THE PATHOPHYSIOLOGICAL ROLE OF DESMOGLEIN-2 IN A STEM CELL MODEL OF ARRHYTHMOGENIC RIGHT VENTRICULAR CARDIOMYOPATHY

by
Robert N. Hawthorne

A dissertation submitted to Johns Hopkins University in conformity with the requirements for the degree of Doctor of Philosophy

Baltimore, Maryland
August 2021

Abstract

Arrhythmogenic right ventricular cardiomyopathy (ARVC) is a progressive heart condition which causes ventricular arrhythmia, fibro-fatty myocardial scarring, and sudden cardiac death. The pathophysiology of ARVC is not well understood, particularly in early phases when arrhythmia can develop prior to structural changes. As a result, treatments for ARVC are limited and poorly targeted. The aim of this work was to generate a patient-derived induced pluripotent stem cell-derived cardiomyocyte (iPSC-CM) model of ARVC harboring a never-before-studied variant in *DSG2* and apply it to glean insight into the roles that *DSG2* and the variant of interest play in important pathophysiological questions surrounding ARVC.

We created a novel iPSC-CM model of ARVC from a patient with a c.2358delA variant in desmoglein-2 (*DSG2*) and found that these *DSG2*-mutant cells displayed substantially altered action potentials and calcium transient dynamics. Mutant cells also displayed aberrant DSG2 expression and atypical organization of contractile proteins. We also sought to generate an isogenic control for the novel ARVC line by using CRISPR-Cas9 to correct the mutant *DSG2* allele. Despite passing all initial quality control checks, deep characterization of the edited cell line led to the discovery of hundreds of unexpected germline mutations, serving as a case study on the importance of thorough validation of new stem cell lines, particularly those that have undergone genome editing. An investigation into the effects of β-adrenergic signaling in our iPSC-CM model revealed that isoproterenol-induced

effects on conduction and action potential upstroke observed in wildtype cardiomyocytes were dampened in *DSG2*-mutants and that *DSG2* suppression in wildtype cells did not recapitulate these effects. Finally, we demonstrated that pro-inflammatory cytokines are much more highly expressed in *DSG2*-mutant iPSC-CMs, and that both canonical and noncanonical NFκB signaling pathways are highly activated in mutant cardiomyocytes compared to controls. We also found high levels of adipo-fibrokine expression in *DSG2*-mutants, which could reveal a link between cardiomyocyte signaling and fibro-fatty changes to the myocardium.

In conclusion, our work suggests that differences in cellular electrophysiology, immune signaling, and response to β-adrenergic stimulation could all play important roles in ARVC pathophysiology. It also contributes new evidence that *in vitro* models of ARVC vary in their behavior significantly and underscores the challenge of defining ARVC *in vitro* in a way that is generalizable across models.

Primary Reader and Advisor: Dr. Leslie Tung

Secondary Reader: Dr. Brian O'Rourke

Thesis Committee: Dr. Leslie Tung, Dr. Brian O'Rourke, Dr. Gordon Tomaselli, and Dr. Marc Halushka

Acknowledgements

I'd first like to express my sincerest gratitude to my thesis advisor, Dr. Leslie Tung for the countless hours invested in me through teaching, poring over data, and writing, editing, and rewriting alongside me – deep into the night on more than one occasion. I thank him for challenging me to push the boundaries of my comfort zones, for offering words of encouragement when I most needed them, and for consistently modeling the attention to detail, rigorous evaluation of data and strong scientific communication skills of the scientist I aspire to be.

I am also deeply grateful to the other members of my thesis committee for the guidance, feedback, and patience that shaped my research and this work. I thank Dr. Brian O'Rourke for our valuable discussions on my work, both during meetings as my project has progressed and in reviewing this dissertation, which expanded my understanding of the molecular mechanisms of cardiac disease and greatly contributed to the quality of this work. I am very grateful to Dr. Gordon Tomaselli for trusting me to carry on a project in which he was heavily invested and especially for his expertise and instrumental feedback on experimental design in stem cell-derived cardiomyocyte models. I'm appreciative of Dr. Marc Halushka for his unwavering personal support throughout this process and for asking questions that forced me to address the weaknesses of my work. While not members of my committee, I am also very thankful to Dr. Stephen Chelko, for his careful guidance on the inflammatory aspects of this project and for helping me plot a course through

this arduous last year, and also to Dr. Kenneth Boheler whose immense technical expertise was invaluable in the advancement of this work.

I would also like to thank all of the members of the Cardiac Bioelectric System Laboratory for making this dissertation possible and for making the lab a fun, engaging place to learn and work. I'm thankful for the senior students in the lab when I arrived, Dr. Renjun Zhu, Dr. David Hunter, Dr. Geran Kostecki, and Dr. Adriana Blazeski, for teaching me innumerable experimental techniques, helping me get this dissertation project off the ground, and for collectively saving me many hundreds of hours of programming. I certainly couldn't have executed this project without an immense amount of help and support from the other members of the lab including Justin Lowenthal, Dr. Justin Morrissette-McAlmon, Makeda Stephenson, Roald Teuben, Marlen Tagle Rodriguez, and Elaine Zhelan Chen. The last four years has been a challenge, and the past year and a half has been especially trying, but I couldn't have asked for a better group of labmates and friends to navigate it with.

I owe a deep well of gratitude to my friends and family who have supported me at every step of this process. Any success I have can be attributed to them. That especially applies to my parents, Robert and Charlotte Hawthorne, who have poured everything they have into my siblings and me, nurturing my interest in science as a kid and making every necessary sacrifice to provide me with the best possible education. I owe you both more than I'll ever be able to repay. To my siblings, Charles, Kayla, and Kendall, thank you for keeping me sane the past few

years and for inspiring me with the strength, curiosity, and kindness with which you move through the world.

Finally, I would like to thank the woman who, over the course of this dissertation work, has gone from my girlfriend to my fiancée to my wife. Thank you, Bernadette, for being there to help me ride the highs and lows of this adventure and to keep me from falling apart when it felt like I might. You're an amazing partner in every sense of the word and I wouldn't be here without you.

Table of Contents

List of Tables

`

List of Figures

Chapter 1 – Introduction

1.1 Overview

Arrhythmogenic right ventricular cardiomyopathy (ARVC) is a primarily inherited cardiac disease estimated to account for more than 10% of cardiovascular deaths in patients younger than 65 years old and approximately 1 in 4 cases of non-traumatic sudden death in young athletes [1–5]. The pathophysiology of ARVC is complex and poorly understood, so current therapies do not address underlying mechanisms of the disease and instead primarily aim to prevent sudden cardiac death by supportive means. Additionally, the disease course and penetrance are highly variable making it difficult to identify common features and broadly useful therapies. Induced pluripotent stem cells (iPSCs) derived from diagnosed patients have emerged as a powerful tool to study ARVC, as these cells can be differentiated

into cardiomyocytes which can then be evaluated *in vitro*. However, the usefulness of iPSC models has not been fully explored, since only a narrow range of ARVC-associated mutations have been studied. The bulk of reports to-date have focused on only one of the several genes with known pathogenic variants. Another issue is that a definition of the ARVC phenotype *in vitro* has not been fully established, making it very difficult to evaluate the effectiveness of an intervention in iPSC models. Expanding and deepening our understanding of these models is critical in the pursuit of insights that can improve patient care.

1.2 Arrhythmogenic Cardiomyopathy: Background and Epidemiology

Arrhythmogenic cardiomyopathy (ACM) is an arrhythmic disease of the myocardium which is not explained by ischemic, valvular or hypertensive heart disease [6]. Arrhythmogenic right ventricular cardiomyopathy (ARVC) is a subcategory of ACM which is characterized by fibro-fatty infiltration and replacement of the myocardium with particular involvement in the right ventricle, which distinguishes it from the most cardiac conditions which disproportionately affect the left ventricle. Clinically, patients with ARVC develop ventricular arrhythmias which often present more frequently as the disease progresses [7].

Estimates for the prevalence of ARVC range from 1:1000 to 1:5000 with significant variation between ethnic and geographic populations [8,9]. While ARVC is primarily inherited in a dominant fashion, most known pathogenic mutations

display incomplete penetrance with only 50-66% of individuals with familial *PKP2* mutations developing a diagnosable form of the disease [10–12]. The penetrance is also highly age-dependent; very few patients present in childhood, but risk of sudden cardiac death increases significantly in early adulthood and onward [13].

Definitive diagnosis of ARVC is traditionally made based on histological findings of transmural fibrofatty infiltration of the right ventricular myocardium via biopsy or necropsy, but clinical diagnosis largely relies on the International Task Force criteria, most recently revised in 2019 [6,14]. These criteria include functional measurements (e.g. right ventricular ejection fraction), incidence of spontaneous arrhythmias, and electrocardiogram (ECG) findings (e.g. T wave inversion, delayed repolarization, etc.). ARVC is associated with very high mortality rates, with an estimated incidence of sudden cardiac death as high as 3% per year in adults [9,15]. Undiagnosed, ARVC is especially deadly, with as many as 50% of all diagnoses made in patients after sudden cardiac death [9,16] largely due to the fact that it is a progressive disease and frequently displays no symptoms until the late stages. Treatment for ARVC is primarily targeted at preventing or limiting deadly arrhythmias using anti-arrhythmic drugs and implantable defibrillators, when indicated. Therapies which target more specific mechanisms of the disease and are capable of slowing or reversing the pathological damage of ARVC are not yet available.

1.3 ARVC Pathology

1.3.1 The desmosome and DSG2

Though, the pathophysiology underlying ARVC is still very poorly understood, there has been general scientific consensus that the common final pathway of the disease involves disruption of the cardiac desmosome, a cellular structure present at the intercalated disc that is critical for intercellular mechanical and electrical coupling between cardiomyocytes [6,17]. The intercellular linkage of the desmosome is primarily formed by the desmosomal cadherins, desmoglein-2 (DSG2) and desmocollin-2 (DSC2), while intracellular linkages to the intermediate filament involve plakophilin-2 (PKP2), plakoglobin (PG), and desmoplakin (DSP) [18]. Mutations in the genes encoding each of these desmosomal proteins have been linked to ARVC, and pathogenic or likely pathogenic mutations in these genes have been identified in more than 60% of ARVC patients [10,13]. These variants have a combined estimated prevalence of approximately 1.2 per 1000 in the general population [19]. *DSG2* is the second most common pathogenic variant found in ARVC patients after *PKP2*, and together they account for 50-80% of the identifiable pathogenic variants found in diagnosed patients [7,20].

One way in which these mutations might contribute to the pathophysiology observed in ARVC is by disrupting the function of the desmosome and thereby compromising the cell-cell cohesion needed for structural stability of the myocardium. This has been supported experimentally; a single missense mutation

in the extracellular cadherin domain of *Dsg2* (responsible for adhesion of the desmosome complex to neighboring cells) was sufficient to recapitulate ARVC features in mice [21]. Another study, though, found that baseline mechanical properties (including cell-cell cohesion) were not substantially altered in NRVMs expressing mutations in plakoglobin and plakophilin, but that the mutations did alter the cells' response to shear stress [22]. Some researchers have suggested that plakoglobin expression is a key hallmark of ARVC, and several studies have investigated the diagnostic usefulness of evaluating plakoglobin expression and localization [23,24]. However, plakoglobin dysregulation has not been found in every ARVC patient, and it has, in fact, produced false positives which turned out to be cases of sarcoidosis instead of ARVC [25].

While patients with advanced ARVC develop severe myocardial scarring and cardiomyocyte loss, which themselves can contribute to arrhythmic risk, substantial evidence demonstrates that cardiac electrical abnormalities – and elevated risk of dangerous arrhythmias – develop well before any overt structural deterioration can be detected [26–28]. This "early concealed phase" suggests that in addition to the structural defects, ARVC-associated mutations affect electrophysiology more directly than is currently recognized; understanding the impact and mechanisms of that effect could greatly improve our ability to diagnose ARVC early and to target therapeutics more carefully. Desmoglein-2 might play a role in this phenomenon as several reports have found that *DSG2* mutations can cause compromised connexin-43 localization and function, reduced sodium current density, and altered

potassium channel expression in isolated mouse cardiomyocytes and iPSC-derived cardiomyocytes [26,29–31].

1.3.2 Inflammation and immune signaling in ARVC

Altered immune signaling and cellular homeostasis have also been proposed as important mechanisms underlying ARVC pathology. Studies have found very strong representation of immune cells and elevated immune cytokines in the myocardium of ARVC patients [25,32–34]. In fact, ARVC is frequently misdiagnosed as other cardiac diseases associated with high levels of inflammation, including myocarditis and sarcoidosis [25,35]. Some researchers have proposed that it is this inflammation that is actually responsible for the cell death and myocardial scarring seen in ARVC. This has been supported by studies showing that in some ARVC patients, periods of very high inflammatory activity lead to acute acceleration of fibrosis and loss of cardiomyocytes [36].

Pilichou et al. discovered that *Dsg2* variants associated with ARVC cause necrosis of cardiomyocytes in mice in a dominant-negative fashion [37] and more recent studies by Chelko et al. support a link between *DSG2* mutation and cell death, though their results emphasize apoptosis over necrosis, mechanistically [38,39]. Inflammatory infiltration by immune cells has been shown to play an important role in pathologic remodeling of the myocardium in ARVC in experimental models. In those *Dsg2*-mutant mice, inhibition of nuclear factor-κB (NFκB) via the small molecule antagonist, Bay11-7082, prevented NFκB-mediated

cytokine storm and inflammatory infiltration of the myocardium, and recent studies have indicated that ARVC iPSC-CMs produce and secrete inflammatory cytokines via innate activation of NFκB, even in the absence of specialized immune cells [39].

1.3.3 Role of exercise and adrenergic stimulation in ARVC

Altered response to exercise and adrenergic signaling has emerged as a very consistent feature of ARVC. Exercise has been shown to drastically exacerbate the progression of ARVC and the risk of sudden cardiac death in both mice [38,40] and human patients [10,41]. While there is strong consensus that ARVC patients should be advised to avoid strenuous exercise, there is still no robust mechanistic understanding of how exercise contributes to the disease progression [6]. One primary physiologic feature of exercise is a sharp stimulation of β-adrenergic signaling, which has itself been shown to affect ARVC patients detrimentally. Isoproterenol and other β-adrenergic agonists cause premature ventricular complexes and induce ventricular arrhythmia in ARVC patients so consistently that isoproterenol testing has been proposed as a diagnostic tool for ARVC [42,43].

We still understand little about why ARVC patients respond so differently to adrenergic signaling but recent studies offer a few clues. At a cellular level, β-adrenergic signaling has been shown to increase desmoglein-2 trafficking to the cellular membrane in wildtype mouse cardiomyocytes [44]. That same work showed that this effect was dependent on plakoglobin expression and phosphorylation at a specific site, which is of note since plakoglobin disruption is a

common feature of ARVC pathology. Studies in *Dsg2*-mutant mice found that exercise triggers extensive cardiomyocyte apoptosis mediated by activation of Ca^{2+}-dependent cysteine protease, CAPN1. That study also found that exercise greatly increased the amount of inflammation and fibrosis in the *Dsg2*-mutant mice, while wildtypes experienced no such effect.

1.4 *In vitro* models of ARVC

Determining the pathogenic mechanisms underlying ARVC has proven difficult, for several reasons. The study of human tissue is challenging, as ARVC is frequently diagnosed in later stages of disease (i.e. after extensive myocardial scarring has developed) when retrieval of a myocardial biopsy would present significant risk of cardiac perforation. Several animal models of ARVC have been established, including in mice [38,39,45,46] and dogs [47,48], which have proven useful in studying specific pathophysiologic processes. However, these models are limited due to substantial differences in cardiac electrophysiology between small animals and humans and the expensive and low-throughput nature of large animal studies [49].

Human induced pluripotent stem cell-derived cardiomyocytes (iPSC-CMs) present a powerful model for studying cardiac disease. Cells from a donor patient can be reprogrammed into induced pluripotent stem cells (iPSCs) and then differentiated into cardiomyocytes using established protocols. These cells then

allow us to study human cardiomyocytes that share a complete genetic background with a patient of known phenotype.

Importantly, iPSC-CM models derived from ARVC patient-specific iPSCs have been shown to recapitulate key characteristics observed in human disease [50,51]. Studies have demonstrated that *PKP2*-mutant iPSC-CMs display reduced membrane localization of plakophilin-2 and plakoglobin, in conjunction with disrupted desmosomal structure [52,53], as has been observed in studies of human tissue. These models have also revealed a number of electrical defects which could potentially explain the predisposition for arrythmia in these patients. *PKP2*-mutant iPSC-CM models display altered calcium homeostasis and connexin-43 function [46] while both *PKP2*- and *DSG2*-mutant iPSC-CM models have demonstrated slower action potential upstrokes and reduced sodium current density [31,54]. Recent studies have indicated that *PKP2*-mutant iPSC-CMs produce and secrete inflammatory cytokines via innate activation of NFκB [39], which supports the findings of mouse studies, and is consistent with altered immune signaling observed in the hearts of human ARVC patients [25,35,38,39].

iPSC models offer several other advantages in studying ARVC. With the most advanced differentiation protocols, iPSCs can yield highly pure populations of cardiomyocytes, which allow researchers to study their behavior without the confounding effects of resident non-cardiomyocytes, such as fibroblasts and immune cells. They also allow for genomic manipulation which enables the association of phenotypic shifts with specific genetic changes. In addition to these

advantages, iPSC-CMs can be efficiently expanded to produce a large number of cells. This feature offers a high-throughput alternative to animal models and allows for larger screening experiments and, potentially, more efficient drug development. These cells also offer amazing potential contributions to personalized medicine, as an individual patient's disease could be modeled, and potential therapies could be screened *in vitro*.

The primary drawback of iPSC-CMs is the fact that current differentiation protocols produce cardiomyocytes at an approximately late-embryonic or neonatal state of maturation, with less developed metabolism, organization and electrophysiology than in adult cells [55,56]. Our ability to further mature these cells using electromechanical stimulation and metabolic training is improving rapidly, but we can already extract great value from these models by comparing cell lines at similar levels of maturity and by focusing on aspects of disease that are less affected by immaturity or for which differences might even be accentuated early in maturity such as cell-cell connectivity and intrinsic beating rate. Another major hurdle in developing and improving these models is the fact that there is no accepted definition of ARVC "disease" behavior *in vitro*. Having a set of phenotypic characteristics that reflect an ARVC disease state across distinct cell lines with varying pathogenic variants would enhance the utility of these models in testing the efficacy of interventions.

We hope that by generating and studying iPSC-CMs harboring unique pathogenic variants associated with ARVC, we can begin to uncover the

mechanisms by which these variants contribute to myocardial pathologic changes and to arrhythmia in the early concealed phase of ARVC, possibly revealing new potential targets for therapeutic intervention.

1.5 Dissertation Overview

The overall aim of this work is to generate a patient-derived iPSC-CM model of ARVC harboring a never-before-studied variant in *DSG2*, thoroughly characterize that model, and apply it to gain insight into the roles that *DSG2* and the variant of interest play in important pathophysiological questions surrounding ARVC. Chapter 2 contains the bulk of this work, detailing the ARVC patient donor's clinical history, the generation and validation of the *DSG2*-mutant iPSC line, and our evaluation of the baseline electrophysiological and biomolecular phenotypes of the novel line. In that chapter, we also compare the effects of the c.2358delA variant against global *DSG2* mRNA suppression. Chapter 3 describes our effort to create an isogenic control for the *DSG2*-mutant line, details our careful validation and discovery that we had not fully accomplished that goal, and attempts to lay out lessons that can be learned from that process. In Chapter 4, we explore the ways in which β-adrenergic stimulation exerts different effects on the behavior of control vs. ARVC iPSC-CMs. Finally, Chapter 5 focuses on our work to characterize the inflammatory landscape of the *DSG2*-mutant iPSC-CMs and to identify pathways by which signaling from cardiomyocytes might contribute to ARVC pathophysiology.

Substantial portions of the data reported in Chapters 2 and 5 have been published in The Journal of Clinical Medicine [57].

Chapter 2 – Physiological impact of familial *DSG2* variant in patient-specific iPSC-CMs

2.1 Background

Advancements in technology surrounding induced pluripotent stem cells and cardiomyocyte differentiation, offer a powerful opportunity to study ARVC *in vitro* with patient-derived iPSC-CMs. The purpose of the work detailed in this chapter was to identify the effects of a known familial pathogenic mutation in desmoglein-2 – *DSG2* c.2358delA – on the physiology of iPSC-derived cardiomyocytes. For these experiments we focused on a novel iPSC line derived from a clinically diagnosed ARVC patient with a familial mutation in *DSG2* in comparison to two wildtype control lines. Our goals were to: 1) compare the electrophysiological properties of

control and *DSG2*-mutant cardiomyocytes, 2) evaluate the expression and localization of desmoglein-2 and other key proteins involved in cell-cell connections and electrophysiology in *DSG2*-mutant iPSC-CMs, and 3) compare the physiological effects of *DSG2* c.2358delA mutation with global *DSG2* mRNA suppression. We hypothesized that the *DSG2*-mutant iPSC-CMs will display slower conduction velocities and reduced excitability as well as impaired desmosomal formation and accompanying impairment of intercalated disc organization.

We believe that a deeper understanding of the role desmoglein-2 plays in human cardiomyocytes will provide important insight into ARVC pathophysiology and that finding commonalities with better-studied *PKP2*-mutant cell lines would advance our goal of creating a phenotypic definition of ARVC *in vitro*.

2.1.1 Family history and clinical phenotype of ARVC patient donor

For these studies, we selected a patient with diagnosed ARVC, who harbors a familial genetic variant in *DSG2*.[*] The patient (JHU013) is a 48-year-old woman of South Asian heritage. She was diagnosed with ARVC at age 45 after a diagnosis in her sister (the proband for this family) prompted a thorough cardiac evaluation. Despite the relatively recent diagnosis, patient JHU013 had abnormal cardiac function for many years prior. Her 12-lead ECG was positive for T wave inversions, which were initially observed at age 22, although they have been consistently

[*] Thank you to Dr. Cynthia A. James for their work coordinating with the ARVC registry and maintaining the patient clinical data for this project.

negative for epsilon waves. She also began experiencing paroxysmal dizziness and palpitations at age 32. In her most recent exam, her ECG showed T wave inversions in anterior precordial leads V1-V4 with inferior repolarization abnormalities in leads II, III, and aVF (Fig. 2.1, Table 2.1). Cardiac magnetic resonance (CMR) imaging demonstrated mild dilation of the right ventricle and dyskinesia of the right ventricular free wall (118 mL/m^2 RV EDVi; Table 2.1) with microaneurysm formation along the right ventricular outflow tract (Fig. 2.2B). CMR was also notable for extensive delayed gadolinium enhancement involving the right ventricular free and inferior walls, suggesting significant fibrosis in those regions. However, no ventricular wall fat infiltration was observed. Notably, as of her last follow-up, patient JHU013 had no documented history of sustained ventricular arrhythmia.

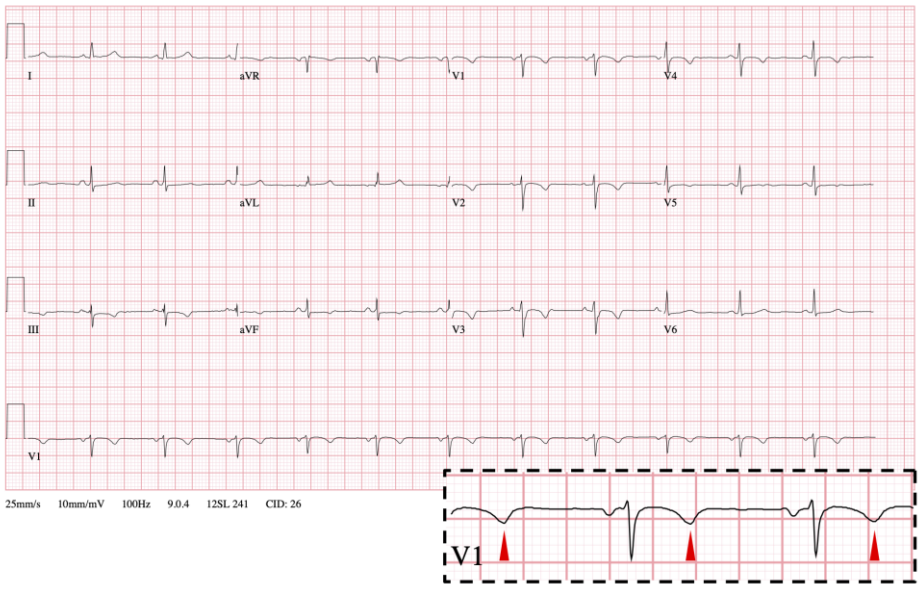

Figure 2.1 Electrocardiogram for ARVC patient donor. 12-lead ECG of patient JHU013 showing T wave inversion in leads V1-V4 (red markers), a classic feature in ARVC patients. Dashed box inset highlights T wave inversion in lead V1.

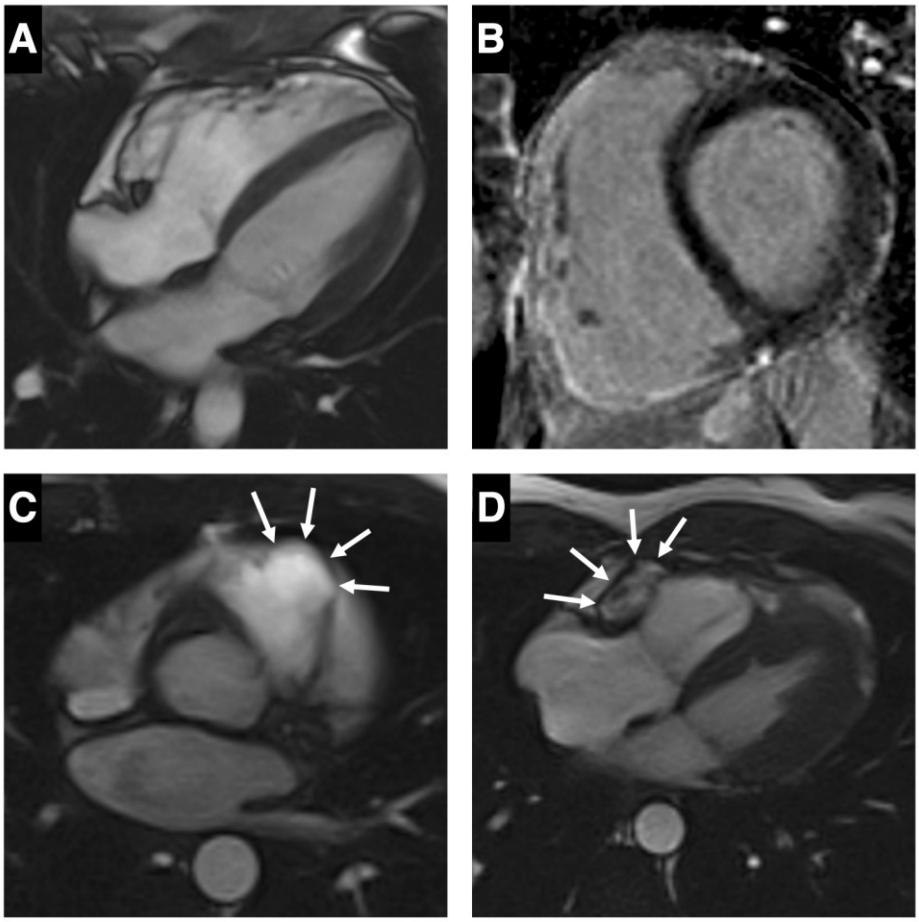

Figure 2.2 Cardiac MRI for ARVC patient donor. Images obtained at last clinical follow-up. (A) Four-chamber, bright blood, steady-state free precession cardiac MRI (CMR) image showing mild RV enlargement. (B) Extensive RV enhancement of the anterior and inferior walls on short axis post-contrast late enhancement CMR. (C-D) End-systolic axial images obtained from cine CMR showing regions of RV outpouching secondary to dyskinesia (arrows).[*]

[*] Thank you to Dr. Stefan Zimmerman for their help acquiring and interpreting this CMR data.

Demographic	
Gender	Female
Race / Ethnicity	South Asian
Presentation (age [yrs.]: symptoms)	22: anterior precordial T wave inversions noted on ECG. 43: dizziness, palpations
Age at ARVC diagnosis (yrs.)	45
Age at last follow-up (yrs.)	51
2010 Task Force Criteria Fulfillment [14]	
ECG Repolarization Abnm.	Major: Inverted T waves in right precordial leads (V_1, V_2, V_3, and V_4)
ECG Depolarization Abnm.	None
Arrhythmia	Minor: ≥ 500 PVCs per 24 hours on Holter monitor
Structural	Major: Regional RV dyskinesia + RV EDVi > 100 ml/m^2
Family History	Major: ARVC confirmed in a first-degree relative who meets current Task Force criteria
Cardiac MRI (at last follow-up)	
RV EDVi (ml/m^2)	118
RV EDVi / LV EDVi	2.62
RV wall-motion Abnm.	Regional dyskinesia, aneurysms
LV wall-motion Abnm.	None
RVEF (%)	44
LVEF (%)	57
Delayed enhancement	Extensive delayed enhancement in RV free wall and inferior wall
Events	
Sustained ventricular arrythmia	No
Cardiac transplant	No
Death	No

Table 2.1 Demographic data and clinical history of patient JHU013. Abnm.: abnormalities, PVC: premature ventricular complex, RV: right ventricle, LV: left ventricle, RVEF: right ventricular ejection fraction, LVEF: left ventricular ejection fraction, EDVi: end diastolic volume indexed to body surface area.

Familial genetic screening revealed that several members of the donor family harbored a heterozygous single nucleotide deletion mutation in *DSG2*. This variant – *DSG2* c.2358delA – was identified in the donor patient, her sister (the proband), her two children, her mother, and her niece and nephew (Fig. 2.3). As of last follow-up no one in the family besides patient JHU013 and her sister had been definitively diagnosed with ARVC. Their children (ages 13-20 at last follow-up) were below the age at which we would expect to see phenotypic expression due to the incomplete age-related penetrance of ARVC. However, the younger family members have experienced some notable cardiac abnormalities. The proband's son (age 20) experienced 420 premature ventricular complexes (PVCs) over a 24-hour period, which was high but did not quite reach the 2010 Task Force criteria of >500 over 24 hours. The proband's daughter (age 17) has a history of palpitations, while the donor's daughter (age 16) has a history of palpitations as well as T wave inversions in V1 and V3 on ECG.

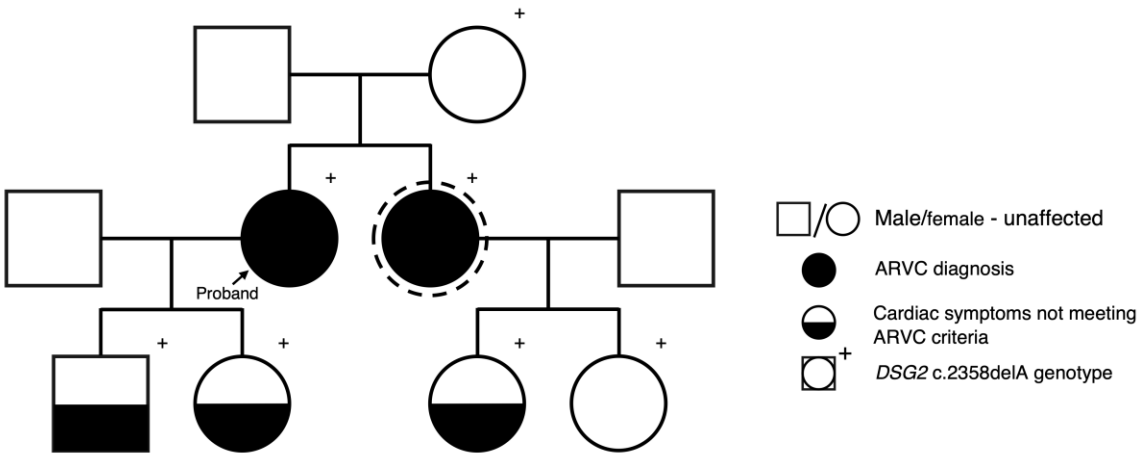

Figure 2.3 Family pedigree for iPSC donor. Family pedigree of patient JHU013 (dashed circle) harboring a pathogenic variant in desmoglein-2 (*DSG2* c.2358delA). Arrow signifies proband.

2.1.2 The DSG2 c.2358delA variant

Sequence analysis shows that the *DSG2* c.2358delA variant harbored by patient JHU013 – identified in ClinVar as NM_001943.5(DSG2):c.2358del (p.Asp787fs) – causes a frameshift mutation resulting in the formation of a premature stop codon 21 codons downstream. This frameshift produces a truncation in the intracellular cadherin-like domain (ICD) of the desmoglein-2 protein (Fig. 2.4). This variant was evaluated in line with standards of the American College of Medical Genetics and Genomics and the Association for Molecular Pathology [58,59] and classified as "likely pathogenic". That classification was based on the satisfaction of these criteria:

1) PVS1: Null variant (nonsense, frameshift, canonical $+/-1$ or 2 splice sites, initiation codon, single or multi-exon deletion) in a gene where loss of function (LOF) is a known mechanism of disease.
2) PM2: Absent from controls (or at extremely low frequency if recessive) in Exome Sequencing Project, 1000 Genomes or ExAC.
3) PP3: Deleterious effect on the gene or gene product (conservation, evolutionary, splicing impact, etc.) supported by multiple lines of computational evidence.

Cascade screening and clinical criteria are consistent with the *DSG2* loss of function contributing to the pathogenesis of both the proband and JHU013.

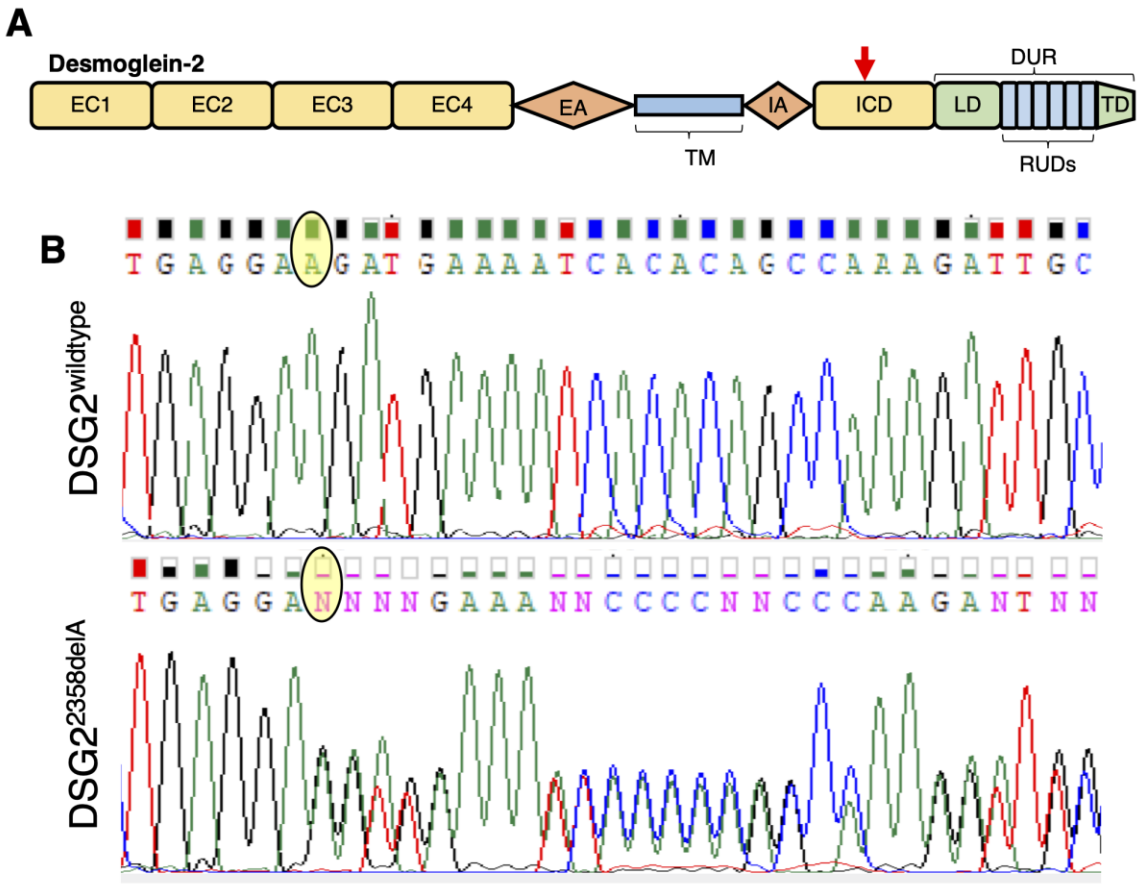

Figure 2.4 The *DSG2* c.2358delA variant. A) Schematic protein structure of desmoglein-2. EC1-4: extracellular cadherin domains, EA: extracellular anchor domain, TM: transmembrane domain, IA: intracellular anchor domain, ICD: intracellular cadherin-like domain, LD: linker domain, RUD: repeat unit domain with six repeats, TD: terminal domain, DUR: DSG unique region; Red arrow indicates location of truncation caused by the *DSG2* c.2358delA variant. (B) Sanger sequencing of *DSG2* in control and JHU013 iPSCs showing the c.2358delA mutation. Yellow oval highlights c.2358 nucleotide under investigation. 'N' indicates heterozygosity at that location.

2.2 Methods

2.2.1 iPSC line generation

Whole blood samples were collected from patient JHU013 by members of the Johns Hopkins ARVC Registry team. Peripheral blood mononuclear cells (PBMCs)

were isolated using Ficoll-Paque PLUS density gradient media (GE Healthcare, Waukesha, WI, USA) and plated at high density in PBMC growth media (PBMC-M; see Table 2.2 for formulation). PBMCs were expanded for 10 days before being harvested and reprogrammed using the Cytotune 2.0 Sendai virus kit containing Yamanaka factors (Thermo Fisher Scientific, Waltham, MA, USA), per manufacturer's protocol.

PBMC Growth media (PBMC-M) formulation
IMDM/F12 (Life Technologies, Frederick, MD, USA)
2 mg/mL recombinant human albumin (Sciencell, Carlsbad, CA, USA)
1% v/v chemically defined lipid concentrate (Life Technologies)
10 µg/mL recombinant human insulin (Corning)
100 µg/mL recombinant human transferrin (Corning)
15 ng/mL sodium selenite (Corning)
64 µg/mL L-ascorbic acid 2-phosphate (Sigma-Aldrich)
450 µM 1- thioglycerol (Sigma-Aldrich)
100 ng/mL SCF (PeproTech, Cranbury, NJ, USA)
10 ng/mL IL-3 (PeproTech)
2 U/mL EPO (R&D Systems, Minneapolis, MN, USA),
40 ng/mL IGF1 (PeproTech)
1 µM dexamethasone (Sigma-Aldrich)

Table 2.2 PBMC growth media formulation.

After 24 hours, the cells were resuspended in PBMC-M media, seeded into Synthemax-treated tissue plates (Corning, Corning NY, USA), and cultured for six days with media changes every other day. On day 7 after viral reprogramming, the media was replaced with a 1:1 mixture of PBMC-M and Essential 8 media (E8; Thermo Fisher). The cells were harvested with TrypLE Select Enzyme (Thermo Fisher) and plated in E8 supplemented with 10 μM Y-27632 dihydrochloride

(Tocris Bioscience, Bristol, United Kingdom) on plates coated with Geltrex matrix (Thermo Fisher). Colonies were then picked by pipette under a microscope, re-plated into separate wells of a tissue culture plate and expanded until passage 10. DNA was then isolated to verify the loss of the Sendai virus and, clones were screened via Sanger sequencing and karyotyping.

2.2.2 iPSC-CM differentiation and culture

iPSCs were plated into 6-well tissue culture-treated polystyrene plates coated with Geltrex diluted 1:200 in DMEM/F-12, HEPES (Thermo Fisher). For the first 18-22 hours, iPSCs were maintained in E8 with 10 μM Y-27632 dihydrochloride. Monolayers of iPSCs were rinsed with DMEM/F-12 and fed with fresh E8 daily. On the fourth day after plating, when cells had reached about 70-90% confluency, the media was replaced with RPMI 1640 medium supplemented with B-27 supplement minus insulin ("B27-minus", Thermo Fisher) plus 6 μM CHIR-99021 (Selleck Chemicals, Houston, TX, USA) to initiate differentiation; this marks day 0 of differentiation. Thereafter, media was changed as follows: B27-minus on day 2, B27-minus with 5 μM IWR-1 (Sigma-Aldrich Corp) on day 3, B27-minus on day 5 and d7ay , and RPMI 1640 medium with B-27 supplement with insulin ("B27+"; Thermo Fisher) on day 9 and every other day afterwards. Spontaneous beating was observed in monolayers starting at day 7 to day 9.

Between day 11 and day 13, wells of differentiated iPSC-CMs were washed with 0.5 mM EDTA (Thermo Fisher) in calcium-free phosphate buffered solution ("PBS";

Thermo Fisher) and incubated in EDTA solution for 5-10 minutes at 37 °C. Afterwards, the EDTA was aspirated off and 0.05% Trypsin-EDTA (Corning) was added for 3-5 minutes at 37 ºC. Cells were triturated before defined trypsin inhibitor ("DTI"; Life Technologies) was added to stop digestion. The resultant suspension was centrifuged at 200 G for 5 minutes. After aspirating off the supernatant, the cell pellet was resuspended in B27+ into a homogenous suspension of cells and distributed over 6-well plates or T-75 flasks freshly coated with 1:200 Geltrex at a surface area ratio of approximately 1:1.5.

On day 14 and day 16, media was replaced with "lactate medium consisting of glucose-free DMEM media supplemented with 4 mM L-lactate, 1x non-essential amino acids (Thermo Fisher), and 1x GlutaMAX (Thermo Fisher) to select for and purify cardiomyocytes in culture. After four cumulative days in lactate medium, iPSC-CMs were switched back to B27+ media, and media was replaced every 2-3 days thereafter.

On day 28, cells were passaged as above, using Trypsin-EDTA and DTI, centrifuged and resuspended in fresh B-27+ media with 10 μM Y-27632 dihydrochloride. Cells in suspension were counted using a Countess automatic cell counter (Invitrogen) and plated at 250,000 cells per cm^2 of surface area into tissue culture plates coated with 1:200 Geltrex. For imaging and optical mapping experiments, Thermanox plastic coverslips (Thermo Fisher) were placed into 24 or 48-well plates before Geltrex coating to allow easy removal of the monolayers at the time of analysis.

2.2.3 Biomolecular assays

For immunostaining, samples were fixed in 4% paraformaldehyde (Thermo Fisher), permeabilized in 0.5% Triton-X for 5 minutes and probed using standard immunocytochemistry techniques. iPSCs were stained for OCT3/4, SOX2, and Nanog, and iPSC-CM monolayers were stained for desmoglein-2, plakoglobin, plakophilin-2, cardiac troponin I, α-actinin and nuclei (see Table 2.3 for primary antibody details). Images were acquired via confocal microscopy. For images being compared, confocal laser and gain settings were held constant across all groups. To assess Z-line length in iPSC-CMs, 400 μm^2 regions of interest were selected from high magnification images at random by computer script, and α-actinin-immunopositive lines were measured by a blinded observer using image analysis software.

For RT-qPCR experiments, total RNA was extracted from iPSC-CMs on differentiation day 37-39 using a column preparation (RNeasy Mini Kit; Qiagen Sciences, Germantown, MD, USA), and reverse transcription was performed using the High-Capacity cDNA Reverse Transcription Kit (Applied Biosystems). cDNA was amplified using PowerUp SYBR Green PCR master mix (Applied Biosystems) and a QuantStudio 7 Flex RT-PCR system (Applied Biosystems) under manufacturer's recommended protocol. All assays were performed with three technical replicates and a minimum of three pooled cell samples. *GAPDH* and 18S rRNA were used in combination as internal controls; all primer sequences are listed in Table 2.4.

For Western blots, total protein was extracted from iPSC-CMs using RIPA lysis buffer. Samples were prepared and run under denaturing conditions on NuPAGE 4-12% Bis-Tris gels (Thermo Fisher) in MOPS buffer using manufacturers recommended reagents and protocol. Proteins were transferred to PVDF membranes using the Trans-Blot Turbo system (Bio-Rad Laboratories, Hercules, CA, USA), probed with primary antibodies (Table 2.3) and visualized with fluorescent secondary antibodies (LI-COR, Lincoln, NE, USA). Images were obtained and analyzed using a LI-COR Odyssey CLx imaging system.

Target	Manufacturer	Product #	Application
α-actinin (ACTN2)	Abcam	ab137346	ICC, WB
Phospho-CaMKII (The286)	Cell Signaling	12716	WB
Cardiac Troponin-I (cTnI)	United States Biological	T8665-13F	ICC
Desmoglein-2 (DSG2)	Proteintech	21880-1-AP	ICC, WB
Desmoglein-2 – extracellular	Invitrogen	326100	ICC
Desmoglein-2 – C-terminus	Abcam	ab150372	ICC
GAPDH	Abcam	ab9483	WB
Nanog	BioLegend	674001	ICC
OCT3/4	Santa Cruz Bio.	SC-5279	ICC
Phospho-PKA C (Thr197)	Cell Signaling	5661	WB
Plakoglobin	Abcam	ab184919	WB
Plakoglobin (JUP)	MiliporeSigma	P8087	ICC
Plakophilin-2 (PKP2)	Abcam	ab220840	ICC, WB
SOX2	Thermo Fisher Scientific	14-9811-80	ICC

Table 2.3 Primary antibodies for immunocytochemistry and Western blot. ICC: Immunocytochemistry; WB: Western blot.

Gene	Forward (5'→3')	Reverse (5'→3')
GAPDH	GCACCGTCAAGGCTGAGAAC	TGGTGAAGACGCCAGTGGA
18S rRNA	CGGCTACCACATCCAAGGAA	GCTGGAATTACCGCGGCT
ATP2A	ATGGGGCTCCAACGAGTTAC	TTTCCTGCCATACACCCACAA
CACNA1C	GAAGCGGCAGCAATATGGGA	TTGGTGGCGTTGGAATCATCT
CAMK2A	ATTGAAGCCATAAGCAATGGAGA	TTCCGGGACCACAGGTTTTC
CASQ2	GGCAGAAGAGGGGCTTAATTT	GAAGACACCGGCTCATGGTAG
DSG2	ACGTAGAAGTTACGCGCATAAA	GGGTCACAATTCCTTCGTTAGTT
GJA1	ACAGGTCTGAGTGCCTGAAC	CGAAAGGCAGACTGCTCATC
JCTN	CATGGAGGACACAAGAATGGG	CCAAACGACAGCTACAGATGT
JUP	TCTCCAACCTGACATGCAACA	CATAGTTGAGACGCACAGAGTTC
KCNH2	TTCGACCTGCTCATCTTCGG	CGATGCGTGAGTCCATGTGT
KCNJ2	GTGCGAACCAACCGCTACA	CCAGCGAATGTCCACACAC
KCNQ1	GCGTCTCCATCTACAGCACG	GAAGTGGTAAACGAAGCATTTCC
PKP2	ATGACATGCTAAAGGCTGGCA	GGGAGCTGTACTGTGCTGTTC
PLN	ACCTCACTCGCTCAGCTATAA	CATCACGATGATACAGATCAGCA
RYR2	ACAACAGAAGCTATGCTTGGC	GAGGAGTGTTCGATGACCACC
SCN5A	GTGCCCAGAAGCAGGATGAG	GGACATACAAGGCGTTGGTG
SLC8A1	ACAACATGCGGCGATTAAGTC	GCTCTAGCAATTTTGTCCCCA
SLN	ATGGTCCTGGGATTGACTGAG	GTGCCCTCGGATGGAGAATG
TRDN	TCACAGAAGACATAGTGACGACG	TGGCAATAGAGCTTGCTGAAA

Table 2.4 RT-qPCR primer sequences.

2.2.4 RNA-sequencing

iPSC-CMs cultured to differentiation day 35 were gently dislodged with a cell scraper, suspended in TRIzol reagent and flash frozen for storage. RNA was then extracted and processed by an outside vendor (GENEWIZ, South Plainfield, NJ, USA). RNA across the samples had a mean RIN of 9.2. RNA-seq libraries were

prepared using a standard poly-A selection protocol for isolating mRNAs. Final libraries were sequenced as 2x150bp paired-end sequencing on an Illumina HiSeq. Samples were sequenced to a depth of ~30-40 million paired reads/cell. Libraries were mapped to the human genome (GRCh38) using STAR (2.3.1a) [60] with two-pass mode, and then counted using featureCounts (2.0.0) through the Subread package [61,62].* Identification of differentially expressed genes was done using DESeq2 [63], with genes identified as differentially expressed by Benjamini-Hochberg-adjusted p-value < 0.05. KEGG pathway maps were made using the Pathview package (1.26.0) [64]. All raw RNA-sequencing data as well as count tables and sample information are available on GEO at accession number: GSE176209.

2.2.5 Electrophysiological studies

All staining and mapping steps were performed in Tyrode's solution (see Table 2.5 for formulation) containing 10 μM blebbistatin (PeproTech) to suppress contraction and prevent motion artifact. For voltage mapping, coverslips with iPSC-CM monolayers were stained with either 10 μm di-4-ANNEPS (all non-siRNA-treated samples) or 10 μm di-8-ANEPPS (all siRNA-treated samples) for 10 minutes. For calcium mapping, coverslips were stained with calcium indicator Rhod-2 AM (1 μM; Thermo Fisher), for 15 minutes. To aid cell loading, all staining solutions were

* Thank you to Suraj Kannan for performing the processing and initial analysis of RNA-sequencing data.

supplemented with 0.05% Pluronic F-127. After incubation in the staining solution, coverslips were gently washed and transferred to a 35 mm petri dish with fresh mapping solution. The dish was placed on a stage heated to 37 ºC for the remainder of the experiment. iPSC-CM monolayers were stimulated from one edge with a bipolar palladium line electrode delivering 10 V, 10 ms monophasic anodal rectangular pulses at predetermined cycle lengths including: 2000, 1000, 700, 500, and 333 ms. Optical mapping recordings were taken using a 100x100 pixel CMOS camera (MiCAM Ultima-L; SciMedia, Costa Mesa, CA, USA) and analyzed using custom MATLAB scripts.

Intensity recordings at each pixel were de-noised using a Bayesian L_1-regularized global filter and convolved with a 5x5 spatial Gaussian filter. Activation times were defined as the moment where maximum of the derivative of membrane potential (dV/dt) occurs. Histograms of local conduction velocities for each sample were fitted to a Gaussian curve, and the mean of the curve was defined as the average conduction velocity (CV). Action potential durations – measured as the time from the moment of maximal upstroke velocity to the moment of 80% or 30% recovery from peak to resting membrane potential (APD_{80}, APD_{30}) – were determined for all local traces over the recording region for each monolayer and fit with Gaussian curves to determine the mean value for each sample, as described for CV measurements. Peak relative upstroke velocity was calculated by normalizing the action potential trace at each pixel such that it varied between 0 and 1, calculating the differential along the curve and selecting the point in the

upstroke where d/dt was maximized. For calcium mapping data, time-to-peak was measured by identifying the time point at which the calcium transient begins to rise and the point at which it reaches its highest signal value and taking the difference. The calcium decay rate (λ, i.e. τ^{-1}) was measured by fitting the portion of the calcium transient between 30% and full decay to an exponential curve and extracting the exponential constant. Spatial heterogeneity of all parameters was measured using Gaussian fits; for each parameter and each sample, the standard deviation of all measurements within the recording region was divided by the mean, providing the relative standard deviation (RSD) of that parameter.

Tyrode's Media Formulation
5 mM HEPES
1 mM magnesium chloride hexahydrate
5.4 mM potassium chloride
135 mM sodium chloride
0.33 mM sodium phosphate
1.8 mM calcium chloride
5.0 mM glucose

Table 2.5 Tyrode's media formulation. Combine all solutes in Milli-q filtered water and warm to 37 ºC. Once at temperature, add hydrochloric acid dropwise, to adjust pH to 37. Expected osmolarity is ~293 mmol/kg.

2.2.6 siRNA-mediated DSG2 knockdown

Pre-designed siRNA oligos targeted against *DSG2* as well as a universal negative control siRNA were purchased (MilliporeSigma, St. Louis, MO, USA). A cocktail of three distinct anti-*DSG2* oligos (see Table 2.6 for oligo sequences) was complexed for transfection using TransIT-siQUEST transfection reagent (Mirus Bio, Madison,

WI, USA) and Opti-MEM reduced serum medium (Thermo Fisher). On differentiation day 35, iPSC-CM monolayers were fed with B27+ media supplemented with siRNA complexes for a final concentration of 50 nM. The monolayers were incubated with the siRNA complexes and transfection reagent for 48 hours, the media was then replaced with fresh B27+ media, and the samples were analyzed the following day (72 hours total treatment time). For preliminary experiments, siRNA was covalently labelled with Cy5 fluorophores using the Label IT siRNA Tracker kit (Mirus Bio) to allow for visual evaluation of transfection efficiency.

Mat. # - Line	Forward (5'→3')	Reverse (5'→3')
VC30002-001	GAAAUUGAGCAGAGACAAA	UUUGUCUCUGCUCAAUUUC
VC30002-004	CUUCUACCUUGGUAGAUCA	UGAUCUACCAAGGUAGAAG
VC30002-007	CUACUCUGGCCAUGCCUAA	UUAGGCAUGGCCAGAGUAG

Table 2.6 siRNA oligo sequences. Purchased from MilliporeSigma.

2.2.7 Statistics

RT-qPCR data is presented as mean ± standard deviation of the mean. Unless otherwise indicated, all other summary data is presented as mean ± 95% confidence interval, calculated in R. Continuous variables were compared using unpaired, unequal variance Student's t-test with a Holm-Bonferroni family-wise error correction. For RT-qPCR data, normalized relative quantities and their standard errors were calculated using the EasyqpcR software package [65]. $P<0.05$ in two-tailed analysis was considered significant. *: $p<0.05$, **: $p<0.01$, ***: $p<0.001$.

2.3 Results

2.3.1 Establishment of a patient-specific iPSC-CM model with novel pathogenic variant DSG2 c.2358delA

In order to determine the functional and pathological consequences of *DSG2* c.2358delA, we generated an iPSC line from the affected patient.[*] Briefly, peripheral blood mononuclear cells were isolated from the donor's blood, induced to form blast cells and reprogrammed into pluripotency via transfection with Sendai virus vectors containing the Yamanaka factors. These cells were re-plated at low density and clonal colonies were selected and expanded. Basic characterization of these clones was then performed.

Chromosomal analysis of this new *DSG2*-mutant iPSC line (referred to as "JHU013" henceforth) demonstrated a normal karyotype, and Sanger sequencing showed a heterozygous *DSG2* c.2358delA variant present in the reprogrammed cells, as was expected based on the donor's genotype (Fig. 2.5). We then measured canonical markers of pluripotency via immunostaining and RT-qPCR in JHU013 iPSCs. Immunofluorescent images showed strong nuclear expression of SOX2, Nanog and OCT3/4, while RT-qPCR experiments demonstrated very high expression of *OCT3/4*, *SOX2*, *NANOG,* and *LIN28* compared to human primary cardiac fibroblasts, which are terminally differentiated.

[*] iPSC reprogramming was largely performed by Deborah Disilvestre and other members of the Tomaselli laboratory.

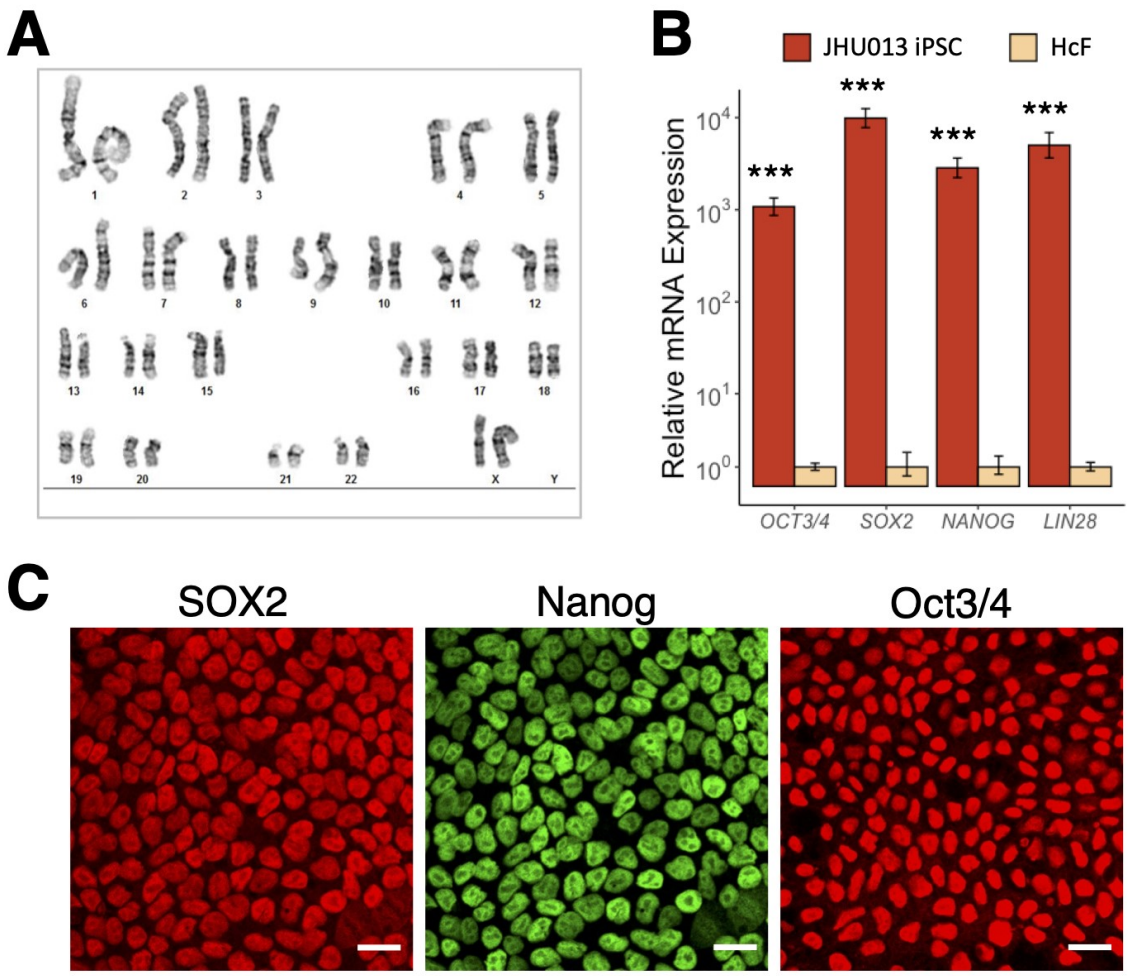

Figure 2.5 Normal karyotype and expression of pluripotency markers in JHU013. (A) Chromosomal analysis of JHU013 iPSCs. (B) RT-qPCR analysis showed abundant expression of pluripotency-associated transcripts in JHU013 iPSCs relative to terminally differentiated control cells (primary neonatal human cardiac fibroblasts, HcF). ***$p < 0.001$ via unpaired t-test. (C) Confocal images of JHU013 iPSCs depicting immunopositivity for canonical markers of pluripotency: SRY (sex determining region Y)-box 2 (SOX2), homeobox NANOG, and Octamer binding transcription factor-3/4 (OCT3/4).

To establish control lines for our experiments, we used an iPSC line derived under an identical protocol from a healthy, Caucasian volunteer who, like patient JHU013, was a female in her early 50s at the time of donation (JHU001). We also selected a widely available wildtype control line derived from a healthy East Asian

male donor in his early 30s (WTC11, “WTC”). iPSCs from all three lines were subjected to a Wnt-mediated cardiogenic differentiation protocol and began to beat on approximately day 8. On days 10-14 the cardiomyocyte (CM) population was enriched metabolically via lactate purification as previously described [66]. Cardiomyocytes formed a syncytial monolayer after being plated onto coverslips on day 28 and were cultured until day 35-39, when they were analyzed. Differentiated iPSC-CMs were measured by flow cytometry to be >90% positive for cardiac troponin T (cTnT) on day 35, indicating high purity of cardiomyocytes, with no differences in differentiation efficiency noted between control and JHU013 iPSC lines (Fig. 2.6A). The mean spontaneous beating rates for the iPSC-CM monolayers were similar among all lines on differentiation day 38 (67.6±5.7 beats per minute {BPM} in JHU013 vs. 68.4 ±12.1 and 64.8±5.8 BPM in JHU001 and WTC, respectively) (Fig. 2.6B).

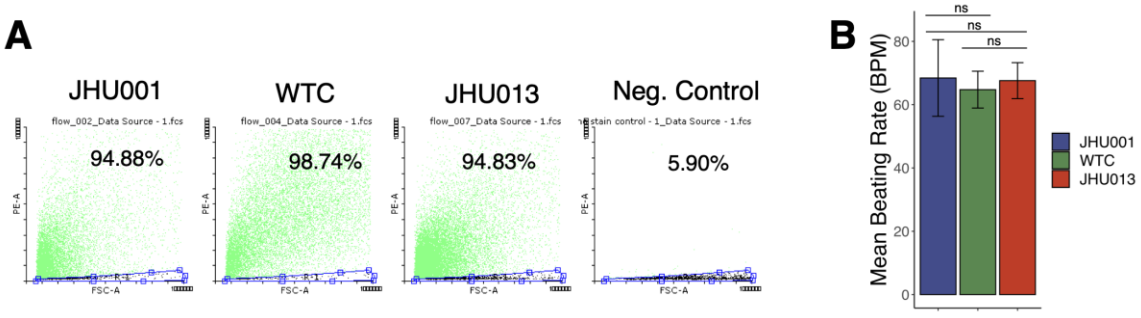

Figure 2.6 Baseline characterization of iPSC-CM model. (A) Cardiac Troponin T expression in iPSC-CMs. iPSC-CMs were fixed on differentiation day 35, stained, and analyzed via flow cytometry. CMs from all three lines demonstrated >90% cTnT-positivity indicating high cardiomyocyte purity. (B) Mean spontaneous beating rate of iPSC-CM monolayer on differentiation day 38. Measured from phase contrast video taken using a Lumascope incubator microscope. Beating rate was not significantly different between the lines. For (B) JHU001 (n=12), WTC (n=12) JHU013 (n=14).

2.3.2 Electrophysiological characterization of JHU013 iPSC-CMs

On day 28 of differentiation, iPSC-CMs from each line were plated onto coverslips and cultured for another 9-11 days to allow confluent monolayers to develop. At day 37-39, optical mapping recordings were taken using a CMOS camera to measure the electrophysiological characteristics of the monolayers. For these experiments, membrane potential was measured using voltage sensitive dye Di-4-ANEPPS, while calcium transients were measured using Rhod-2 AM. For all experiments, pacing stimulation was applied using a bipolar palladium line electrode at cycle lengths ranging from 250 ms to 2000 ms. For most experiments, data for the 500 to 1000 ms range is presented, as these are the rates at which we most consistently achieved capture.

One of the most striking findings from these experiments was that the action potentials of the JHU013 monolayers was substantially shortened compared to both wildtype controls. Action potential duration at 80% repolarization (APD_{80}) was significantly reduced in JHU013 CMs compared with both control lines (220±24 ms in JHU013 vs 311±27 ms in JHU001 and 365±26 ms in WTC at 1000 ms pacing) as was APD_{30} (134±15 ms in JHU013 vs 213±21 ms in JHU001 and 227±25 ms in WTC at 1000 ms pacing; Fig. 2.7). This result indicates considerable differences in repolarization behavior in the *DSG2*-mutant iPSC-CMs.

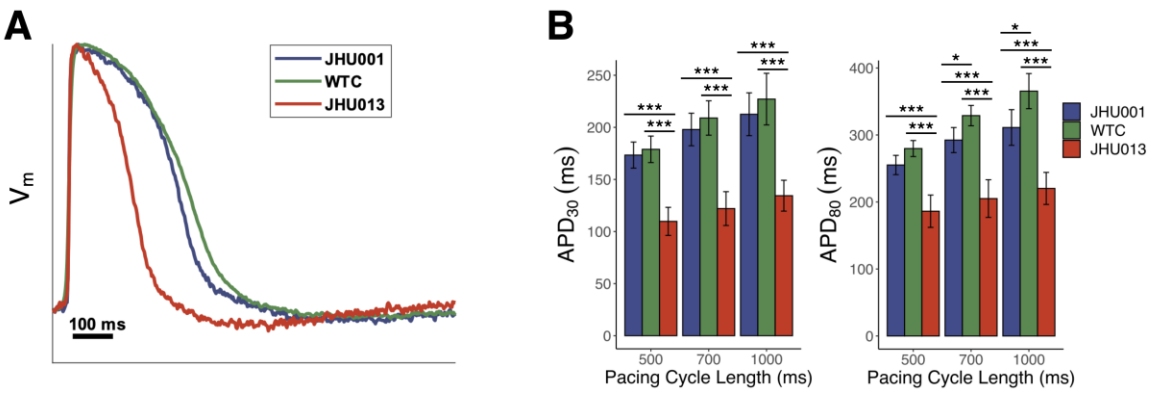

Figure 2.7 Action potential shortening in *DSG2*-mutant iPSC-CM monolayers. (A) Representative voltage traces for JHU013 and both control lines. (B) Action potential duration (APD) measured at 30% and 80% repolarization at three different pacing rates. JHU001 (n=8), WTC (n=13) JHU013 (n=9).

Optical mapping experiments showed similar conduction velocities in all lines and no differences in conduction heterogeneity, as measured by the relative standard deviation (RSD) of conduction velocity values within each sample (Fig. 2.8A,B). There were also no significant differences in relative upstroke velocity (Fig. 2.8C,D). However, we did find that the upstroke velocity in the JHU013 iPSC-CMs was more variable across each monolayer on average (RSD= 0.27±0.1 in JHU013 vs 0.15±0.01 in JHU001 and 0.13±0.06 in WTC at 1000 ms pacing, Fig. 2.8D). This implies substantial spatial heterogeneity of excitability or electrical coupling in these cells. The latter seems less likely because of the lack of measurable differences in conduction heterogeneity, but small differences in heterogeneity could potentially be masked by the safety factor of the syncytium.

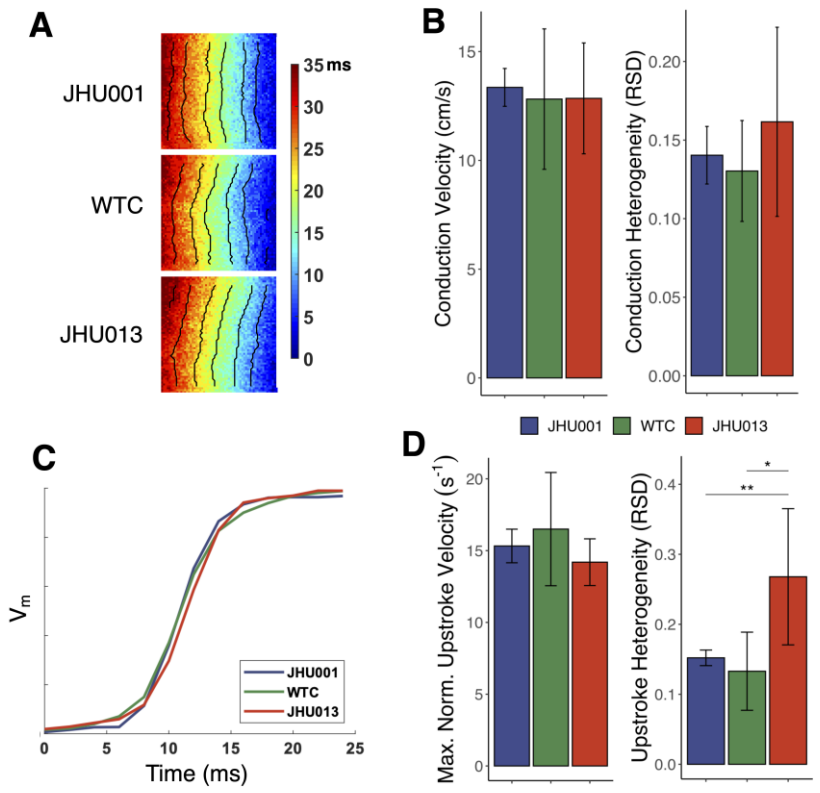

Figure 2.8 Normal conduction but increased upstroke heterogeneity in JHU013 iPSC-CM monolayers. (A) Representative activation maps. Isochrone lines spaced 5 ms apart. (B) Mean conduction velocity and conduction heterogeneity measurements at 1000 ms pacing. Heterogeneity calculated as the relative standard deviation (RSD) of all measurements within each sample. (C) Traces of the action potential upstroke in all three lines. (D) Relative upstroke velocity measured at 1000 ms pacing and spatial heterogeneity of upstroke velocity. JHU001 (n=8), WTC (n=13) JHU013 (n=9).

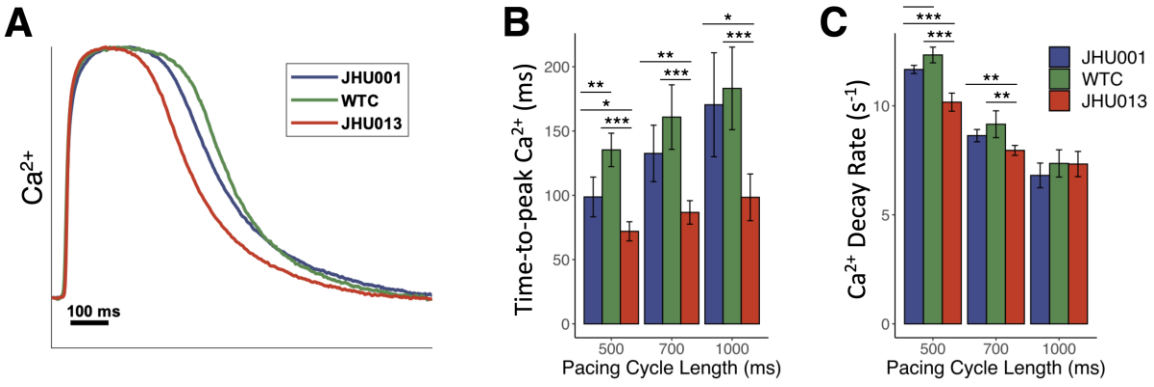

Figure 2.9 Altered calcium transient behavior in *DSG2*-mutant iPSC-CMs. Representative calcium traces. (B) Average time-to-peak Ca^{2+}. (C) Ca^{2+} decay rate λ (i.e. τ^{-1}). JHU001 (n=10), WTC (n=7), JHU013 (n=9).

Mapping the relative intracellular calcium concentration in iPSC-CM monolayers during excitation revealed significant differences in calcium dynamics. Time-to-peak Ca^{2+} was considerably shorter in JHU013 CMs than in controls (98±18 ms in JHU013 vs 170±40 and 183±32 ms in JHU001 and WTC; Fig. 2.9B). At faster pacing rates JHU013 CMs also displayed slowed Ca^{2+} transient decay (Fig. 2.9C), though this effect was not observed at 1000 ms pacing.

2.3.3 Biomolecular characterization of JHU013 iPSC-CM

We first characterized the expression and localization of key desmosomal proteins and cardiac ion channels in the *DSG2*-mutant iPSC-CM model. Specifically, RT-qPCR analysis showed that mRNA expression of *DSG2* was significantly reduced in the mutant iPSC-CMs compared to both JHU001 and WTC (35.2% and 49.6% lower expression, respectively), using a primer targeted to a site upstream of the *DSG2* c.2358delA location (Fig. 2.10). Sodium and potassium channel genes *SCN5A* and *KCNQ1* were more highly expressed in JHU013 CMs compared to JHU001, but not WTC, as was Ca^{2+}-handling gene *CAMK2A*. In other Ca^{2+}-handling genes, we observed increased *RYR2* expression and reduced *CASQ2* and *SLN* expression in JHU013 CMs compared to controls. These changes are very interesting in consideration of the different calcium transient dynamics we observed in JHU013 CMs.

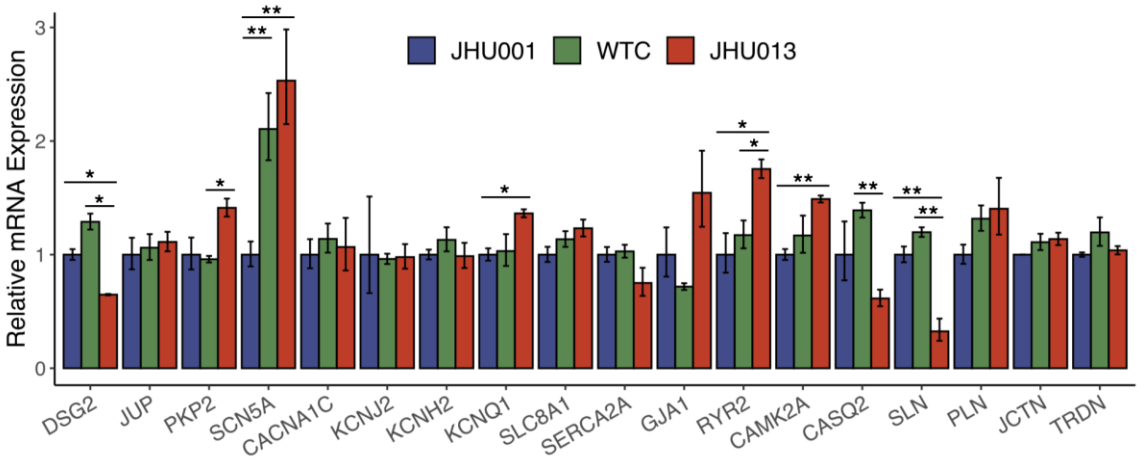

Figure 2.10 RT-qPCR analysis of JHU013 CMs. Expression calculated relative to JHU001. n=3 for each group, with three technical replicates per sample.

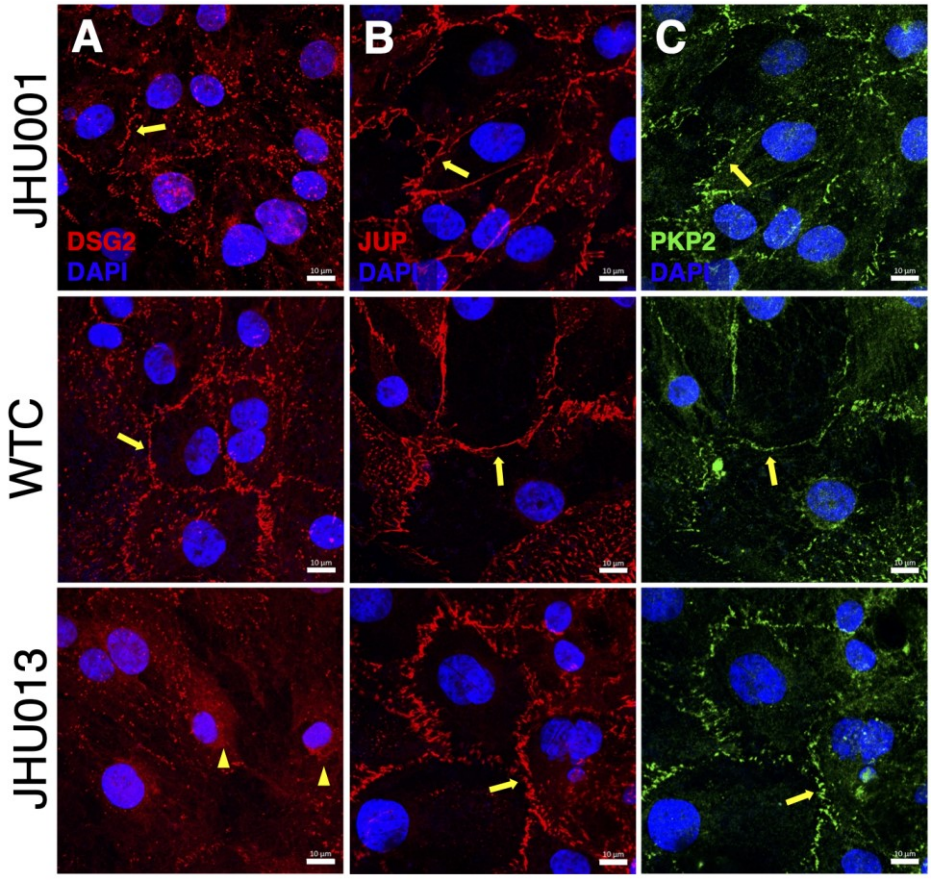

Figure 2.11 Visualization of desmosomal components in iPSC-CMs. Confocal images of iPSC-CM monolayers stained for desmosome components: (A) desmoglein-2, (B) plakoglobin, and (C) plakophilin-2. Yellow arrows highlight presence of desmosomal proteins at cell-cell boundaries; yellow arrowheads highlight perinuclear localization of DSG2. White scale bars: 10 μm.

Immunofluorescent imaging illustrated reduced overall signal intensity of desmoglein-2 in JHU013 iPSC-CMs, in addition to reduced localization at the cell membrane in conjunction with perinuclear accumulation (Fig. 2.11A). The latter finding suggests defects in trafficking of DSG2 in these cells, as has been previously reported in *Dsg2*-mutant mouse models and in human ARVC patients with pathogenic variants in *DSG2* [40,67]. Western immunoblot analysis demonstrated much lower expression of full-length (~130kDa) desmoglein-2 in JHU013 CMs but retained lower molecular weight bands of desmoglein-2-immunopositive protein (Fig. 2.12). This implies either enhanced degradation of desmoglein-2 or substantial translation of incomplete protein.

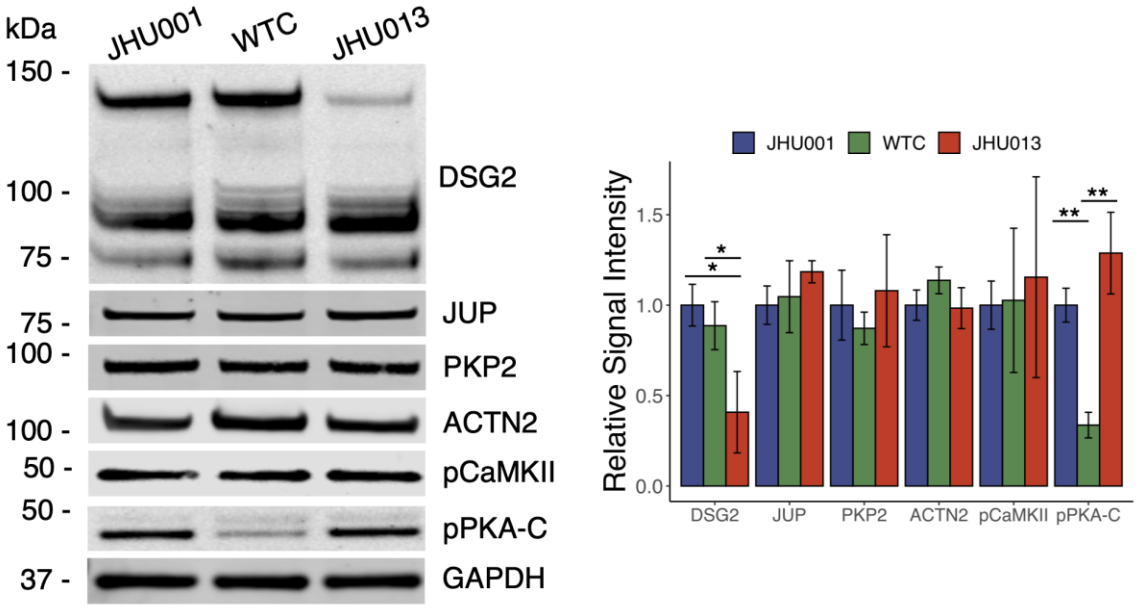

Figure 2.12 Western blot analysis of desmosomal and contractile proteins in JHU013 and control iPSC-CMs. Whole lysate Western immunoblots of JHU013 and JHU001 iPSC-CMs, probed for desmosomal proteins, α-actinin (ACTN2), and calcium handling regulators pCaMKII and pPKA-C. Quantification of signal intensity relative to GAPDH and normalized to JHU001. DSG2 quantified using the full-length 130 kDa band. n=3 for each cell line.

We found mRNA abundance of desmosomal components *PKP2* and *JUP* to be slightly increased and unaffected, respectively, in JHU013 cells, but observed no difference in protein expression of either gene product by immunostaining (Fig. 2.11B,C) or Western blot studies (Fig. 2.12). We also measured the abundance of two key calcium handling proteins, Ca^{2+}/calmodulin-dependent kinase II and PKA-C in their active forms (pCaMKII and pPKA-C, respectively) and found pCaMKII abundance was not significantly different among the three lines and that JHU013 iPSC-CMs displayed similar levels of pPKA-C compared to JHU001, but more than WTC.

Immunostaining for α-actinin and cardiac troponin I in JHU013 iPSC-CMs showed narrower myofibrils than normal iPSC-CMs (Fig. 2.13), although Western blots demonstrated that α-actinin protein abundance was not altered in JHU013 CMs. To assess myofibril diameter, we measured the length of Z-lines, denoted by α-actinin immunopositivity, in randomly selected regions across several high magnification confocal images. We found myofibril diameter in both control lines to be in agreement with measurements reported in the literature [67] but confirmed that Z-line length, i.e. myofibril width, was significantly shorter in JHU013 CMs compared to controls ($0.76 \pm 0.08\ \mu$m in JHU013 vs. $1.17 \pm 0.2\ \mu$m in JHU001 and $1.22 \pm 0.23\ \mu$m in WTC; Fig. 2.13).

In search of further validation for the theory that myofibril organization is dysregulated in JHU013 iPSC-CMs, we queried an RNA-sequencing dataset which was initially generated as part of the investigation detailed in Chapter 3.

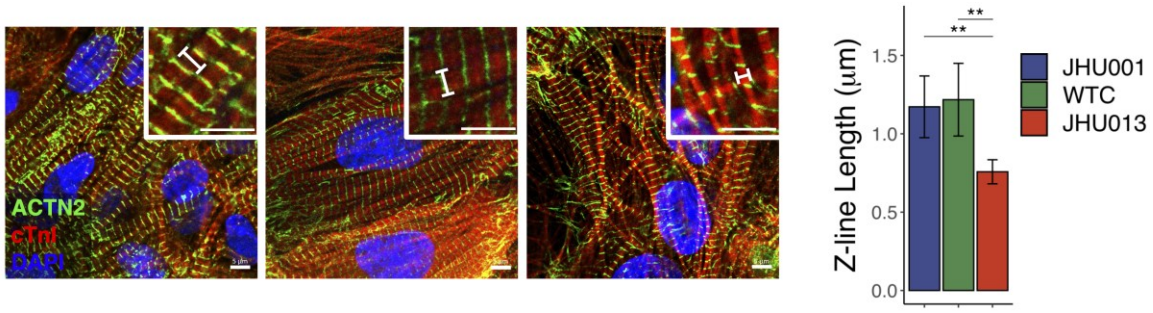

Figure 2.13 Visualization of contractile architecture in iPSC-CMs. Confocal images of iPSC-CM monolayers stained for α-actinin and cardiac troponin T. Bar graph depicts the mean Z-line lengths quantified from α-actinin immunostaining. Shorter Z-lines in JHU013 cells correspond to narrower myofibrils. Two regions were randomly selected for quantification from three different images of each line. White scale bars: 5 μm. While length markers highlight sarcomere width in each image inset.

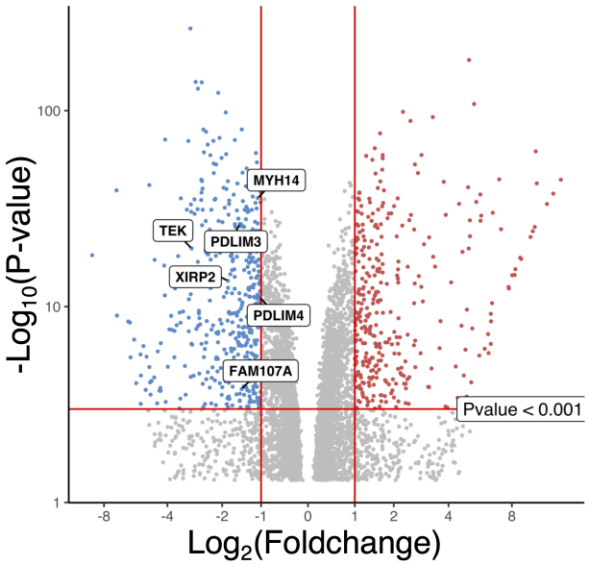

GO Accession	GO term name
GO:0032432	actin filament bundle
GO:0097517	contractile actin filament bundle
GO:0042641	actomyosin

Figure 2.14 Contraction-related genes are differentially expressed in JHU013 iPSC-CMs. A volcano plot showing the expression genes associated with the three contraction-related GO terms (listed to the right) identified in RNA-seq enrichment analyses. Each point represents a gene that was found to be differentially regulated between JHU013 and JHU001 iPSC-CMs. Red points to the right of the vertical red lines are genes which were upregulated in JHU013 by at least two-fold, and blue points to the left are genes which were downregulated in JHU013 by at least two-fold. The horizontal red line applies a more stringent cutoff value so that everything above that line has a p-value < 10^{-3}.

The dataset includes bulk RNA-seq data for JHU001 and JHU013 iPSC-CMs harvested on differentiation day 35 (see Section 2.2.4 for methods details). We compared the data for JHU001 and JHU013 iPSC-CMs, identified all genes that were differentially expressed between them, and performed a gene ontology enrichment analysis to get a sense of which gene sets are particularly different between the two lines. In that analysis three of the top ten most over-enriched gene ontology terms were: actin filament bundle (GO:0032432), contractile actin filament bundle (GO:0097517), and actomyosin (GO:0042641). This was noteworthy as actin filaments and actomyosin complexes are integral components of the myofibril structure. The volcano plot in Figure 2.14 highlights the genes from those three gene ontology sets that were the most differentially expressed between JHU001 and JHU013 iPSC-CMs in our analysis.

2.3.4 Effect of siRNA-mediated silencing of DSG2 expression

We next sought to interrogate the role that the *DSG2* c.2358delA mutation plays in mediating the biomolecular and electrophysiological changes observed in JHU013 iPSC-CMs as compared to the effects of overall *DSG2* expression. To achieve this, we used small interfering RNA (siRNA) to suppress expression of *DSG2* in JHU001 iPSC-CMs. After 72 hours, siRNA transfection of JHU001 iPSC-CMs substantially reduced *DSG2* expression at both the transcriptional and protein levels. The 81% decrease in mRNA abundance we measured (Fig. 2.15A) was a greater reduction than we saw in the JHU013 cells at baseline relative to controls.

We did not observe a significant change in the localization of desmoglein-2 in response to *DSG2* knockdown (DSG2-KD), nor did we find any effect on the expression or localization of plakoglobin (Fig. 2.15B).

DSG2 knockdown resulted in altered abundance of RNAs encoding several ion channels including reduced *SLC8A1* (I_{NCX}) and increased *KCNJ2* (I_{K1}) (Fig. 2.15A), but notably its effects on *SCN5A* and *KCNQ1* transcript levels, which were altered in JHU013 CMs (Fig. 2.10), were not statistically significant. Expression of calcium handling genes *RYR2*, and *SLN*, which were all differentially expressed in JHU013 CMs, were not significantly affected by *DSG2* suppression.

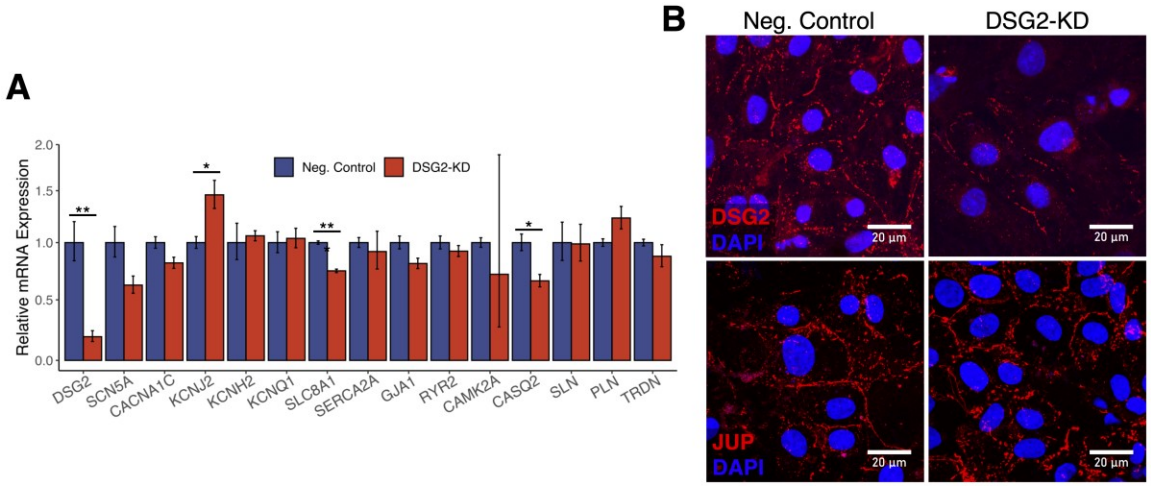

Figure 2.15 Effects of *DSG2* knockdown on gene expression in JHU001 iPSC-CMs. (A) Relative mRNA expression of key cardiac markers in iPSC-CMs, with and without *DSG2* knockdown. n=3 for each group. (B) Confocal images of JHU001 iPSC-CM monolayers stained for DSG2 and JUP. White scale bars, 20 μm.

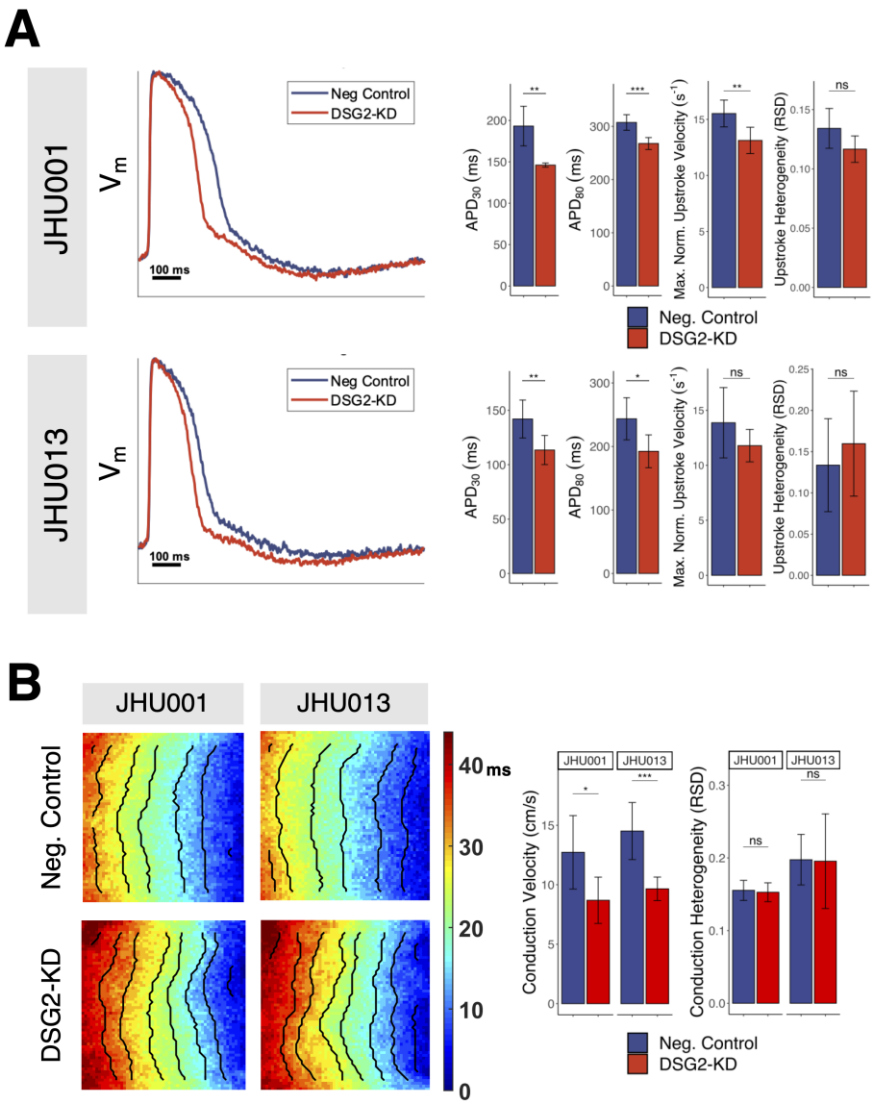

Figure 2.16 Action potential and conduction effects of *DSG2* knockdown. (A) Representative action potential traces are shown for JHU001 and JHU013 iPSC-CMs. Bar graphs depict summary statistics for action potential characteristics. (B) Isochrone maps for JHU001 and JHU013 iPSC-CMs and mean conduction velocity and conduction heterogeneity. All data shown is from recordings taken at 1000 ms pacing cycle length. JHU001: Neg. Control (n=9), DSG2-KD (n=8). JHU013: Neg. Control (n=5), DSG2-KD (n=5).

Optical voltage mapping showed that *DSG2* knockdown in wildtype iPSC-CM monolayers shortened the action potential duration (Fig. 2.16A). At 1000 ms pacing rates, APD_{30} was reduced by 47 ms and APD_{80} was reduced by 40 ms in JHU001

CMs, similar to the differences seen between untreated control and *DSG2*-mutant CMs. However, unlike our observation in JHU013 cells, *DSG2*-suppressed JHU001 cells displayed slower conduction velocities (Fig. 2.16B) and slower action potential upstroke velocity, without significant effect on the spatial heterogeneity of either parameter. Interestingly, similar action potential and conduction effects were observed in JHU013 iPSCs in response to *DSG2* knockdown (Fig. 2.16).

We also performed calcium mapping and discovered that calcium transients in JHU001 CMs were not substantially altered by *DSG2* knockdown; times-to-peak Ca^{2+} and Ca^{2+} decay rates were similar between treated and untreated monolayers (Fig. 2.17). In JHU013, there was also no observable effect on calcium decay, but there was a slight shortening effect on the time-to-peak Ca^{2+}.

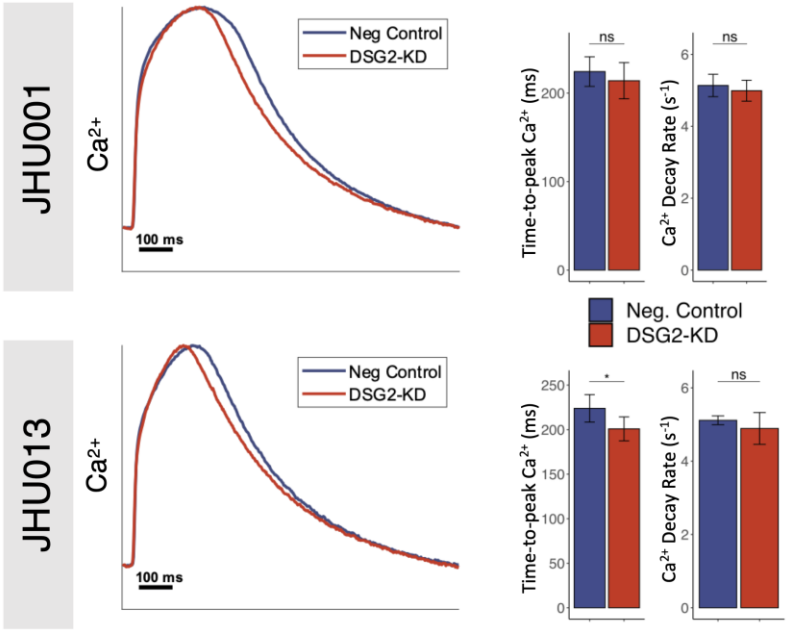

Figure 2.17 Calcium transient effects of *DSG2* knockdown. Representative Ca^{2+} traces are shown for JHU001 and JHU013 iPSC-CMs. Bar graphs depict summary statistics for calcium transient characteristics. All data shown is from recordings taken at 1000 ms pacing cycle length. JHU001: Neg. Control (n=9), DSG2-KD (n=8). JHU013: Neg. Control (n=9), DSG2-KD (n=9).

2.4 Discussion

In this chapter we established a novel patient-specific iPSC model of ARVC from an individual with a pathogenic variant in *DSG2*, the second most common gene associated with ARVC [68]. We performed a broad characterization of cardiomyocytes derived from these iPSCs, evaluating their biomolecular features as well as their electrophysiological behaviors in monolayer cultures. Our studies confirmed reduced *DSG2* expression and disrupted localization in JHU013 CMs, with no apparent changes in expression or localization of other key desmosomal components. We also found that these cells have aberrant electrophysiology and altered Ca^{2+} handling when compared to wildtype cells, including shortened action potential duration and time-to-peak calcium.

The *DSG2* c.2358delA variant results in a frameshift and early termination in the intracellular cadherin-like domain of *DSG2*, which would result in the loss of the C-terminus from proteins translated from that allele. It has been previously demonstrated that the distal C-terminal domains are critical in stabilizing desmoglein-2 at the cell membrane, and that deletion of those downstream regions results in increased protein internalization and consequently weakened cell-cell cohesion [69]. Our observations are consistent with loss of desmoglein-2 stability at the cell membrane and dysfunctional protein trafficking; we found that in JHU013 iPSC-CMs, desmoglein-2 accumulates intracellularly, primarily near the nucleus, whereas it was predominantly localized at myocyte-myocyte junctions in controls (Fig. 2.11).

Advanced ARVC has several well-established pathological markers in human myocardium; however, establishing a definition and criteria constituting a faithful *in vitro* model of ARVC has proven difficult. Some authors have proposed using reduced plakoglobin expression at cell boundaries as a key component of that definition, since this feature has been documented in both animal [40] and iPSC [70] models and has even been evaluated as a potential diagnostic marker in humans [23,24,71]. However, plakoglobin dysregulation has not been observed universally, and notably the extent of dysregulation has been variable among pathogenic variants studied [25,54]. In our model, plakoglobin expression was not appreciably altered in transcription, protein abundance, or in its localization, which conflicts with the use of plakoglobin as a universal marker of ARVC *in vitro* (Fig 2.10 and Fig. 2.11). Although, given that iPSC-CMs do not form mature intercalated discs at baseline, these results are difficult to extrapolate to human and animal models, and it is still very possible that plakoglobin disruption is a useful marker for advanced disease [56].

Interestingly though, cytoskeletal organization did seem to be affected in JHU013 iPSC-CMs. We found myofibrillar diameter was significantly reduced in *DSG2*-mutant cells compared to both control lines, which hints at disruption in the production, localization or assembly of myofibrillar proteins. We did not find evidence that cardiac troponin T or α-actinin protein abundance was altered, but RNA-sequencing revealed that genes involved in regulating myofibril assembly were expressed very differently in JHU013 CMs compared to control (Fig. 2.14).

Studies of myocardial biopsies of ARVC patients have shown altered or degraded myofibrillar structure and some forms of ARVC are associated with myofibrillar myopathy [72–74]. Irregular organization of myofibrils has been noted in at least two previous studies of ARVC in iPSC-CMs; one study used a *PKP2*-mutant iPSC line and the other used a line with a rare mutation in *OBSCN* [75,76]. If similar myofibrillar differences continue to be identified in diverse iPSC models of ARVC, it could offer a novel criterion for defining ARVC phenotype *in vitro*.

Prior studies of ARVC iPSC-CMs have reported a range of electrophysiological characteristics. An iPSC-CM model harboring a compound pathogenic variant in *PKP2* showed abnormal sodium channel function as indicated by slowed upstroke speeds and reduced total sodium current [54]. A study of DSG2 p.G638R iPSC-CMs found similar defects, and another study evaluating iPSC-CMs derived from a patient with a rare homozygous *DSG2* variant (p.R119X) found very slow conduction velocities compared to an isogenic line with one wildtype *DSG2* allele [31,77]. In our model, we did not observe any differences between the *DSG2*-mutant CMs and control CMs in terms of their conduction velocity or relative action potential upstroke velocity, though we did find that the JHU013 CMs displayed much greater upstroke heterogeneity within each monolayer compared to the controls (Fig. 2.8). Because the cardiomyocyte monolayers used in this study possess electrically connected myocytes and display syncytial behavior, our metrics of excitability also reflect source-load current effects and, therefore, can differ from single-cell measurements of excitability. Nevertheless, when considered alongside

our finding that expression of the primary sodium channel (*SCN5A*) was not reduced in JHU013 cells, these results are inconsistent with major sodium current dysfunction as reported in those prior studies.

In the study of DSG2 p.G638R iPSCs, the authors also found reduced expression and activity of multiple potassium currents, including I_{to}, I_{SK}, and I_{KATP} [31], but they did not report any significant differences in repolarization dynamics in those cells. In our study we measured substantially shortened action potential durations in our *DSG2*-mutant CMs as compared to controls (Fig. 2.7), however the mechanisms responsible for that difference are not entirely clear. JHU013 CMs displayed slightly higher mRNA expression of *KCNQ1*, the gene encoding the channel responsible for I_{Ks}, which is one of the major repolarizing currents of the action potential (Fig. 2.10). JHU013 CMs also had significantly shorter time-to-peak calcium, which could reflect reduced influx of L-type calcium current resulting from the shortened action potential duration or could itself potentially be a contributor to those shortened action potentials (Fig. 2.9).

Another possible explanation for the differences in action potential characteristics in our model compared to other *DSG2*-mutant models may be related to ion channel trafficking. Desmoglein-2 and plakophilin-2 trafficking has been linked to the expression and trafficking of several key ion channels, including Nav1.5, through the formation of macromolecular complexes [26,78]. The different excitability effects in our model as compared to other *DSG2*-mutant models, could

be explained by variation in how different mutations affect the ability of desmoglein-2 to form and influence these complexes.

Interestingly, our action potential findings in JHU013 iPSC-CMs is consistent with the ECG data available for the donor. The donor of the JHU013 line has shown evidence of T wave inversions on ECG for decades (Fig. 2.1). T wave inversions are considered to be indicative of aberrant repolarization behavior, and their presence satisfies the 2010 ARVC task force criteria for "Repolarization abnormalities" (Table 2.1) [79]. Meanwhile, her clinical history offers no sign of altered cardiac depolarization, such as epsilon waves or prolongation of terminal activation duration on ECG. Our iPSC-CM experiments found altered repolarization (shortened APD) but no defects in depolarization (unchanged conduction and upstroke velocity). While inverted T waves do not imply globally shortened APDs in the heart (in that case, we would expect to see QT interval shortening), they can reflect abnormalities in the dispersion of APDs throughout the organ, which is difficult to capture in an iPSC-CM monolayer model, but would be consistent with our results.

Abnormal Ca^{2+}-handling can promote arrhythmia via a number of different mechanisms and has been implicated in a broad range of acquired and inherited cardiovascular diseases [80]. Several studies have suggested that calcium signaling pathways play an important role in arrhythmia associated with ARVC, in particular [45,81]. Previously reported iPSC-CM models of ARVC have exhibited slower calcium relaxation [53], disrupted calcium homeostasis [46], and increased

susceptibility to epinephrine-induced proarrhythmic calcium events (i.e. delayed afterdepolarizations) [31]. Our findings further support the theory that cardiomyocyte calcium regulation is altered in ARVC. In addition to displaying much shorter time-to-peak Ca^{2+} and slower Ca^{2+} decay (Fig. 2.9), RT-qPCR experiments showed overexpression of *RYR2* and reduced expression of *SLN*, which encode the ryanodine receptor and sarcolipin, respectively (Fig. 2.10). Ryanodine receptors regulate calcium release from the sarcoplasmic reticulum (SR), and sarcolipin regulates SR calcium uptake; both are critical for calcium homeostasis [82–84]. High levels of cytosolic Ca^{2+} has been shown to enhance I_{Ks} in rabbit cardiomyocytes, which could possibly explain the action potential duration shortening observed in JHU013 iPSC-CMs [85].

Ultimately there are many ways in which the cellular- and syncytial-level electrophysiological differences we observed in JHU013 iPSC-CMs could increase susceptibility to ventricular arrhythmia if replicated in patient myocardium. The shortened action potential durations in JHU013 CMs implies that the cells are in their refractory period for less time than the controls [86]. Therefore, these cells would be more likely to respond to an ectopic beat which could allow an event that would normally be damped by refractory myocardium to propagate into fulminant arrhythmia [87,88]. We can infer from the upstroke velocity data that excitability is more heterogeneous in JHU013 monolayers than in control. Heterogeneity of excitability is known to contribute to arrhythmia by increasing the susceptibility of the substrate to unidirectional block and consequent reentry [89]. Our findings also

suggest that Ca^{2+} homeostasis is disrupted in the *DSG2*-mutant iPSC-CMs, which can contribute to increased occurrences of early and delayed afterdepolarizations. This “triggered activity” is one of the major mechanisms by which arrhythmias are initiated [90,91].

In our model, overall expression of *DSG2* was lower in the JHU013 CMs than in the controls. This made it very difficult to assess which of the effects we observed were related to the specific *DSG2* mutation (and defective protein product) we are studying in this patient and which effects might be linked to an across the board reduction in *DSG2* expression. To isolate the contributions of a gross difference in *DSG2* expression from the potentially dominant-negative effects of the c.2358delA variant, we used siRNA targeted against *DSG2* mRNA to transiently suppress *DSG2* expression without introducing the potential for truncated protein translation. This method achieved an approximately 80% reduction in *DSG2* mRNA abundance in JHU001 CMs. *DSG2* knockdown in JHU001 CMs resulted in shortened action potential durations but had little effect on Ca^{2+} dynamics. The action potential changes are quite similar to the behavior seen in JHU013 iPSC-CMs, but mRNA expression patterns suggest that these could be the result of different mechanisms. While JHU013 iPSC-CMs expressed more of the gene encoding I_{Ks} compared to control, *DSG2* knockdown did not alter expression in that gene but instead resulted in increased expression of *KCNJ2*, which encodes I_{K1}. RT-qPCR data also offers an explanation for the minimal effects of *DSG2* knockdown on calcium dynamics in these cells. Although expression of *CASQ2* was reduced by *DSG2* knockdown, the

other calcium handling genes that were differentially regulated in JHU013 cells – *RYR2* and *SLN* – were not affected. While we observed no conduction differences between JHU013 and control iPSC-CMs at baseline, we found that *DSG2* knockdown caused conduction slowing in both control and *DSG2*-mutant lines (Fig. 2.16). This slowing could be due to diminished intercellular connectivity, as reduced expression of *DSG2* can disrupt connexin-43 localization; indeed, one study showed that mice with a cardiospecific knockout of *Dsg2* developed prolonged PR and QRS intervals on ECG recordings, indicative of significant conduction delay [21].

The fact that *DSG2* knockdown produced similar levels of conduction slowing in JHU001 and JHU013 iPSC-CMs while we saw no difference in baseline conduction between those two lines suggests that direct suppression of *DSG2* expression is more disruptive of conduction than the *DSG2* c.2358delA variant alone. Though, it is worth noting that these knockdown experiments measured only acute reductions in *DSG2* expression and longer-term studies, such as germ-line knockouts, could reveal different effects.

2.5 Conclusion

iPSC-CMs derived from an ARVC patient with a familial *DSG2* variant differ from controls substantially with regard to their biomolecular and electrophysiological phenotypes. They display altered expression of *DSG2* and several important ion channels and calcium-handling genes as well as narrower, more disorganized

myofibrils. These cells also exhibit shortened action potentials and aberrant calcium transient dynamics, each of which could make the myocardial substrate more susceptible to dangerous arrhythmias, though we found no evidence of defects in excitability as reported in other iPSC-CM models. Finally, global suppression of *DSG2* expression recapitulates some, but not all, of these phenotypic differences, leaving open the possibility of a dominant-negative mechanism associated with *DSG2* c.2358delA pathophysiology.

Chapter 3 – Establishing an isogenic control for JHU013 iPSC line

3.1 Background

The use of patient-derived iPSCs for modeling disease has expanded rapidly since the technology was first developed. Most often, controls for these studies are selected from age-matched, ideally sex-matched [92], unrelated healthy control lines (as we did in Chapter 2) or from unaffected family members of the disease line donor. However, these control lines can be suboptimal due to differences in genetic background and other confounders [93,94]. Advances in genome editing technology like CRISPR have allowed for the introduction of highly targeted genetic mutations into iPSCs, which has been leveraged for disease models in two primary ways; some investigators have introduced disease-associated mutations into

healthy iPSC lines to generate a disease model [95,96], while others have used genome editing to alter or "correct" the putatively pathogenic gene in a patient-derived diseased iPSC line [77,97].

In the work detailed in this chapter, we sought to optimize our ARVC iPSC model by generating an isogenic control line for JHU013 iPSCs. To do this, we used a genome editing procedure based on CRISPR-Cas9 to replace the *DSG2* allele harboring the c.2358delA mutation, with a wildtype *DSG2* sequence. We then compared the phenotypes of the isogenic control iPSCs to both disease and wildtype lines and performed a range of quality control experiments to assess the usefulness of the generated control.

3.2 Methods

3.2.1 Genome editing of JHU013 iPSCs

Genome editing was performed using a CRISPR-Cas9 protocol based on previously published work [98]. Guide RNAs were designed with the assistance of the Broad institute GPP sgRNA Designer. gRNA/Cas9-GFP structures were transfected into JHU013 iPSC via neon electroporation, and two days later, the cell population was sorted in a live cell fluorescence-activated cell sorter for GFP-expression. GFP-positive cells were plated at single-cell density on 100 mm petri dishes coated with laminin 521 (Flexcell, Burlington, NC, USA) and allowed to expand for six days. Colonies were then picked, plated in 24-well plates and

expanded to confluence twice. At that point cells were passaged, and half of the cells from each colony were re-plated into 6-well plates while the other half were sent for karyotyping and Sanger sequencing (performed by the Johns Hopkins Genetic Research Core Facility) to look for *DSG2* gene correction. Clones with normal *DSG2* genotype (Fig. 3.1) were then further expanded and banked in cryogenic storage. We refer to this edited cell line as JHU013-Corrected or "JHU013-C".

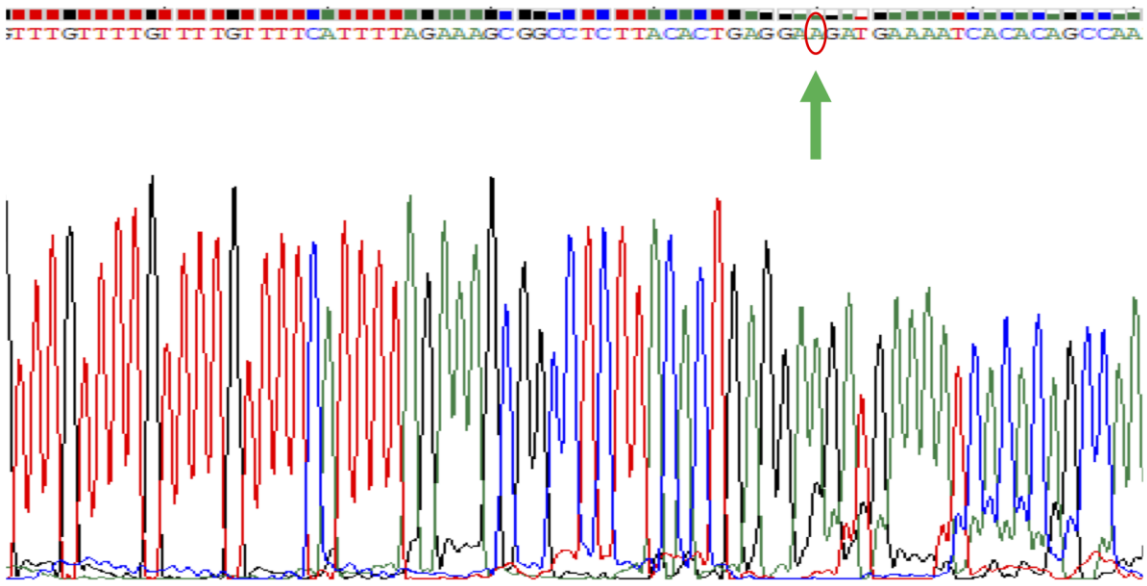

Figure 3.1 Sanger sequencing of *DSG2* in an edited clone of JHU013 iPSC. Green arrow and red circle highlight the adenine in position 2358 of the *DSG2* gene, which is present here in JHU013-C iPSCs, whereas this nucleotide is deleted on one allele in unedited JHU013 iPSCs (Fig. 2. 4).

3.2.2 Electrophysiological studies

Optical mapping studies and beat rate analysis were performed as described in Section 2.2.5.

To assess beat rate, high-speed video recordings were taken using an inverted microscope set up inside of an incubator to allow tight control of temperature and humidity. After a plate containing iPSC-CM monolayers was allowed to equilibrate in the incubator, three separate 30 second recordings were taken of each well.

The data were then analyzed using a custom MATLAB script which identified a reference frame when the cells are at rest and quantifies the total deviation from that reference frame, producing a waveform that correlates with the beating of the monolayers. After denoising, the total number of peaks was divided by the duration of the recording to produce the beating rate, and the standard deviation of the time between each pair of adjacent peaks was used to assess beat-to-beat variability.

3.2.3 Biomolecular assays

Immunocytochemistry and RT-qPCR analyses were performed as described in Section 2.2.3.

3.2.4 Next-generation sequencing

DNA extraction, preparation and sequencing for whole exome sequencing studies were performed by the Johns Hopkins Genetics Research Core Facility. That service also performed the initial data analysis including aligning the sequences to the genome and annotating genetic variants.

RNA-sequencing and analysis were performed as described in Section 2.2.4.

3.2.5 Statistics

Unless otherwise indicated, all data are presented as mean ± standard deviation of the mean, calculated in R. Continuous variables were compared using unpaired, unequal variance Student's t-test with a Holm-Bonferroni family-wise error correction. $P < 0.05$ in two-tailed analysis was considered significant.

3.3 Results

3.3.1 Basic characterization of genome-edited JHU013 iPSC line

Although we see significant phenotypic differences in the JHU013 line compared to wildtype controls, these experiments do not completely rule out the potential influence of genetic background on iPSC-CM behavior. Our group therefore sought to generate an "isogenic control" which would be genetically identical to JHU013 except for a corrected *DSG2* genotype (i.e. two wildtype *DSG2* alleles). To do this we employed CRISPR-Cas9 and nonhomologous end joining to edit the genome of JHU013 iPSCs.[*] We then expanded the edited cells and screened clones for a homozygous normal *DSG2* gene. We refer to this line as "JHU013-Corrected" or "JHU013-C".

We next applied our cardiogenic differentiation protocol to the JHU013-C iPSCs to generate iPSC-CMs and set out to characterize these cells as we did for the other

[*] Gene editing was planned and executed primarily by Deborah DiSilvestre in the Tomaselli laboratory and Adriana Blazeski.

iPSC lines, beginning with electrophysiological characterization. Analysis of optical voltage mapping recordings found that JHU013-C iPSC-CMs displayed action potential durations that were much longer than JHU013 CMs but similar to JHU001 control CMs (APD_{80} = 339±7 ms in JHU013-C vs. 331±27 ms in JHU001 and 214±25 ms in JHU013 at 1000 ms paced cycle length; Fig. 3.2A,C-D). These results aligned with our expectations of a "corrected" phenotype in the JHU013-C line. However, we also observed that the conduction velocities of JHU013-C CMs were much slower than both JHU013 and JHU001 (CV = 6.6±0.3 cm/s in JHU013-C vs. 13.2±0.9 cm/s in JHU001 and 12.8±2.5 cm/s JHU013 at 1000 ms paced cycle length; Fig. 3.2B). This unexpected finding was consistent across multiple clones and multiple rounds of differentiation and mapping.

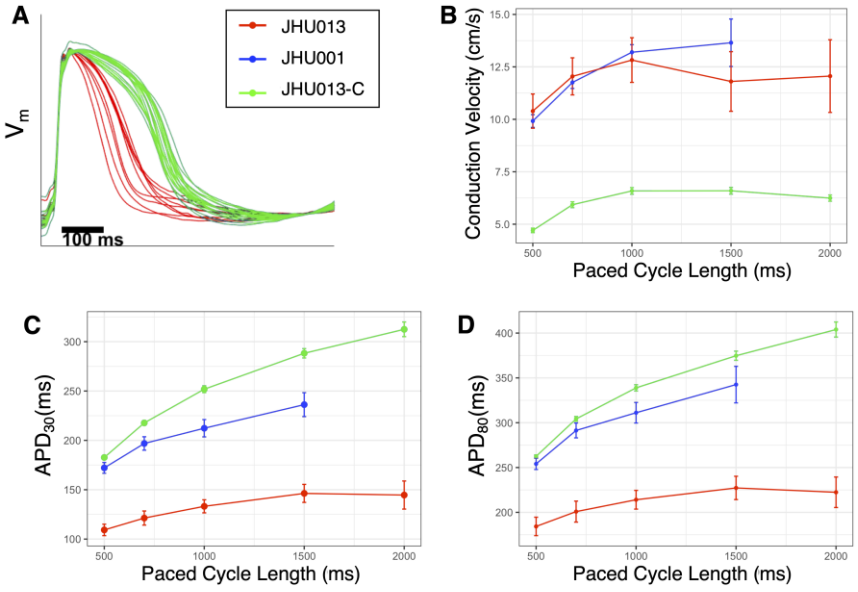

Figure 3.2 Action potential characteristics of JHU013-C iPSC-CMs vs JHU013 and JHU001. (A) Normalized action potential traces for JHU013 and JHU013-C iPSC-CMs; all samples included in this analysis have been overlaid. (B) Mean conduction velocity measurements from 500 ms to 2000 ms paced cycle lengths. (C,D) Mean APD_{80} and APD_{30} measurements. For all figures, JHU013 (n=9), JHU013-C (n=14), JHU001 (n=9).

Calcium mapping provided further unexpected results, and we discovered that the calcium time-to-peak (TTP-Ca^{2+}) was much longer in JHU013-C CMs compared to both JHU013 and JHU001 despite the fact that the CRISPR-corrected cells had similar action potential durations to the wildtype line (TTP-Ca^{2+} = 224±25 ms in JHU013-C vs 118±15 ms in JHU001 and 85±7 ms in JHU013 at 700 ms paced cycle length; Fig. 3.3). Calcium decay kinetics showed a wider variance in JHU013-C monolayers but the mean decay rate was not significantly different from the other two lines (λ = 8.8±0.5 ms in JHU013-C vs 8.8±0.2 ms in JHU001 and 8.3±0.2 ms in JHU013 at 700 ms paced cycle length; Fig. 3.3).

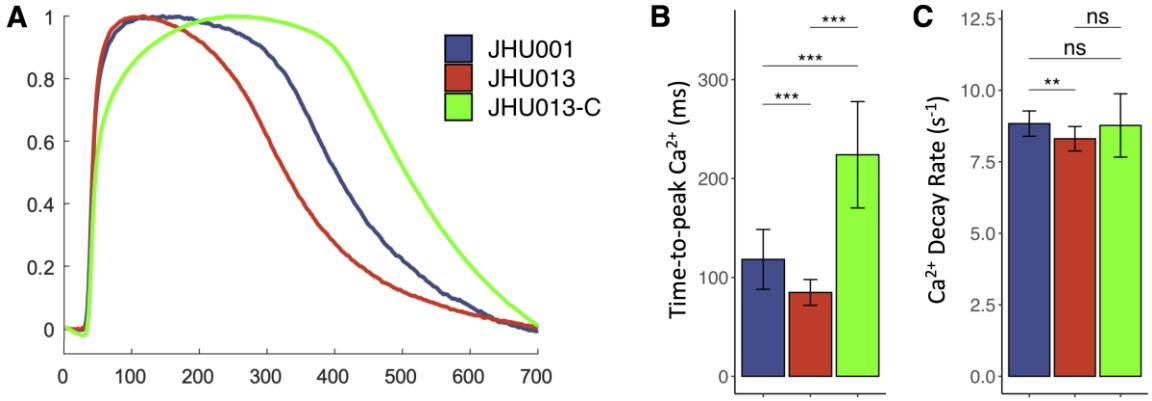

Figure 3.3 Calcium transient characteristics of JHU013-C iPSC-CMs. Measured via optical mapping with Rhod-2 AM. (A) Normalized calcium traces for JHU001, JHU013 and JHU013-C iPSC-CMs. (B) Mean time-to-peak calcium. (C) Calcium decay rate (λ). All data shown measured at 700 ms paced cycle length. JHU001 (n=23), JHU013 (n=22), JHU013-C (n=15).

Seeking to explain the unexpected electrophysiological differences observed in JHU013-C CMs, we next performed biomolecular characterization via RT-qPCR and immunocytochemistry. We first isolated RNA from wildtype, *DSG2*-mutant, and CRISPR-corrected iPSC-CMs and performed RT-qPCR experiments. As we might

have expected, we found that *DSG2* expression in JHU013-C CMs was increased relative to JHU013 but was somewhat reduced relative to JHU001 (compared to JHU001, RQ = 0.66±0.8 in JHU013-C vs 0.27±0.07 in JHU013; Fig. 3.4A). That pattern of JHU013-C expression falling in between JHU001 and JHU013 was reflected in several measured markers including *SCN5A*, *CACNA*, and *PKP2*; in all of these genes, JHU013 expression was measured to be greater than JHU013-C which in turn was greater than JHU001. These results might be expected in a line with a partially corrected phenotype, and they did not offer a good explanation of the major electrophysiological differences we observed in the CRISPR-edited cells. It is also notable that *GJA*, which encodes connexin-43, was similarly expressed in all three lines.[*] The conduction velocity defect could still be due to post-transcriptional differences in connexin-43 expression and could also be attributable to another mechanism altogether.

We also used immunostaining to evaluate the expression of desmoglein-2 in JHU013-C CMs. For these experiments we utilized two different primary antibodies; one antibody targets an epitope in the extracellular domain of DSG2 (which is not affected by the *DSG2* c.2358delA variant) while the other targets the C-terminus on the intracellular portion of the protein (this region is expected to be truncated by the *DSG2* c.2358delA mutation).

[*] Preliminary immunostaining suggested that Cx-43 expression at the cell membrane was lower in JHU013-C CMs compared to JHU001 and JHU013, but these experiments were not conclusive.

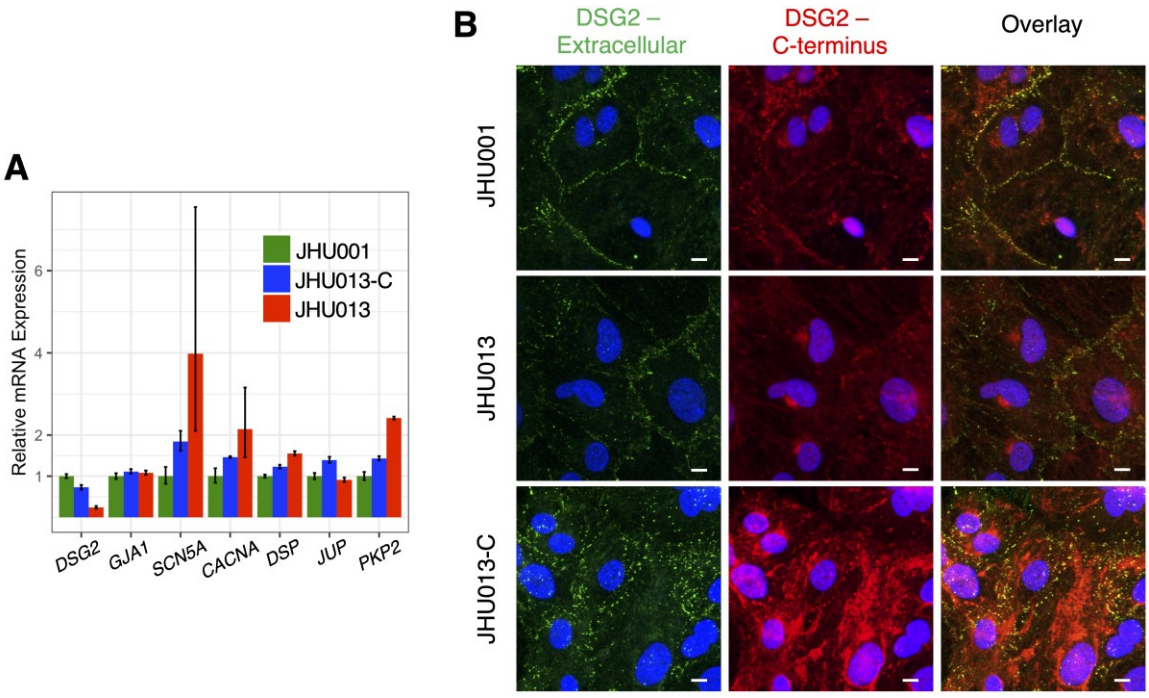

Figure 3.4 Biomolecular evaluation of JHU013-C iPSC-CMs. RT-qPCR analysis. mRNA foldchange expression is shown relative to JHU001. n=3 for all groups. (B) iPSC-CM monolayers stained for desmoglein-2 with probes targeting extracellular and intracellular (C-terminus) domains of the protein. The C-terminal domain is expected to be absent in proteins translated from an allele with the *DSG2* c.2358delA variant. White scale bar, 5 µm.

In confocal images, JHU001 cells displayed immunopositivity for both antibodies primarily at the intercellular membranes as would be expected (Fig. 3.4B). Localization was clearly disrupted in the JHU013 CMs as we've seen previously, with staining of both antibodies much less pronounced at the cell membranes; though interestingly, there was much more perinuclear accumulation of the desmoglein-2 C-terminus in these cells than there was for the extracellular portion. JHU013-C cells, though, showed markedly aberrant desmoglein-2 expression. Overall immunopositivity was much higher than in either of the other two lines, and while there was some expression at intercellular boundaries, the vast

majority of the signal was intracellular. This immunostaining data suggests that desmoglein-2 protein expression in JHU013-C was significantly higher than in JHU013, but that the CRISPR-edited cells retained a substantial defect in desmoglein-2 protein localization.

3.3.2 Genomic and transcriptomic evaluation of JHU013-C iPSC line

We next decided to perform bulk RNA-sequencing with the goal of generating a reasonable hypothesis as to the underlying causes of the unexpected behaviors in the JHU013-C cell line. We prepared five iPSC-CM samples each from JHU001, JHU013, and JHU013-C and sent them to an outside vendor (GENEWIZ, South Plainfield, New Jersey) for RNA isolation, library preparation and sequencing. The data was then mapped onto the human genome, and relative expression was calculated.[*]

The RNA-sequencing data made it very clear that the CRISPR-edited iPSC-CMs were phenotypically different from both the unedited *DSG2*-mutant line and the wildtype line. Figure 3.5A shows a heatmap of all genes that were found to be differentially expressed when comparing JHU013 and JHU013-C. Since JHU013 and JHU013-C theoretically share the vast majority of their genetic background, we expected that their overall expression patterns would be similar to each other, with perhaps a few key differences. However, as can be observed in that heatmap,

[*] RNA-seq data processing was performed by Suraj Kannan.

expression patterns in JHU001 and JHU013 were much more similar to each other than either of them was to JHU013-C, despite having completely unrelated genetic background. The same observation holds true when we limit the heatmap to a set of cardio-specific genes in Figure 3.5B.

To get an unbiased assessment of the similarity of the three lines, we performed a principle component analysis on the RNA-seq expression data. That analysis showed that on one set of genes, defined by component 2 (PC2 in Fig. 3.5C), JHU013-C expression fell in between JHU001 and JHU013; if JHU013-C had a corrected or partially corrected phenotype, we would expect to find a set of genes with this property, where expression is pulled toward the healthy control. However, in another set of genes defined by component 1 (PC1) JHU013-C expression was much different compared to both other lines, which, in turn, are very similar to each other. We performed a gene ontology enrichment analysis on the genes comprising PC1 and discovered that a number of the top ontology terms relate to cellular adhesion and extracellular matrix interactions (Table 3.1). Defects in these cellular processes, could potentially be driving the functional differences we observe in JHU013-C iPSC-CMs since changes in the composition of the extracellular matrix has been shown to modulate cardiomyocyte electrophysiology, calcium handling, and conduction [99,100], and loss of extracellular adhesion molecules can also cause conduction defects and changes to calcium channel function [96].

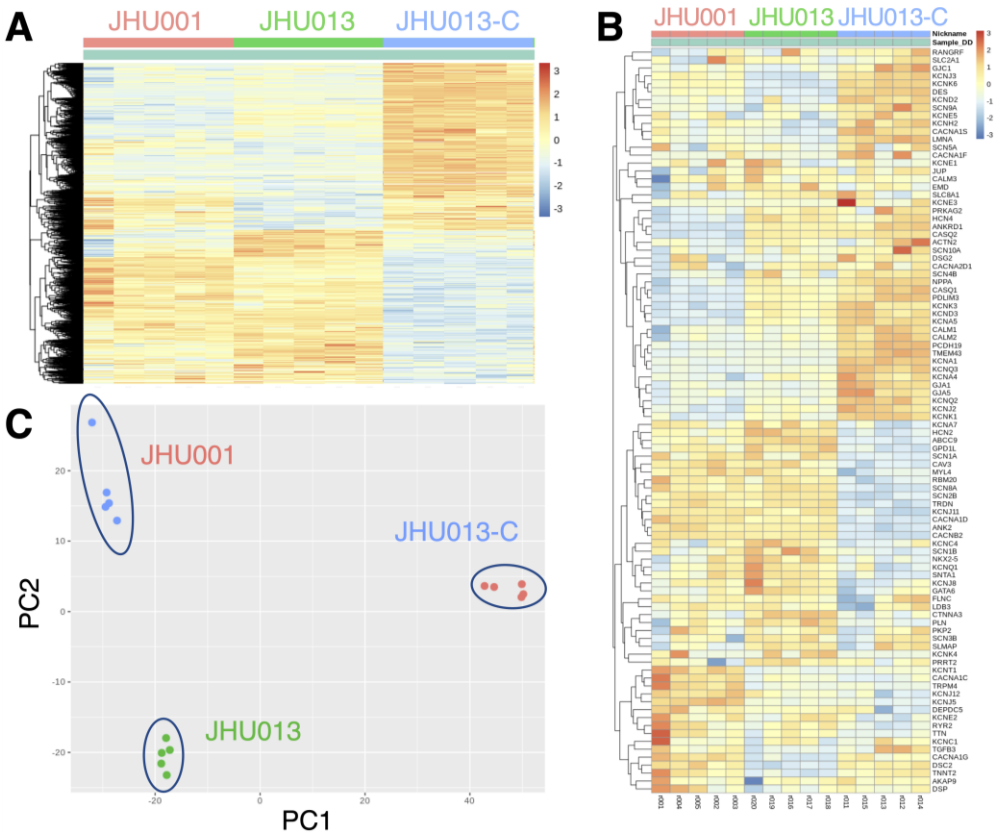

Figure 3.5 Preliminary analysis of JHU013-C RNA-sequencing data. (A) Heatmap displaying row-normalized expression of all genes found to be differentially expressed between JHU013 and JHU013-C CMs. (B) Heatmap displaying a set of genes key to CM function and electrophysiology. (C) A principle component analysis comparing the expression profiles of all three lines.

Top 10 GO Terms: PC1
Cell-matrix adhesion mediator activity (GO:0098634)
Platelet-derived growth factor binding (GO:0048407)
Extracellular matrix structural constituent conferring tensile strength (GO:0030020)
Extracellular matrix structural constituent conferring compression resistance (GO:0030021)
Extracellular matrix structural constituent (GO:0005201)
Extracellular matrix binding (GO:0050840)
Collagen binding (GO:0005518)
Cell adhesion mediator activity (GO:0098631)
Transmembrane receptor protein tyrosine kinase activity (GO:0004714)
Growth factor binding (GO:0019838)

Table 3.1 Gene ontology enrichment analysis for PC1. Top 10 gene ontology terms identified via enrichment analysis of the genes comprising PC1 in the principle component analysis in Figure 3.5C.

One of our primary hypotheses regarding JHU013-C's aberrant behavior was that off-target mutations had been introduced, either during the CRISPR-editing process or spontaneously in culture afterwards. To interrogate this, we decided to pursue whole exome sequencing (WES). We submitted five iPSC samples to the Johns Hopkins Genetics Research Core Facility for WES: two distinct clones of JHU013, two distinct clones of JHU013-C, and one clone of JHU001. The GRCF performed the DNA extraction, sequencing and initial data processing including genome alignment and variant annotation.

The first question we wanted to answer with the WES data was "Did the CRISPR editing properly correct the *DSG2* mutation in JHU013-C?". A quick look at the gene alignment data revealed that, as expected, JHU013-C iPSCs did not harbor the *DSG2* c.2358delA mutation, while JHU013 iPSCs showed a heterozygous genotype (Fig. 3.6). All identifiable genetic variants were then annotated and analyzed for potentially impactful off-target mutations. We adapted an analysis workflow from two publications aiming to identify off-target mutations in CRISPR-edited cells [101,102] to generate the set of parameters detailed in Table 3.2, which was then applied to all variants identified in the JHU013-C clones. This left 441 potentially impactful variants that were not present in JHU013 iPSCs, confirming our suspicions of significant genomic differences.

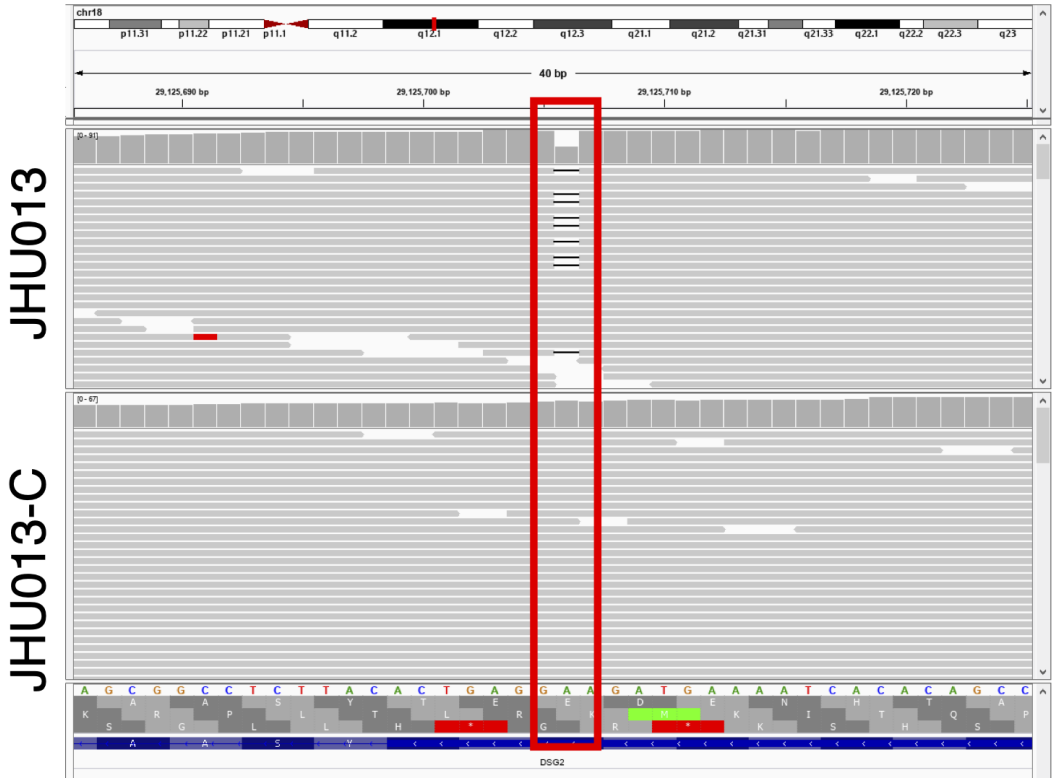

Figure 3.6 Whole exome sequencing shows wildtype *DSG2* alleles in JHU013-C. Image shows sequencing reads for the portion of *DSG2* containing the c.2358delA variant. The missing nucleotide is apparent in about half of the reads for JHU013, suggesting heterozygosity, while there are no missing nucleotides at that location in JHU013-C.

Off-target Mutation Workflow Criteria:
Exclude: variants in intronic regions and synonymous SNVs
Exclude: variants with poor quality sequencing (Total Reads < 10 or Quality/Total Reads < 2)
Exclude: genes with more than 3 different variants observed
Exclude: homozygous variants
Exclude: variants with greater than 1% prevalence in the general population
Exclude: variants present in either unedited JHU013 clone
Include: variants present in both JHU013-C clones

Table 3.2 Criteria for identifying impactful off-target mutations in JHU013-C from WES data.

We then queried our RNA-seq data to assess the relative expression of those 441 genes with new mutations. The heatmap in Figure 3.7 makes it fairly clear that in

this particular set of genes, JHU001 and unedited JHU013 CMs have expression patterns that are much more similar to each other than either are to JHU013-C CMs. This finding supports the hypothesis that the identified gene mutations are actually impactful.

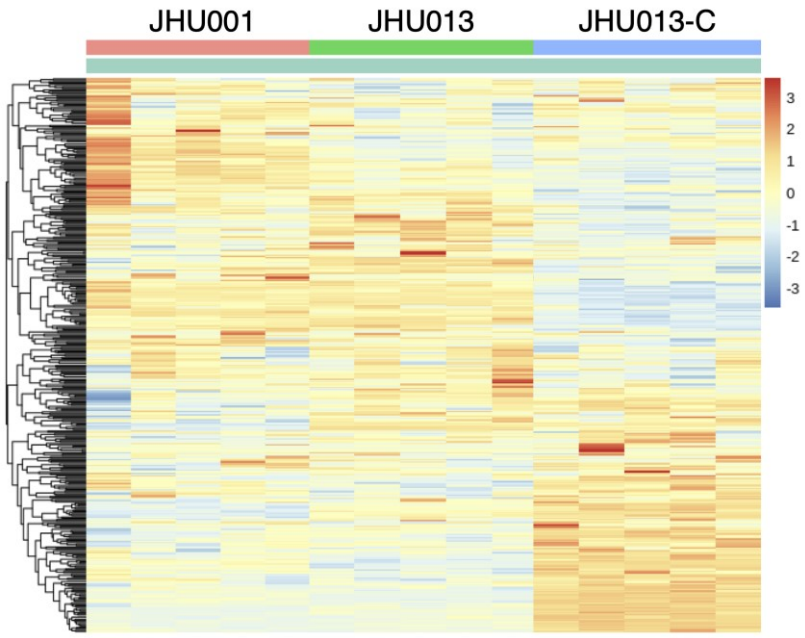

Figure 3.7 RNA-seq data for genes identified as newly mutated in JHU013-C. Heatmap displaying iPSC-CM expression for the 441 genes with new, potentially impactful mutations identified in JHU013-C iPSCs.

3.4 Discussion

In this chapter, we used CRISPR-Cas9 with non-homologous end joining to edit *DSG2* in the JHU013 line and generate an isogenic control line with two normal *DSG2* alleles. Through a multifaceted characterization, we discovered that cardiomyocytes derived from this new line, JHU013-C, did not behave the way we expected a control line to behave. These cells displayed very slow conduction

velocities, altered calcium dynamics and aberrant localization of DSG2. These abnormal results warranted deeper investigation which revealed that JHU013-C cells were very abnormal transcriptionally compared to both control and JHU013 lines. This investigation also led us to identify more then 400 potentially impactful off-target mutations in JHU013-C iPSCs which were not present in the parent line. This preponderance of evidence led us to conclude that JHU013-C is not a truly "corrected" iPSC line and should not be considered an isogenic control because of the extent of the potentially impactful genomic differences between it and its parent disease line.

The presence of so many off-target mutations is surprising but has many potential explanations. It is normal and expected than any cell line in culture will accumulate spontaneous mutations over time, and this is also true of iPSCs [103,104]. One study found that cultured human pluripotent stem cells cultured *in vitro* acquire approximately 3-11 base pair substitutions per population doubling [105], a more than 40 times faster than the *in vivo* mutation rates observed for the same cell types. Assuming that the iPSC population doubles every 18 hours and acquires 10 new mutations at each doubling and given that gene exons account for only 1% of the 3.2 billion base pairs in the human genome, we would expect it to take over eight years of continuous culture to amass 400 exonic mutations. Therefore, if these mutations were caused by random drift, it would be incredibly unlikely that two independently maintained JHU013-C clones would amass 400+

identical, nonsynonymous exonic variants not found in either of two independently maintained JHU013 clones, over the course of a few months.

It is much more likely that these mutations originated in some portion of the gene editing process, where both clones would have been subjected to the same conditions. Great effort and care were invested in designing the gene editing procedure to avoid exactly this problem. Guide RNAs were carefully selected for high efficiency scores and low levels of predicted off-target binding; neon electroporation conditions were optimized to deliver the CRISPR constructs with as little cellular damage as possible; and all standard quality control practices were observed, including assessing genome stability (via karyotyping), verifying pluripotency (via RT-qPCR and immunostaining for pluripotency markers), and confirming the effect on the target gene (via sanger sequencing). Despite these steps, the resulting gene-edited iPSC lines apparently acquired hundreds of off-target mutations.

Without further extensive experimentation, it is very difficult to conclusively ascertain where in the gene editing process this problem originated. However, this work can potentially serve as a case study for the importance of quality control testing in gene-edited iPSCs, even when using methods that are touted to be highly targeted with minimal off-target effects. There are no universally accepted guidelines for what kind of studies are necessary to validate a gene-edited iPSC line, but some investigators in the field have recently begun to argue that the standards for quality control should include searching for off-target effects. In a 2020 review

of iPSC gene editing pipelines, one group recommended that all CRISPR edited iPSC lines undergo a quality control regimen that includes not just tests of genomic stability and pluripotency, but also routine testing for off-target effects [106]. This could include studies as advanced as whole exome sequencing, as we performed as part of this work, or as basic as RT-qPCR or high-resolution melting analysis of the 10 most likely off-target loci according to prediction algorithms. Other groups advocate for slightly more obscure types of measurements, such as evaluating so called “pseudo-genes”, DNA sequences known to share high homology with the target gene which may or may not be transcribed [107].

At the moment, this depth of quality control is rare. Very few papers using gene corrected iPSC lines report any type of testing for off-target effects of the process and the same goes for most industrial contractors providing genome editing services [77,108–111]. There are many reasons that this kind of testing is not more commonly performed. Adopting these standards across the board could substantially increase the cost, time, and effort involved in producing gene-edited iPSC lines. There are also no clear guidelines or cutoffs as to what constitutes an acceptable gene-edited clone. How many off-target-mutations are tolerable? Does it matter which genes are affected? Research into this area and the establishment of best practices, could make such testing much more common and improve the reliability and usefulness of iPSC disease models, even as newer generations of genome editing technology achieve ever-higher fidelity.

3.5 Conclusion

We sought to use CRISPR-Cas9 gene editing to create an isogenic control line for the *DSG2*-mutant JHU013 iPSC. This new cell line displayed very unexpected phenotypic characteristics and generally did not behave as expected for a control line. Through our investigation, we concluded that this is likely due to off-target mutations acquired as part of the gene-editing process. With this insight, we ceased further experiments using the gene edited-cell line. However, data from experiments in which the JHU013-C line was used as the only control, and which we were not able to repeat later with wildtypes, are still reported in the following chapters.

While unfortunate considering the significant amount of data we had collected with JHU013-C iPSC-CMs as the control line, we hope that this work can serve as a case study on the importance of thorough validation of new cell lines, particularly after genome editing.

Chapter 4 – Beta-adrenergic signaling in ARVC iPSC-CMs

4.1 Background

A pathologic response to exercise has emerged as a very consistent feature of ARVC. Exercise has been shown to drastically exacerbate the progression of ARVC and increase the risk of sudden cardiac death in both mice and human patients [10,38,40,41]; exercise restriction is therefore a key tenet of clinical ARVC management [6,41,112]. While there is strong consensus that ARVC patients should be advised to avoid strenuous exercise, there is still no strong mechanistic understanding of how exercise contributes to an acutely increased risk of ventricular arrhythmia or to longer-term disease progression. One noteworthy feature of exercise is that it engenders a sharp stimulation of β-adrenergic signaling,

which has itself been shown to affect ARVC patients detrimentally. Isoproterenol and other β-adrenergic agonists cause premature ventricular complexes and induce ventricular arrhythmia in ARVC patients with such regularity that isoproterenol testing has been proposed as a diagnostic tool for ARVC [42,43]. Chronic stimulation of β-adrenergic activity has also been proven to promote cardiac inflammation and accelerate myocardial remodeling in mouse models of ARVC [38].

Pathology studies of human tissue found that post-synaptic β-adrenergic receptor density is reduced by about 40% in the intrinsic cardiac nervous system of ARVC patients, compared to healthy controls [113], providing further evidence for a link between ARVC and adrenergic signaling. That type of downregulation of receptor density is often part of a feedback mechanism responding to direct overstimulation or high levels of downstream signaling [114,115]. At a cellular level, β-adrenergic signaling has been shown to increase desmoglein-2 trafficking to the cellular membrane in wildtype mouse cardiomyocytes [44].

In this chapter, our work focuses on assessing the effects of isoproterenol on development of pathogenic changes in *DSG2*-mutant iPSC-CMs, with the hypothesis that *DSG2*-mutant cells will be more sensitive to isoproterenol and will respond with greater changes in action potential duration and conduction. We also test whether desmosomal protein localization changes in response to isoproterenol in our iPSC-CMs, as has been previously demonstrated in mouse cardiomyocytes.

4.2 Methods

4.2.1 Optical mapping

For the most part, optical mapping studies were performed as described in section 2.2.5. For the voltage mapping data presented in this chapter, there is a mix of data using Di-4-ANEPPS (as was used in Chapter 2 experiments) and Di-8-ANEPPS which is a more recently developed voltage indicator that is reported to be longer lasting and less cytotoxic and shows slower loading of intracellular compartments over time. Recordings with these two dyes are broadly similar, though on average Di-8 recordings show a slightly longer action potential duration than Di-4, but this effect seems to consistently scale. Because we are interested in the change in action potential in response to a stimulant as opposed to the absolute values, we pooled this data for increased power and confirmed that each trend holds across the data from both dyes. We do not expect this change to affect our conclusions.

For acute isoproterenol experiments, we stained and washed the monolayer to prepare for optical mapping, allowed it to acclimate on the heated stage, and then took a set of recordings at predetermined pacing intervals to serve as our baseline measurements. Next, while continuing to stimulate the sample at 1 Hz, we added 1 mM isoproterenol 1:1000 for a final concentration of 1 μM. After 5 minutes of treatment, we took another set of recordings.

4.2.2 Beat rate analysis

Beat rate analysis was primarily performed as described in Section 3.2.2, except that two sets of recordings were taken for each sample. After a plate containing iPSC-CM monolayer was allowed to equilibrate in the incubator, three separate 30 second recordings were taken of each well. Either 1 μM or 10 μM ISO was then added to each well, and after 5minutes, another set of three recordings were taken.

4.2.3 Biomolecular assays

Immunocytochemistry was performed as described in section 2.2.3.

4.2.4 Statistics

Unless otherwise indicated, all data are presented as mean ± 95% confidence interval, calculated in R. Continuous variables were compared using unpaired, unequal variance Student's t-test with a Holm-Bonferroni family-wise error correction. $P < 0.05$ in two-tailed analysis was considered significant.

4.3 Results

4.3.1 Electrophysiological response to isoproterenol is altered in JHU013 iPSC-CMs

We first sought to evaluate the acute effects of isoproterenol on *DSG2*-mutant as well as control iPSCs. We prepared iPSC-CM monolayers as described previously herein (Section 2.2.2). For mapping experiments, we took an initial set of

recordings to measure the monolayers' behavior at baseline. We then added 1 μM ISO to the mapping solution, waited 5 minutes while continuing to electrically stimulate the monolayers at 1 Hz, and then took another set of recordings. 1 μM was chosen after pilot studies showed no significant difference in response between 1 and 10 μM treatment.

We found that 5-minute treatment with 1 μM ISO resulted in significantly increased conduction velocity in wildtype JHU001 iPSC-CMs (ΔCV=1.44$\pm$0.53 cm/s; Fig. 4.1A,B). ISO also increased CV in JHU013 CMs, on average, but the difference was not statistically significant (ΔCV = 1.44$\pm$1.83 cm/s). In JHU001 monolayers, acute ISO treatment resulted in shortened action potentials (ΔAPD_{30} = -20.7$\pm$6.7 ms, ΔAPD_{80} = -22.6$\pm$11.6 ms; 1000 ms paced cycle length; Fig. 4.1D,E), but very interestingly, these significant shortening effects were not observed in JHU013 samples (ΔAPD_{30} = -7.5$\pm$10.0 ms, ΔAPD_{80} = -4.1$\pm$14.7 ms; 1000 ms paced cycle length). However, ISO did not appear to have a very substantial effect on the action potential upstroke, as maximum upstroke velocity was similar before and after ISO treatment in both lines (Fig. 4.1F). We also found that ISO did not induce a significant change in spatial heterogeneity of conduction or upstroke velocity in JHU001 samples (Fig. 4.1C,G), while there was a small but statistically significant increase in conduction heterogeneity in JHU013 samples (%ΔRSD = 7.6$\pm$6.9%; 1000 ms paced cycle length).

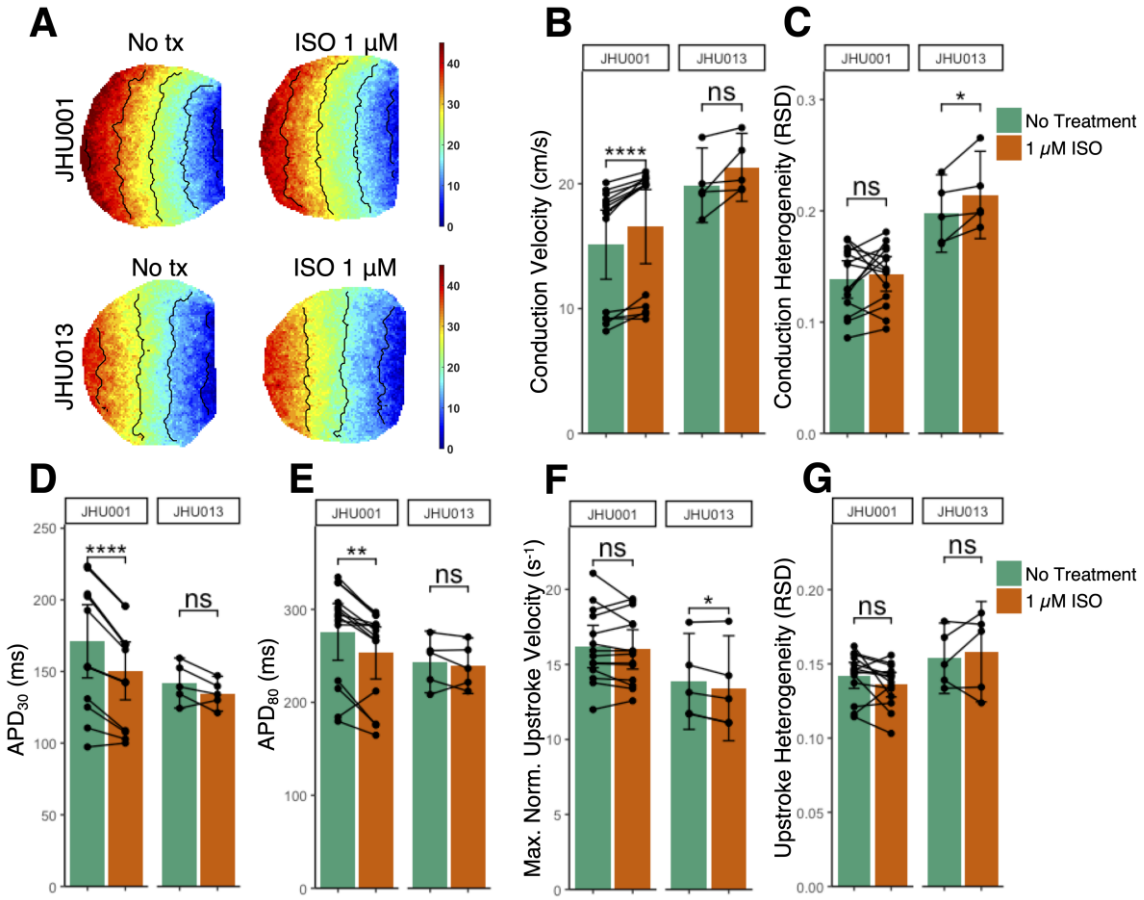

Figure 4.1 Action potential and conduction effects of acute isoproterenol treatment. (A) Representative isochrones depicting conduction in JHU001 and JHU013 iPSC-CM monolayers before and after treatment with 1 μM ISO. Isochrones lines are spaced 10 ms apart. (B-C) Conduction velocity and conduction heterogeneity response to ISO. (D) APD_{30}, (E) APD_{80}, (F) peak upstroke velocity, and (G) upstroke heterogeneity response to ISO. For (B-G), each point represents a single measurement and black lines connect measurements from the same sample before and after 5-minute treatment with 1 μM ISO. All data recorded at 1000 ms paced cycle length.

How action potential duration changes in response to changes in pacing rate is key factor in arrhythmogenesis. Our voltage mapping data revealed that as the pacing rate increased from 1 to 2 Hz, the magnitude of APD shortening caused by isoproterenol in wildtype cells decreased slightly, as would be expected. But as the

pacing rate increased in JHU013 iPSC-CMs, ISO had either no effect at all on APD or, in some cases, even had a net lengthening effect on APD (Fig. 4.2).

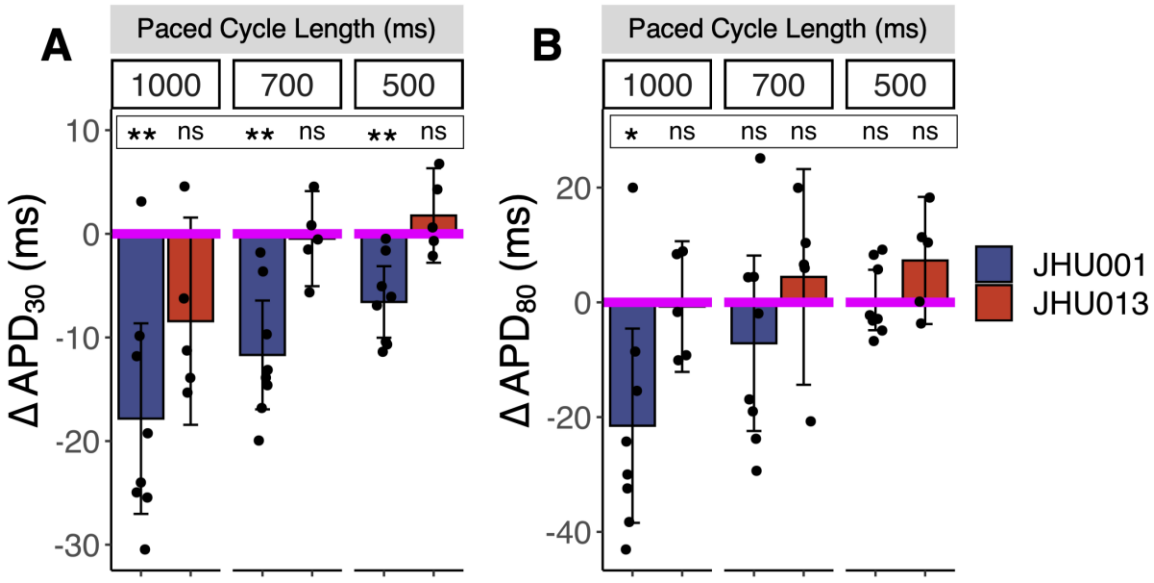

Figure 4.2 Impact of isoproterenol on restitution of action potential duration. Change in APD_{30} (A) and APD_{80} (B) in response to ISO across multiple pacing rates. Each point represents the difference between pre- and post-ISO APD measurements in a single sample. Significance calculated as a one-sample t-test with null hypothesis of no change.

Calcium mapping experiments revealed no observable change to calcium transient duration (CTD_{80} and CTD_{30}) in either cell line in response to acute ISO treatment. However, we did find a small reduction in the speed of Ca^{2+} decay in JHU001 monolayers ($\%\Delta\lambda$ = -6.1±1.4%; Fig. 4.3C) that was not observed in JHU013 ($\%\Delta\lambda$ = -0.7±4.6%). On the other hand, time-to-peak Ca^{2+} (TTP-Ca^{2+}) in JHU001 was not affected by ISO (ΔTTP-Ca^{2+}= -3.8±12.4 ms; Fig. 4.3D), while it was increased in JHU013 (16.0±14.7 ms).

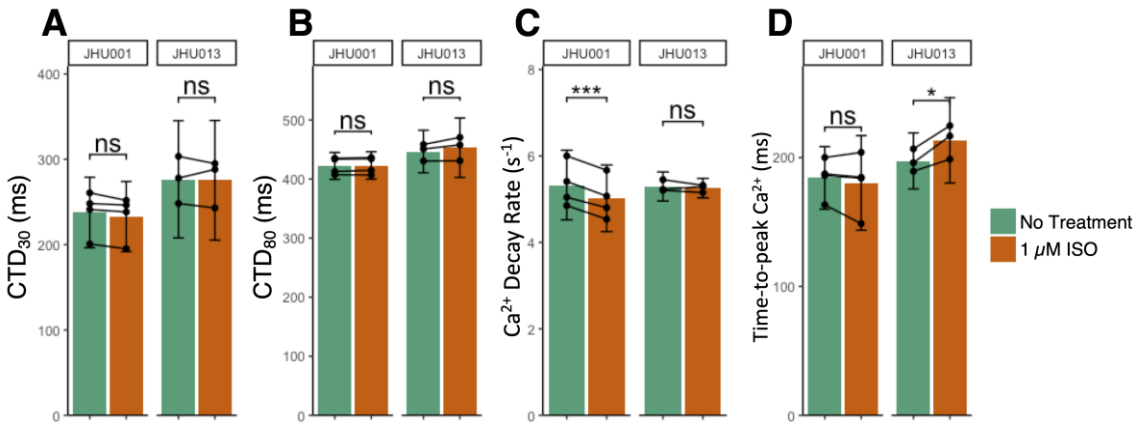

Figure 4.3 Calcium transient effects of acute isoproterenol treatment. (A) Calcium transient duration at 30% decay (CTD_{30}), (B) CTD_{80}, (C) Ca^{2+} decay rate, and (D) Ca^{2+} time-to-peak response to ISO. Each point represents a single measurement and black lines connect measurements from the same sample before and after 5-minute treatment with 1 μM ISO. All data recorded at 1000 ms paced cycle length.

In addition to its effects on calcium dynamics, isoproterenol is known to have substantial positive chronotropic actions [116,117]; in iPSC-CM preparations, this is the most immediate and consistently observed effect of isoproterenol. In order to assess any potentially differential effects on *DSG2*-mutant iPSC-CMs, we measured the spontaneous beating rates of CM monolayers before and after ISO treatment.[*] Our analysis showed that spontaneous beating rate increased significantly in both JHU013 and JHU013-C CMs in response to both doses of ISO. However, we found that at each dose, the relative increase in beating rate was significantly larger in JHU013-C than in JHU013 (Fig. 4.4A). While the JHU013-C CMs saw an average

[*] For these experiments, we have only data for the *DSG2*-mutant line, JHU013, and the CRISPR-edited derivative line, JHU013-C. Ideally we would also have measurements for one of the wildtype lines, but since we found in other experiments that the JHU013-C CM electrophysiology behaved similarly to wildtype in response to ISO, we feel that this data is valuable to present.

increase of 70% in its beating rate in response to 1 μM ISO, JHU013 CMs saw only a 40% change. We also measured beat-to-beat variability by measuring. the variability of cycle lengths within each video recording. Of the four tested groups, the only group with a significant change in this parameter was the JHU013-C CMs treated with 1 μM ISO, which saw a 30% decrease in variability on average (Fig. 4.4B).

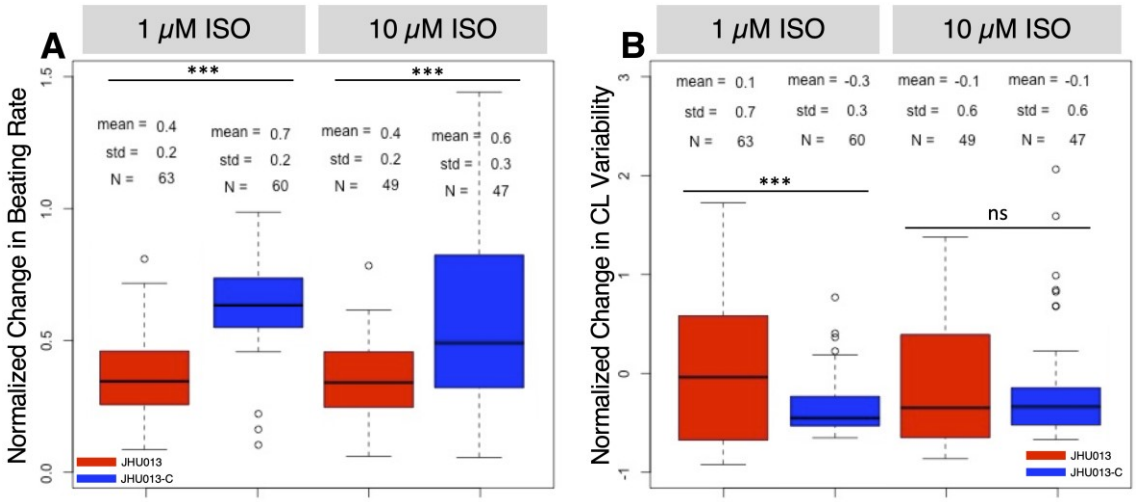

Figure 4.4 Spontaneous beating response to isoproterenol. (A) Normalized change in spontaneous beating rate in response to treatment with 1 or 10 μM ISO in JHU013 and JHU013-C iPSC-CMs. (B) Change in the variability of spontaneous beating in response to ISO treatment. Variability measured as the standard deviation of the cycle length times between each beat within each 30 second recording.[*]

4.3.2 DSG2 knockdown does not recapitulate ISO insensitivity

Having observed these differences in the ways that JHU013 iPSC-CMs respond to isoproterenol, we wanted to investigate whether a transient overall decrease in

[*] This data was analyzed by Adriana Blazeski and was collected with her assistance

DSG2 expression is sufficient to explain these differences, or if a more complex mechanistic explanation is needed. To probe this question, we performed similar optical mapping experiments, this time with siRNA-mediated *DSG2* silencing as an added factor. We transfected JHU001 and JHU013 monolayers with a cocktail of anti-*DSG2* siRNA (DSG2-KD) or a negative control vector (Neg. Control/NC), and performed optical mapping 72 hours later, with and without ISO treatment.

Via optical voltage mapping, we discovered that JHU001 iPSC-CMs displayed shortened action potentials (both APD_{30} and APD_{80}) in response to ISO regardless of whether *DSG2* was knocked down (Fig. 4.5A-C). On average, APD_{30} was reduced by 20.7±6.7 ms in negative control JHU001 CMs and by 12±3.8 ms in DSG2-KD JHU001 CMs, at 1000 ms pacing CL. On the other hand, both negative control and DSG2-KD JHU013 CMs did not have significant changes in APD in response to ISO; ΔAPD_{30} = -7.5±10.0 ms in NC JHU013 and +4.9±19.5 ms in DSG2-KD JHU013. APD_{80} measurements followed a similar pattern: ΔAPD_{80} = -22.7±11.6 ms in NC and -13.3±8.0 ms in DSG2-KD JHU001 CMs and -4.1±14.7 ms in NC and +14.6±34.2 ms in DSG2-KD JHU013 CMs.

Some other electrophysiological parameters were more mixed in their results. Conduction velocity increased in response to ISO in both negative control and DSG2-KD JHU001 monolayers (%ΔCV = +8.7±3.4% in NC +7.6±3.1% in DSG2-KD JHU001 monolayers; Fig. 4.5D), but a statistically significant increase was only apparent in JHU013 samples where *DSG2* had been silenced (%ΔCV = +6.7±8.5% in NC and +9.1±7.6% in DSG2-KD JHU013 monolayers).

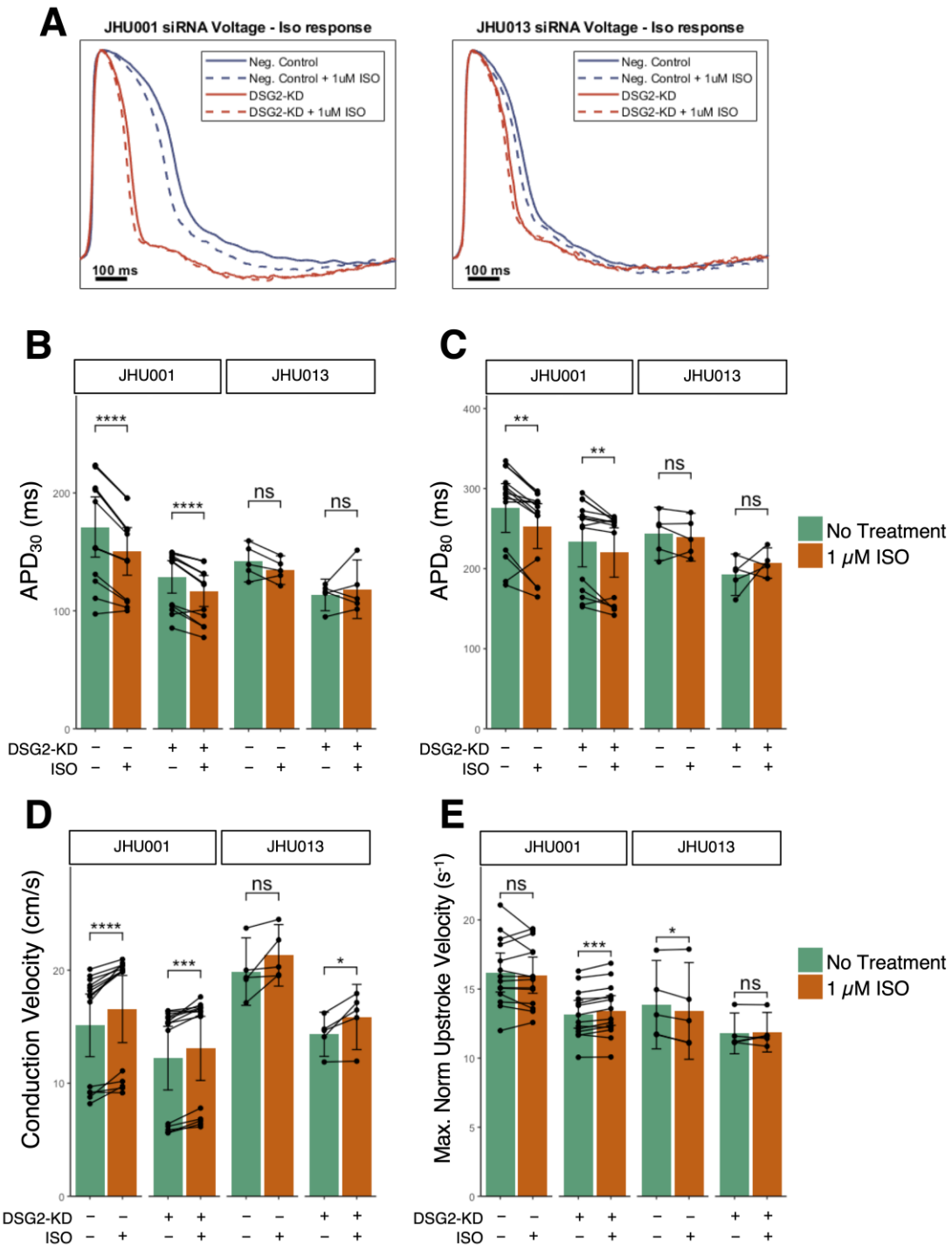

Figure 4.5 Effect of *DSG2* knockdown on the action potential and conduction response to acute isoproterenol treatment. Representative voltage traces (B) APD_{30}, (C) APD_{80}, (D) conduction velocity, and (E) peak upstroke velocity for iPSC-CM monolayers with and without *DSG2* knockdown. For all charts, each point represents a single measurement and black lines connect measurements from the same sample before and after 5-minute treatment with 1 μM ISO. All data collected at 1000 ms paced cycle length.

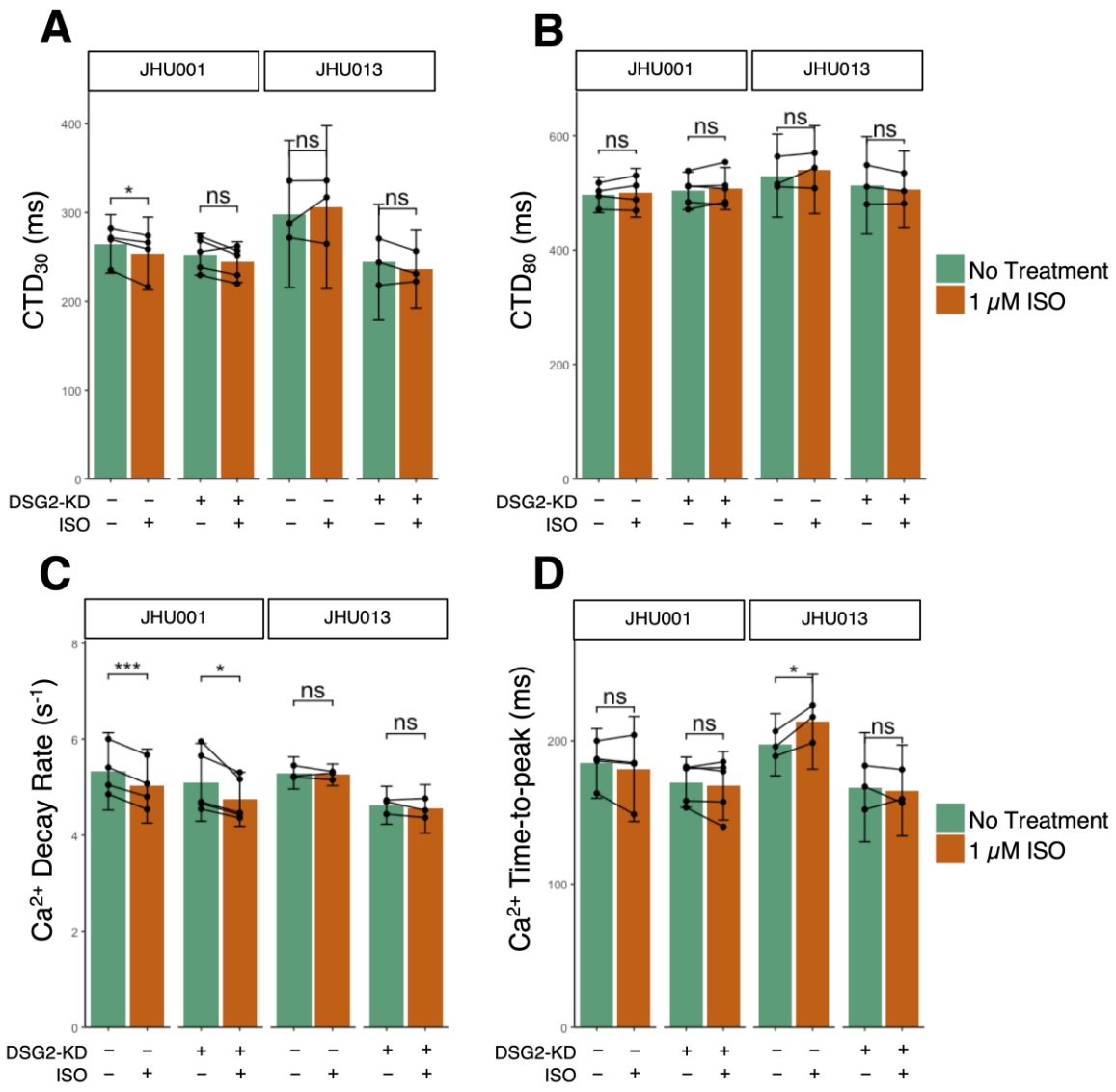

Figure 4.6 Effect of *DSG2* silencing on the calcium transient response to acute isoproterenol treatment. Calcium transient duration at 30% decay and (B) 80% decay, (C) Ca^{2+} decay rate, and (D) Ca^{2+} time-to-peak for iPSC-CM monolayers with and without *DSG2* knockdown. Each point represents a single measurement and black lines connect measurements from the same sample before and after 5-minute treatment with 1 μM ISO. All data collected at 1000 ms paced cycle length.

It may be worth noting that on average CV did increase in NC JHU013 CMs, but that difference was not statistically significant. ISO treatment demonstrated very little effect on maximum upstroke velocity in any of the tested groups (Fig. 4.5E). While we did find a significant increase in DSG2-KD JHU001 samples ($\%\Delta V_{upstroke} = +1.9\pm1.0\%$) and a decrease in NC JHU013 samples ($\%\Delta V_{upstroke} = -3.8\pm3.1\%$), even these differences were fairly small in magnitude.

The calcium transient response to ISO also did not seem to be strongly modulated by *DSG2* knockdown. Calcium transient durations did not change in response to ISO in all tested groups except for a small increase decrease in CTD_{30} in NC JHU001 ($\Delta CTD_{30} = +4.7\pm4.9$ ms; Fig. 4.6A,B). In JHU001 iPSC-CMs Ca^{2+} decay rate was reduced both with and without *DSG2* suppression ($\%\Delta\lambda = -6.1\pm1.4\%$ in NC JHU001 and $-7.2\pm5.6\%$ in DSG2-KD JHU001), while JHU013 CMs showed no ISO response in either treatment group ($\%\Delta\lambda = -0.7\pm4.8\%$ in NC JHU013 and $-1.6\pm5.9\%$ in DSG2-KD JHU013; Fig. 4.6C). Ca^{2+} time-to-peak was generally unaffected by ISO; the only significant response we observed was a lengthened TTP-Ca^{2+} in NC JHU013 samples (Fig. 4.6D).

4.3.3 Isoproterenol elicits no observed effect on expression of desmosome proteins

We found very interesting differences in the acute effects of isoproterenol on *DSG2*-mutant vs. control iPSC-CMs, but studies have shown that longer treatments with isoproterenol can increase the mobility of DSG2 proteins and its expression at

the cellular membrane in murine cardiomyocytes [44]. We sought to replicate this finding in our iPSC-CMs and to determine whether the ISO response, like the electrophysiology, was different in JHU013 cells. For these experiments, we treated differentiation day 35 iPSC-CM monolayers with 1 μM isoproterenol or an equivalent volume of water (the solvent) and incubated them for 24 hours. At that time, the cells were fixed, and immunostaining was performed to visualize desmosomal components desmoglein-2 and plakoglobin as well as the more ubiquitous adhesion protein N-cadherin, which is additionally useful as a marker of intercellular boundaries, where we expect to see the desmosomal protein expression. As was the case with the beating rate data in Section 4.3.1, these experiments were conducted with only the JHU013-C line as a control.

Confocal imaging of these samples revealed no obvious change in the localization of desmoglein-2 in response to ISO in either line (Fig 4.7). In JHU013-C CMs, plakoglobin staining at the cell membrane was poor both with and without isoproterenol treatment but in JHU013 CMs, there was some evidence that plakoglobin localization shifted slightly away from the cell boundaries and instead accumulated near the nucleus. However, this latter observation was not true across all samples. Finally, the intensity of N-cadherin immunostaining was highly variable between samples, but it did not appear to be consistently affected by ISO treatment in either line. However, it did have one notable feature which was that the N-cadherin-positive region at the cell boundary was much wider in JHU013-C iPSC-CMs and suggested a more jagged, irregular intercellular boundary. This was

one of many findings that prompted the deep investigation of JHU013-C phenotype and genotype detailed in Chapter 3.

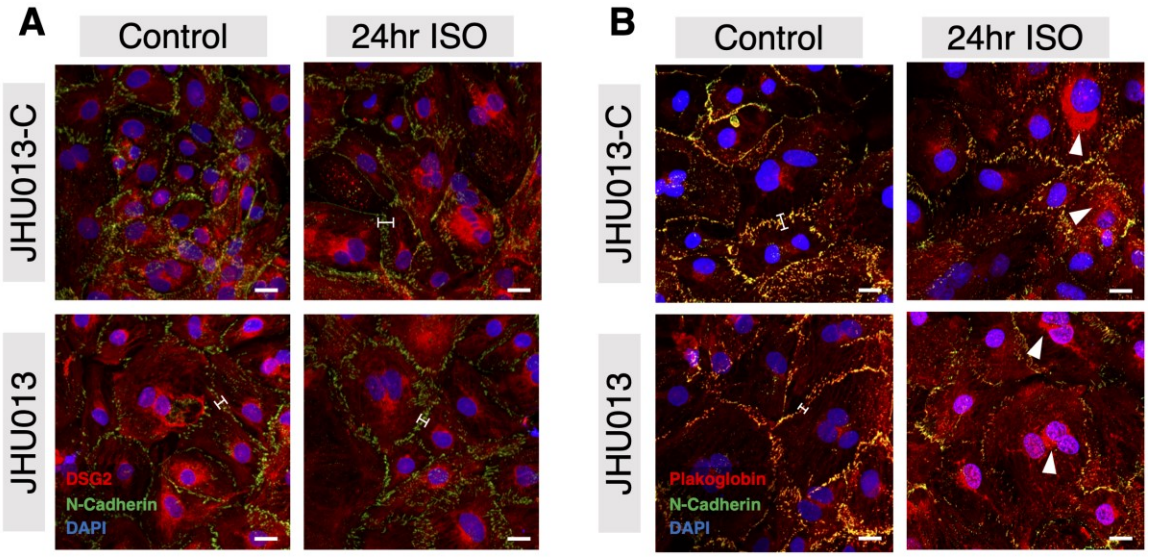

Figure 4.7 24-hour isoproterenol effect on desmosomal protein expression. (A) Confocal images of JHU001 and JHU013-C iPSC-CM monolayers stained for DSG2 and N-cadherin. (B) Confocal images of JHU001 and JHU013-C iPSC-CM monolayers stained for plakoglobin and N-cadherin. White scale bars, 10 µm. White length markers indicate N-Cadherin-positive intercellular boundaries. White arrow heads highlight perinuclear accumulation of plakoglobin.

4.4 Discussion

We found that acute exposure to isoproterenol produced a significant increase in conduction velocity and decrease in action potential duration in wildtype JHU001 iPSC-CM monolayers but that these effects were either not present or blunted enough as to be statistically insignificant in JHU013 CMs. ISO treatment slowed the Ca^{2+} decay kinetics in JHU001 while not affecting JHU013 but lengthened the Ca^{2+} time-to-peak in JHU013 without any significant changes in JHU001; the net effect was no significant change in total calcium transient

duration. ISO exposure also accelerated the spontaneous beating rate for CMs from both cell lines but the increase in JHU001 was significantly larger. siRNA-mediated suppression of *DSG2* expression in wildtype cells did not recapitulate the major differences in ISO response we observed in JHU013 CMs and 24 hours of ISO treatment did not have a discernable effect on the expression or trafficking of major desmosomal proteins.

Based on the extreme sensitivity to isoproterenol demonstrated in ARVC patients [43], we hypothesized that JHU013 iPSC-CMs would be more sensitive to the effects of isoproterenol but instead found the exact opposite: the most prominent electrophysiological effects of ISO in JHU001 cells were blunted or absent in JHU013. The mechanisms underlying this difference in response remain very unclear, but the fact that *DSG2* knockdown does not reproduce these effects in JHU001 CMs suggests that specific characteristics of the *DSG2* mutation itself, and not merely its resultant decrease in *DSG2* expression, play an important role. Although, because of the transient nature of siRNA-mediated gene knockdown, these experiments cannot account for the effects of longer-term *DSG2* expression changes and associated compensation.

While it is not obvious why *DSG2*-mutant iPSC-CMs response so differently to ISO, there is a way in which their response could contribute acutely to arrhythmia. As heart rate increases, action potential duration of cardiomyocytes naturally becomes shorter, a phenomenon known as restitution of the action potential duration. When that restitution is compromised it can amplify any heterogeneities

in the myocardium and create areas of local conduction block, where action potential propagation reaches still depolarized and unresponsive tissue, which could trigger reentry [118–120]. In our experiments, we found some evidence that restitution of APD is impaired by isoproterenol in JHU013 iPSC-CMs (Fig 4.2) and that conduction heterogeneity within each JHU013 monolayer was enhanced by ISO treatment; in combination, these responses could theoretically contribute to ventricular arrhythmia.

One of isoproterenol's most well-characterized features is its effect on calcium dynamics and excitation-contraction coupling. In a wide variety of models, ISO has been shown to increase the speed of sarcoplasmic calcium release and increase the maximum contractile force in cardiomyocytes. However, these effects have often been reported as lacking in iPSC-CMs [121–124]. The insensitivity of iPSC-CMs to ISO has largely been attributed to low levels of Ca^{2+}-buffering by the sarcoplasmic reticulum associated with lack of t-tubules and organized Ca^{2+} release units due to poor maturity in these cells. Although monolayer-based differentiation protocols may partially ameliorate the issue by improving SR loading and leak dynamics [126], this phenomenon could potentially explain the minimal effects we see on calcium dynamics in our system.

Schinner et al. reported that β-adrenergic stimulation increases DSG2 trafficking to the cellular membrane in mouse cardiomyocytes via enhanced cyclic AMP signaling [44]. However, in our experiments, which were performed at similar drug concentrations and treatment durations, we did not find any distinct effects of ISO

on the localization of DSG2 or plakoglobin. There are many plausible explanations for this discrepancy, including species-specific behavior and differences in CM maturity. One explanation that would fit neatly with the findings of the Schinner paper is that both of the cell lines that we used – JHU013 and JHU013-C – are abnormal in their baseline expression of desmosomal proteins because these experiments were performed without the foresight to include a wildtype control line. The Schinner report found that the ISO effect on DSG2 was dependent on intact plakoglobin expression and specific phosphorylation patterns. It is very possible that the plakoglobin-desmoglein-2 interactions underlying the ISO effect are disrupted in both of the cell lines we used. To make a stronger conclusion, this experiment should be repeated with proper control lines.

One subject that warrants more focused experimentation pertains to the importance of treatment duration on the response to ISO. The documented effects of β-adrenergic stimulation span a range of time courses. A study evaluating the clinical usefulness of isoproterenol testing for ARVC, found that 89% of ARVC patients developed signs of ventricular arrhythmia in under 15 minutes (they performed a 3-minute infusion plus 10 minutes of observation) [43]. On the other end, another study recently found that seven days of continuous isoproterenol exposure induced apoptosis in cardiomyocytes derived from *Dsg2*$^{Mut/Mut}$ mice [38]. Across this range of time scales encompassing three orders of magnitude, it's possible (and I would hazard, likely) that there are multiple mechanisms involved,

which could be distinct or interrelated. A careful study evaluating cellular responses over a range of time points would be valuable in untangling those mechanisms.

There are a several other ways in which these experiments could be improved and expanded upon. Patch clamp measurements could be used to identify precisely which currents are affected by isoproterenol differently between wildtype and *DSG2*-mutant CMs, under acute treatment conditions or over longer periods. And evaluating transcriptional changes in response to isoproterenol, via RT-qPCR panels, RNA-seq, or another method, could shed critical light on the pathways that are involved in medium and long-term responses to ISO.

4.5 Conclusion

In this chapter, we demonstrated that JHU001 iPSC-CMs respond to isoproterenol treatment with action potential shortening, conduction velocity enhancement, and acceleration of spontaneous beating rate, while the response in JHU013 CMs is absent or blunted in all of those parameters. We also found that JHU013 and JHU013-C iPSC-CMs exposed to ISO for 24 hours do not undergo substantial changes to localization of desmoglein-2 and plakoglobin.

Our findings contradicted our expectations that JHU013 CMs would be more sensitive to the effects of isoproterenol but offer a plausible – though far from conclusive – explanation as to how their altered response could lead to arrhythmia in ARVC patients. Further confirmation of our findings and a deeper understanding of the underlying mechanisms have the potential to unlock interventions that

prevent the exacerbation of ARVC associated with exercise and β-adrenergic stimulation.

Chapter 5 – The inflammatory landscape in ARVC iPSC-CMs

5.1 Background

Inflammatory processes play a prominent role in a wide range of cardiomyopathies, including ARVC and other forms of ACM. Inflammatory involvement is such a prominent feature of ARVC, that a large portion of ARVC cases in women are initially diagnosed as myocarditis [35]. In the vast majority of ARVC patients who experience sudden cardiac death, myocardial infiltration of inflammatory immune cells is apparent in histological samples, and inflammatory cytokines have been shown to be elevated in the plasma of ARVC patients [3,125]. However, professional immune cells comprise only part of the inflammatory

environment, as cardiomyocytes themselves have been shown to produce these cytokines in disease states [25].

In this chapter, we aim to evaluate the inflammatory state of JHU013 iPSC-CMs and assess whether NFκB and other inflammatory signaling pathways are substantially altered in these cells. We primarily rely on cytokine expression arrays and RNA-sequencing. By characterizing the inflammatory landscape of JHU013 iPSC-CMs, we can offer insight into how cardiomyocytes, and not just immune cells, in ARVC might contribute to disease progression and structural degradation of myocardium.

5.2 Methods

5.2.1 iPSC-CM culture and differentiation

iPSC-CM culture and differentiation were performed as described in Section 2.2.2.

5.2.2 Cytokine arrays

For cytokine analysis, iPSC-CM samples were re-plated on differentiation day 28 into 24-well plates at a density of 250,000 cells/cm^2 and cultured for another week to allow the formation of a monolayer. On day 37 iPSC-CMs were isolated and lysed in RIPA buffer. For these experiments, four wells of a 24-well plate were combined for each sample, yielding approximately 2x10^6 cells. Cell lysates and cell culture supernatants were analyzed using the Proteome Profiler Human XL

Cytokine Array Kit (R&D Systems, Minneapolis, MN, USA), following the manufacturer's instructions with one exception: instead of using the chemiluminescence reagent that was included, we instead used the SuperSignal West Femto Maximum Sensitivity Substrate (Thermo Fisher). Films were obtained and developed in a dark room, scanned, and then analyzed using Quick Spots image analysis software (Western Vision Software, Salt Lake City, UT, USA).

5.2.3 RNA-sequencing

RNA-sequencing and analysis was performed as described in Section 2.2.4.

5.2.4 Oil Red O staining

For Oil Red O lipid staining, cell monolayers were washed three times with cold PBS, fixed in 4% paraformaldehyde for 10 minutes, and then washed again. Samples were then incubated in 60% isopropanol for 5 minutes before being stained with Oil Red O working solution (MilliporeSigma, St. Louis, MO, USA) for 15 minutes. Cells were then washed in PBS three times, and 10x brightfield images were taken on an EVOS inverted microscope (Thermo Fisher).

5.2.5 Statistics

All data in this chapter is presented as mean ± standard deviation, calculated in R. Continuous variables were compared using unpaired, unequal variance Student's t-test with a Holm-Bonferroni family-wise error correction. $p < 0.05$ in

two-tailed analysis was considered significant. For RNA-seq data presented in volcano plots, a cutoff value of $p<0.001$ was used.

5.3 Results

5.3.1 Cytokine expression is altered in JHU013 iPSC-CMs

To assess the immunologic state of our iPSC-CMs, we used printed antibody arrays to assess iPSC-CM lysates for the production of 105 cytokines in JHU013 and JHU001 cell lines. We found 71 total cytokines to be differentially expressed in the cellular lysates of JHU013 CMs compared to JHU001(Fig. 5.1A,B).[*] Of these, several stood out as particularly interesting. Beginning with the innate immune response, we identified eight cytokines involved in that process which were differentially regulated in JHU013 CMs (Fig. 5.1C). Among these was the receptor for advanced glycation end products (RAGE), which binds to nuclear high-mobility group box-1 (HMGB1) to promote cell death [126]; recent work by Chelko et al. demonstrated that HMGB1-nuclear loss leads to myocyte cell necroptosis in *Dsg2*-mutant mice [38]. We also identified several pleiotropic cytokines and chemokines involved in mobilizing and recruiting immune cells, which were upregulated in JHU013 (Fig. 5.1D). One of these, monocyte chemoattract protein-1 (MCP-1), was previously reported to be upregulated in the myocardium of *Dsg2*-mutant mice as well as in supernatants and cell lysates from *PKP2*-mutant iPSC-CMs [39].

[*] Collection and analysis of this data was done in coordination with Dr. Stephen Chelko.

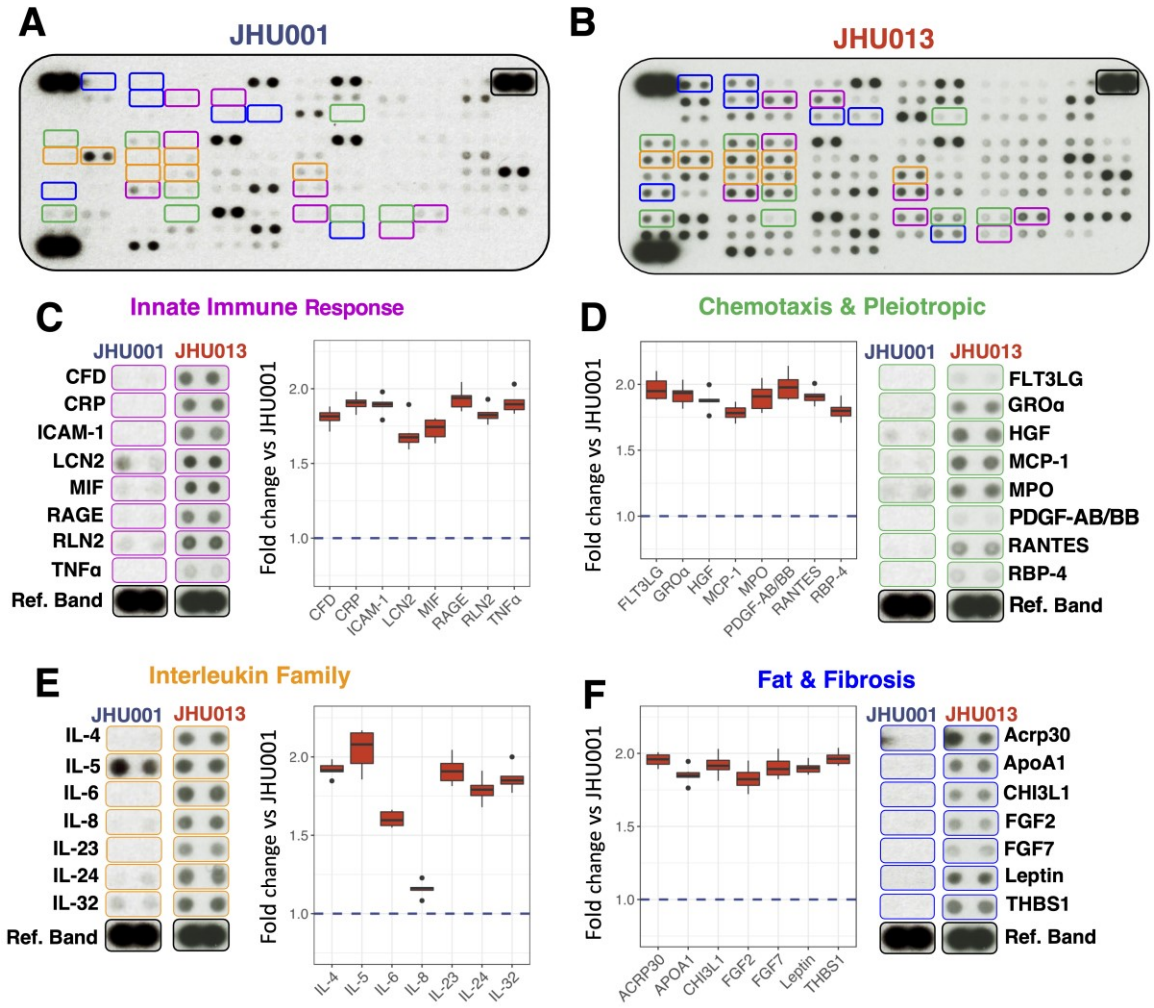

Figure 5.1 Cytokine expression in JHU013 iPSC-CMs. (A,B) Representative cytokine immunoblots from wildtype control (JHU001) and *DSG2*-mutant (JHU013) iPSC-CMs. Colored boxes highlight specific cytokines, grouped based on their role in inflammation: the innate immune response (purple); chemoattractant and pleiotropic regulation (green); interleukins that regulate immune cell differentiation and proliferation (orange); and adipo-fibrokines involved in lipid accumulation and metabolism and fibrotic remodeling (blue). (C-F) Box and whisker plots of selected groups of cytokines along with inset images from Figure 5A,B. Data presented as mean ± standard deviation. Blue dashed line represents normalized values for JHU001; JHU001 (n=4); JHU013 (n=6); For all values shown in (C-F) $p < 0.05$ comparing JHU001 and JHU013.

Multiple members of the potent, proinflammatory interleukin (IL)-family were expressed differently in JHU013 CMs compared to JHU001 (Fig. 5.1E). Cytokines that regulate immune cell differentiation (e.g., IL-5, IL-6, and IL-32) and

proliferation (e.g., IL-4, IL-23, IL-24) were elevated in JHU013 CMs, suggesting substantial differences in inflammatory signaling. Lastly, several adipo-fibrokines which drive lipid accumulation, regulate adipocyte survival and proliferation, and promote fibrotic remodeling were significantly elevated in JHU013 iPSC-CMs compared to controls, including apolipoprotein A1 (APOA1), leptin, and fibroblast growth factors 2 and 7 (FGF2 and FGF7) (Fig. 5.1F).

5.3.2 NFκB signaling is enhanced in JHU013 iPSC-CMs

A report published by Chelko et al. in 2019 demonstrated that myocardial inflammation in *Dsg2*-mutant mice as well as cytokine production in PKP2-mutant iPSC-CMs are regulated via the canonical NFκB pathway [39]. We queried our bulk RNA-seq data set, which includes data for JHU001 and JHU013 iPSC-CMs, for markers related to NFκB signaling, based on the gene ontology term "NIK/NF-kappaB signaling" (Fig. 5.2A). We then applied a KEGG PATHWAY analysis to map out the expression of the components of the NFκB pathway (Fig. 5.2B).

Our results highlight four cell surface receptors involved in regulating canonical and non-canonical NFκB signaling which were upregulated in JHU013 CMs: IL-1R, XEDAR, Toll-like receptor-4 (TLR4), and CD40 (Fig. 5A,B). TLR4 is a pleiotropic NFκB transcription factor which regulates IL-23-induced T-cell infiltration [127], a cytokine we found to be upregulated in JHU013 iPSC-CMs (Fig. 5.1E). Downstream of TLR4- and IL-1R-induced NFκB activation, we found IL-1R kinase-1 (IRAK1) and TRIF to also be more highly expressed in JHU013 CMs (Fig. 5.2). These two

pathways merge to signal through TGF-β activating kinase (TAK1/MAP3K7) and TAK binding protein (TAB) to initiate canonical NFκB signaling via activation of p50/p65 (RELA) (Fig. 5.2B). While we did not find that RELA itself was differentially expressed in our RNA-seq analysis, downstream RELA-mediated factors were upregulated in JHU013 iPSC-CMs, including IL-8 and COX4. This discrepancy is potentially explained by post-transcriptional mechanisms of regulation.

We next turned to the cell surface receptors involved in regulating non-canonical NFκB signaling, CD40 and XEDAR. Non-canonical NFκB signaling is mediated through tumor necrosis factor receptor-associated factors (TRAF1-6), where prior work demonstrated TRAF2 acts as a negative regulator of NFκB [128–130]. Our data showing reduced levels of TRAF2 and upregulation of RELB, a positive regulator of non-canonical NFκB signaling (Fig. 5.2), is consistent with the more activated non-canonical NFκB signaling in this model of ARVC. Furthermore, while not quite statistically significant, NFκB1 (p105) and TRIP6 (both suppressors of NFκB) were both downregulated in JHU013 iPSC-CMs (Fig. 5.2).

Figure 5.2 Bulk RNA-seq and pathway analysis of NFκB regulation in JHU013 iPSC-CMs. (A) RNA-seq heatmap analysis and (B) KEGG NFκB pathway schematic. For (A), we identified genes in the NFκB pathway that were differentially expressed between JHU001 and JHU013 iPSC-CMs (BH-adjusted p-value < 0.05). NFκB pathway genes were identified using genes associated with the gene ontology term *NIK/NF-kappaB signaling* (GO:0038061). Color scale denotes row-scaled log expression values. For (B), purple lines and arrows indicate canonical NFκB pathway; green lines and arrows indicate non-canonical NFκB pathway; red shading indicates higher expression in JHU013 relative to control, blue indicates lower expression, and gray indicates no difference. Blue boxes indicate markers which were upregulated in cytokine array experiments.

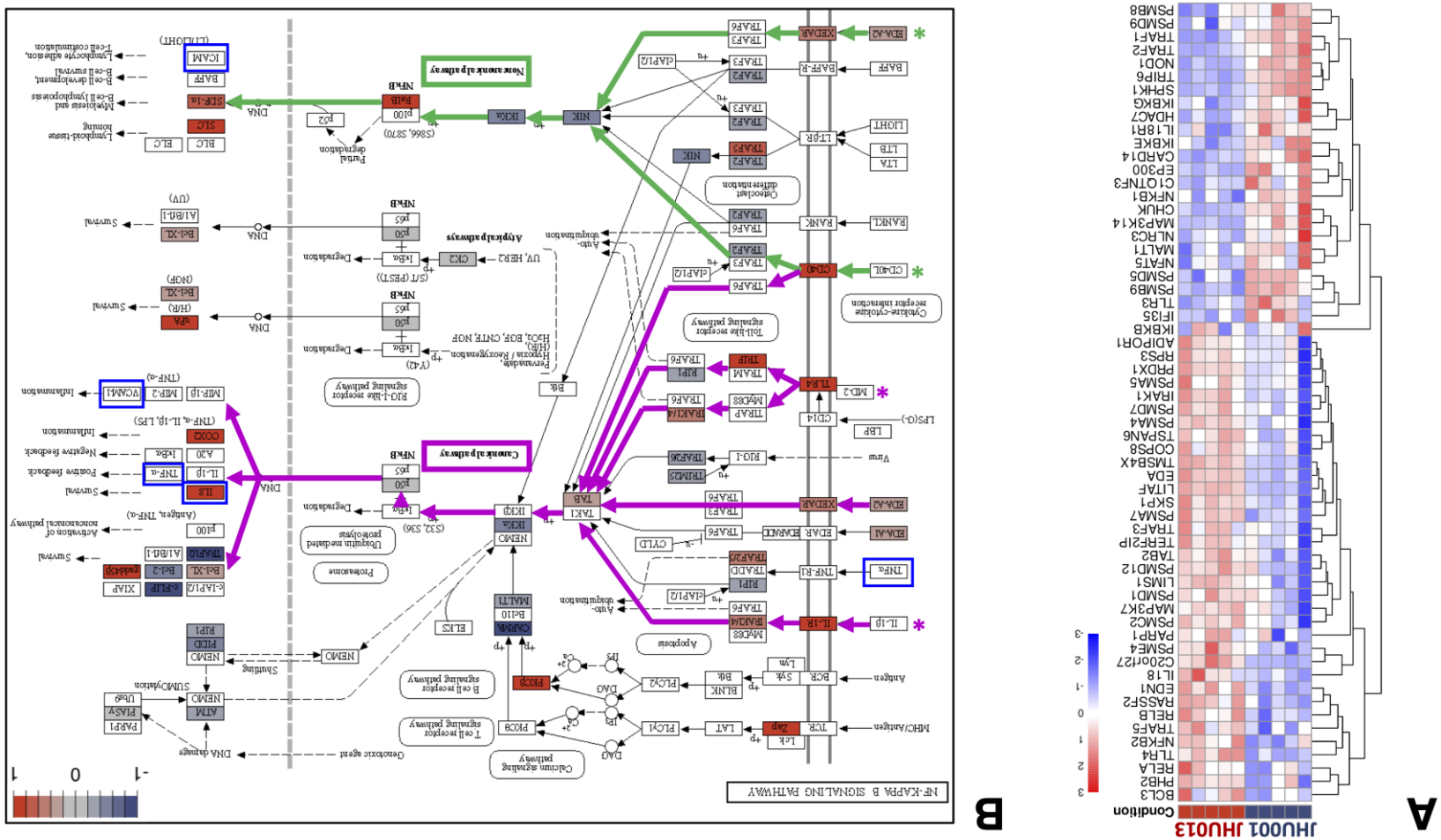

5.3.3 Adipo-fibrokine upregulation in JHU013 iPSC-CMs

Our finding that adipo-fibrokines are more highly expressed in JHU013 iPSC-CMs than in JHU001, is especially interesting considering the huge role that fat infiltration plays in the pathology of ARVC. We therefore sought further evidence that regulation of fat is altered in the *DSG2*-mutant CMs.

We again looked to the RNA-sequencing data. We performed a gene ontology enrichment analysis, which applies a statistical test to determine if some sets of related genes are over- or underrepresented among the genes we determined to be differentially regulated. Among the top results of this analysis, we found three gene ontology sets related to lipid regulation, which were all overrepresented: lipid metabolic process (GO:0006629), lipid modification (GO:0030258), and response to lipid (GO:0033993). This suggests that genes tied to lipid homeostasis are expressed differently between the two lines. To visualize that another way, the volcano plot in Figure 5.3 shows that about two dozen genes associated with those three GO terms are among the most differentially expressed genes in our data set.

Finally, we wanted to assess whether the differences in signaling we observed at the protein and RNA level appreciably alter the deposition of lipids in the iPSC-CMs. To gain an understanding of the gross lipid accumulation in these cells we performed Oil Red O staining on iPSC-CM monolayers as well as on primary human adipocytes (as a positive control).[*] Oil Red O staining revealed little, if any,

[*] Oil Red O staining and imaging was performed by Justin Morrissette-McAlmon.

lipid deposition in either population of iPSC-CMs, while the positive controls were stained bright red (Fig. 5.4). This suggests that despite the measured differences in expression upstream, neither cell line was producing grossly visible lipid deposits.

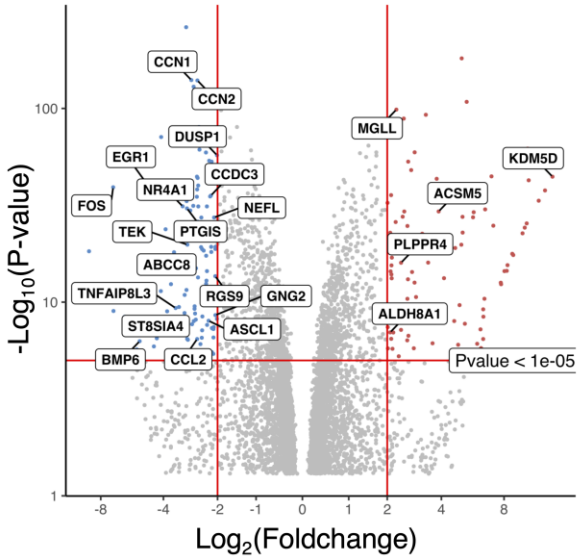

GO Accession	GO term name
GO:0006629	Lipid metabolic process
GO:0030258	Lipid modification
GO:0033993	Response to lipid

Figure 5.3 RNA-seq data suggests altered expression of lipid regulation. A volcano plot showing the expression genes associated with the three lipid-related GO terms (listed to the right) identified in RNA-seq enrichment analyses. Each point represents a gene that was found to be differentially regulated between JHU013 and JHU001. Red points to the right of the vertical red lines are genes which were upregulated in JHU013 by at least four-fold, and blue dots to the left are genes which were downregulated in JHU013 by at least four-fold. The horizontal red line applies a more stringent cutoff value so that everything above that line has a p-value $< 10^{-5}$.

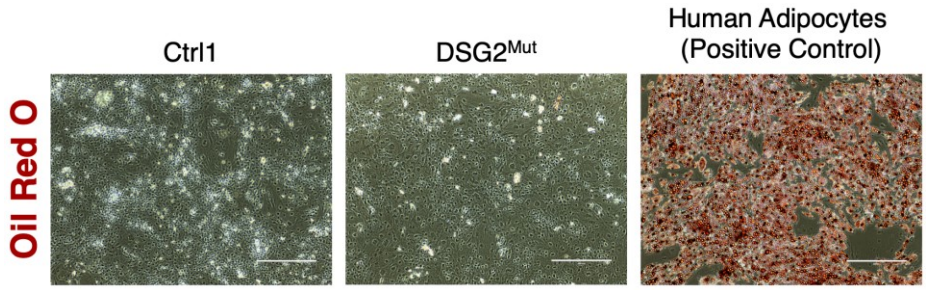

Figure 5.4 Lipid production in iPSC-CMs. JHU001 and JHU013 iPSC-CMs were fixed on differentiation day 35 and stained with Oil Red O to highlight lipid deposits. Phase contrast images revealed no positive staining in iPSC-CMs from either line. Primary human adipocytes are presented as a positive control. White scale bar, 400 μm.

5.4 Discussion

Inflammation is a pathological hallmark of ARVC. Periods known as "hot phases" have been shown to occur in many ARVC patients, in which high levels of inflammation contribute to progression of cardiomyocyte cell death and myocardial fibrotic replacement [36]. It is not yet known whether these inflammatory periods are the result of factors extrinsic to the native myocardium – such as infiltrating professional immune cells – or of intrinsic changes to cardiomyocyte behavior – such as NFκB-mediated cytokine secretion. It's very possible and probably likely that these highly inflammatory hot phases involve both intrinsic and extrinsic influences. Prior reports show infiltration of immune cells in hearts of animal models of ARVC [38,39] and patients with ARVC [131], indicating that extrinsic inflammatory pathways are activated in these cases. On the other hand, our cytokine data in JHU013 iPSC-CMs largely corroborates earlier findings in *PKP2*-mutant iPSC-CMs [39], both demonstrating that intrinsic inflammatory pathways are dysregulated in ARVC iPSC-CMs, even in the absence of non-myocyte immune cells.

We found numerous chemotactic cytokines and inflammation-associated gene transcripts upregulated in relatively pure populations of CMs from JHU013 iPSCs compared to JHU001; these intrinsic signaling pathways could comprise the driving force for recruitment of immune cells into the myocardium of ARVC hearts. Specifically, our RNA-seq data supports instrumental roles for both canonical NFκB signaling through an IRAK-TAB/TAK-RELA pathway and non-canonical NFκB

signaling through a TRAF-IKKa (CHUK) -RELB pathway (Fig. 5.2). More broadly, the cytokine profiles in these JHU013 cells indicate a global upregulation of inflammation machinery and immune cell recruitment. For example, LIF – also known as differentiation stimulating-factor (DSF) – was upregulated in JHU013 iPSC-CMs and is a strong inducer of hematopoietic cell differentiation, known to drive myeloid cells towards macrophage phenotype or pleiotropic cells toward T-cell phenotypes. Both of these terminally differentiated immune cells are routinely found in ARVC hearts [131]. It should also be noted that β-adrenergic stimulation is a powerful activator of NFκB signaling [132], which could draw a link between the clinically observed effects of β-adrenergic signaling (via exercise, stress or drug administration) on ARVC disease progression.

We also found substantial evidence that intrinsic signaling in cardiomyocytes could be important in the myocardial remodeling seen in ARVC. In our cytokine studies, MPO and GROα (also referred to as CXCL1) were more highly expressed in JHU013 iPSC-CMs; both of these cytokines are powerful contributors to cardiac fibrosis via recruitment of neutrophils (i.e. chemotactic immune signaling) together with direct effects on fibroblast proliferation and differentiation [133–136]. Adipo-fibrokines such as Leptin, ApoA1, and THBS1 (thrombospondin-1) were also overexpressed in JHU013 iPSC-CMs (Fig. 5.1). This class of chemokines is known to induce activation of epicardial adipose cells and has been shown to promote fatty infiltration in atrial myocardium [137,138]. RNA-seq data also showed significant dysregulation of genes associated with lipid production and homeostasis (Fig. 5.3).

Our results demonstrating these signaling differences is an important step in identifying new drug targets in ARVC, but further experiments are needed to elucidate the exact roles that these pathways are playing in ARVC pathophysiology, and to test whether disrupting or altering them has positive effects. A key set of experiments will be to evaluate whether inhibitors of NFκB signaling make the electrical or biomolecular phenotypes of JHU013 CMs more closely resemble wildtypes.

5.5 Conclusion

In this chapter, we investigated differences in inflammatory signaling in *DSG2*-mutant ARVC-patient-derived iPSC-CMs. We found that components of pro-inflammatory pathways including both canonical and noncanonical NFκB pathways are overexpressed in JHU013 iPSC-CMs, as are adipo-fibrokines. These results strengthen the evidence that cardiomyocyte-intrinsic inflammatory signaling contributes to ARVC pathophysiology and supports the pursuit of NFκB modulation as a therapeutic strategy.

Chapter 6 – Conclusions

6.1 Summary of Findings

In this dissertation, we set out to generate, characterize and apply an iPSC-CM model of ARVC from a patient with the never-before-studied *DSG2* c.2358delA variant. We validated the iPSC line derived from the patient and found that the cells behaved as expected for iPSCs and expressed the variant of interest on one *DSG2* allele. Electrophysiological testing revealed that, compared to wildtype cells, *DSG2*-mutant iPSC-CMs have much shorter action potential durations and altered calcium transient dynamics, as well as increased heterogeneity of excitability. We also found that *DSG2*-mutant CMs display reduced *DSG2* expression and altered localization of desmoglein-2 protein along with thinner, more poorly organized myofibrils compared to controls, suggesting cytoskeletal impact of the c.2358delA variant. The

impact of the mutation of interest was emphasized by our finding that suppression of *DSG2* expression via siRNA only recapitulated some of the features observed in the *DSG2*-mutant line. We described our attempt to create an isogenic control line and laid out a few lessons that can be learned about gene-editing in iPSC from the difficulties we encountered. Using this newly defined model, we found that β-adrenergic signaling affects *DSG2*-mutant iPSC-CMs very differently than control cells. These effects were not at all reproduced in wildtype cells by *DSG2* suppression. Finally, we detailed our findings that in our iPSC-CMs model, *DSG2*-mutant CMs are very immunologically active, with increased expression of many immune cytokines, alongside more active NFκB and adipo-fibrokine signaling than controls.

6.2 Limitations and Future Directions

Despite the effort detailed in this dissertation, our analysis was limited by several experimental realities, and there remain questions which must be answered in future work. Firstly, our experimental model could be refined in a number of ways. As discussed in the introduction, iPSC-CMs do not fully reach the maturity of adult cardiomyocytes and display phenotypes more reminiscent of neonatal cells. In typical monolayer cultures, they do not assume an elongated morphology or form fully organized intercalated discs, which could affect the level and spatial distribution of desmosomal protein expression. Furthermore, these cells beat spontaneously, and because of their immaturity are more depolarized at rest than

adult ventricular cells, which can affect the dynamics of voltage-gated ion channels and alter excitability [56]. On the other hand, iPSC-CMs cultured in a syncytium such as ours may possess resting transmembrane potentials more similar to adult cardiomyocytes, as compared to single cell preparations [139,140]. There are many ways to enhance iPSC-CM maturity, including chronic electrical pacing, cyclical stretch regimens, metabolic manipulation, and 3D culture methods such as the engineered heart slice [52,141–144]. Employing one or more of these techniques could potentially improve the fidelity of this model to native myocardium. The other major way in which this model could be advanced is by the development of improved experimental controls. For iPSC disease models, isogenic cell lines are becoming increasingly standard for experimental controls. Chapter 3 details our effort and ultimate failure to use CRISPR-Cas9 to generate such a line, but another attempt using an improved editing and validation protocol could provide a very useful tool in evaluating the effects of the specific variant we are interested in. Alternative approaches could include introducing the *DSG2* c.2358delA variant into a wildtype control line (i.e. a “knock-in”) or conditionally silencing the *DSG2* gene for complete suppression (i.e. a “conditional knock-out”).

Our measurements of electrophysiology were rigorously performed and offered invaluable insight, but our conclusions were somewhat constrained by the types of data we were able to collect. The optical mapping system we used provided relative, but not absolute, measures of transmembrane potential and Ca^{2+} concentration. That means we were unable to assess characteristics such as resting membrane

potential, action potential amplitude, and Ca^{2+} transient amplitude. A huge contribution to this work could be made by performing cellular-level electrophysiology experiments (e.g. patch clamp) to gain a fuller picture of the electrical behavior of the JHU013 iPSC-CMs and also to determine which ionic currents underlie the differences in action potential and calcium handling we observed.

Our investigation into the effects of isoproterenol highlighted some very interesting differences in the ways in which *DSG2*-mutant cells respond to adrenergic stimulation compared to wildtype controls. However, we are still in search of a mechanistic explanation for these differences. Patch clamp experiments could be very helpful in identifying the root causes of the action potential discrepancies we found under acute ISO treatment. Our longer-term studies were performed only with a flawed control line, as detailed in Chapter 5, so repeating these experiments with proper controls is an important next step as well. Extending the timeline of the chronic ISO experiments could also be valuable as some studies have found effects in mouse stem cells after one week that were not apparent after 24 hours [38].

Finally, our work characterizing the immune signaling landscape in *DSG2*-mutant iPSC-CMs resulted in some very interesting and potentially impactful findings, but a deeper understanding is needed in order to push these towards clinical application. We identified several signaling pathways and clusters of cytokines that appear dysregulated in *DSG2*-mutant CMs, most notably including

NFκB and adipo-fibrokines. The NFκB findings largely mirror work previously published by our collaborators in *Dsg2*-mutant mice [39], but the relevance and impact of our model would increase substantially if we were able to demonstrate that intervening in either of those signaling pathways corrects, or at least abrogates, the phenotypic differences observed in JHU013 CMs. We have already proposed a subset of these experiments which are currently being set up, including a trial using a patented inhibitor of Il-1β, which is a potent activator of the canonical NFκB pathway. These experiments could help to validate NFκB as a therapeutic target, which could result in a major advancement in treatment options for ARVC patients.

6.3 Conclusions

This dissertation introduced a novel iPSC-CM model of *DSG2*-mutant ARVC and, by evaluating that model, established three primary findings. First, our work suggests that there are substantial cellular-level differences in cytoskeletal organization and cardiomyocyte electrophysiology that could explain early arrhythmia in ARVC patients in the absence of structural damage. Second, contrary to our expectations, we found that the *DSG2*-mutant cells are actually less sensitive to the conduction and action potential duration effects of isoproterenol treatment. And third, we established that immune signaling is markedly abnormal in our iPSC-CM model of ARVC, bolstering the evidence supporting NFκB as a potentially valuable target for new therapies. Further work is needed to push these findings toward clinical significance, with a few questions of particular importance still

needing answers. How is the *DSG2* variant found in the ARVC patient donor mechanistically connected to the electrophysiological and molecular changes we observed? Which cellular processes are differentially affected by isoproterenol treatment? And does intervening in the inflammatory signaling in ARVC iPSC-CMs correct their phenotypic differences? Answering each of these questions will require extensive experimentation beyond the scope of this dissertation, but the work presented herein suggests that each answer could unlock powerful, actionable insight into the pathophysiology of ARVC.

References

1. Saguner, A.M.; Brunckhorst, C.; Duru, F. Arrhythmogenic Ventricular Cardiomyopathy: A Paradigm Shift from Right to Biventricular Disease. *World Journal of Cardiology* **2014**, *6*, 154, doi:10.4330/wjc.v6.i4.154.

2. Tabib, A.; Loire, R.; Chalabreysse, L.; Meyronnet, D.; Miras, A.; Malicier, D.; Thivolet, F.; Chevalier, P.; Bouvagnet, P. Circumstances of Death and Gross and Microscopic Observations in a Series of 200 Cases of Sudden Death Associated with Arrhythmogenic Right Ventricular Cardiomyopathy and/or Dysplasia. *Circulation* 2003, *108*, 3000–3005.

3. Corrado, D.; Basso, C.; Thiene, G.; McKenna, W.J.; Davies, M.J.; Fontaliran, F.; Nava, A.; Silvestri, F.; Blomstrom-Lundqvist, C.; Wlodarska, E.K.; et al. Spectrum of Clinicopathologic Manifestations of Arrhythmogenic Right Ventricular Cardiomyopathy/Dysplasia: A Multicenter Study. *Journal of the American College of Cardiology* **1997**, *30*, 1512–1520, doi:10.1016/S0735-1097(97)00332-X.

4. Basso, C.; Corrado, D.; Thiene, G. Cardiovascular Causes of Sudden Death in Young Individuals Including Athletes. *Cardiology In Review* **1999**, *7*, 127–135, doi:10.1097/00045415-199905000-00009.

5. Corrado, D.; Zorzi, A. Sudden Death in Athletes. *International Journal of Cardiology* **2017**, *237*, doi:10.1016/j.ijcard.2017.03.034.

6. Towbin, J.A.; McKenna, W.J.; Abrams, D.J.; Ackerman, M.J.; Calkins, H.; Darrieux, F.C.C.; Daubert, J.P.; de Chillou, C.; DePasquale, E.C.; Desai, M.Y.; et al. 2019 HRS Expert Consensus Statement on Evaluation, Risk Stratification, and Management of Arrhythmogenic Cardiomyopathy. *Heart Rhythm* **2019**, doi:10.1016/j.hrthm.2019.05.007.

7. Calkins, H. Arrhythmogenic Right Ventricular Dysplasia. *Current Problems in Cardiology* **2013**, *38*, 103–123, doi:10.1016/j.cpcardiol.2012.12.002.

8. Peters, S.; Trümmel, M.; Meyners, W. Prevalence of Right Ventricular Dysplasia-Cardiomyopathy in a Non-Referral Hospital. *International Journal of Cardiology* **2004**, *97*, 499–501, doi:10.1016/j.ijcard.2003.10.037.

9. Basso, C.; Corrado, D.; Marcus, F.I.; Nava, A.; Thiene, G. Arrhythmogenic Right Ventricular Cardiomyopathy. *The Lancet* **2009**, *373*, 1289–1300, doi:10.1016/S0140-6736(09)60256-7.

10. van Lint, F.H.M.; Murray, B.; Tichnell, C.; Zwart, R.; Amat, N.; Lekanne Deprez, R.H.; Dittmann, S.; Stallmeyer, B.; Calkins, H.; van der Smagt, J.J.; et al. Arrhythmogenic Right Ventricular Cardiomyopathy-Associated Desmosomal Variants Are Rarely De Novo. *Circulation: Genomic and Precision Medicine* **2019**, *12*, 337–344, doi:10.1161/circgen.119.002467.

11. Syrris, P.; Ward, D.; Asimaki, A.; Sen-Chowdhry, S.; Ebrahim, H.Y.; Evans, A.; Hitomi, N.; Norman, M.; Pantazis, A.; Shaw, A.L.; et al. Clinical Expression of Plakophilin-2 Mutations in Familial Arrhythmogenic Right Ventricular Cardiomyopathy. *Circulation* **2006**, *113*, 356–364, doi:10.1161/CIRCULATIONAHA.105.561654.

12. Dalal, D.; James, C.; Devanagondi, R.; Tichnell, C.; Tucker, A.; Prakasa, K.; Spevak, P.J.; Bluemke, D.A.; Abraham, T.; Russell, S.D.; et al. Penetrance of Mutations in Plakophilin-2 Among Families With Arrhythmogenic Right Ventricular Dysplasia/Cardiomyopathy. *Journal of the American College of Cardiology* **2006**, *48*, 1416–1424, doi:10.1016/j.jacc.2006.06.045.

13. Groeneweg, J.A.; Bhonsale, A.; James, C.A.; te Riele, A.S.; Dooijes, D.; Tichnell, C.; Murray, B.; Wiesfeld, A.C.P.; Sawant, A.C.; Kassamali, B.; et al. Clinical Presentation, Long-Term Follow-Up, and Outcomes of 1001 Arrhythmogenic Right Ventricular Dysplasia/Cardiomyopathy Patients and Family Members. *Circulation: Cardiovascular Genetics* **2015**, *8*, 437–446, doi:10.1161/CIRCGENETICS.114.001003.

14. Marcus, F.I.; McKenna, W.J.; Sherrill, D.; Basso, C.; Bauce, B.; Bluemke, D.A.; Calkins, H.; Corrado, D.; Cox, M.G.P.J.; Daubert, J.P.; et al. Diagnosis of Arrhytmogenic Right Ventricular Cardiomyopathy/Dysplasia (ARVC/D): Proposed Modification of the Task Force Criteria. *Circulation* **2010**, *121*, 1533–1541, doi:10.1161/CIRCULATIONAHA.108.840827.Diagnosis.

15. Hulot, J.S.; Jouven, X.; Empana, J.P.; Frank, R.; Fontaine, G. Natural History and Risk Stratification of Arrhythmogenic Right Ventricular Dysplasia/Cardiomyopathy. *Circulation* **2004**, *110*, 1879–1884, doi:10.1161/01.CIR.0000143375.93288.82.

16. Gupta, R.; Tichnell, C.; Murray, B.; Rizzo, S.; Te Riele, A.; Tandri, H.; Judge, D.P.; Thiene, G.; Basso, C.; Calkins, H.; et al. Comparison of Features of Fatal Versus Nonfatal Cardiac Arrest in Patients With Arrhythmogenic Right Ventricular Dysplasia/Cardiomyopathy. *American Journal of Cardiology* **2017**, *120*, 111–117, doi:10.1016/j.amjcard.2017.03.251.

17. Vatta, M.; Marcus, F.; Towbin, J.A. Arrhythmogenic Right Ventricular Cardiomyopathy: A “final Common Pathway” That Defines Clinical Phenotype. *European Heart Journal* **2007**, *28*, 529–530, doi:10.1093/eurheartj/ehl530.

18. Garrod, D.; Chidgey, M. Desmosome Structure, Composition and Function. *Biochimica et Biophysica Acta - Biomembranes* **2008**, *1778*, 572–587, doi:10.1016/j.bbamem.2007.07.014.

19. Hall, C.L.; Sutanto, H.; Dalageorgou, C.; McKenna, W.J.; Syrris, P.; Futema, M. Frequency of Genetic Variants Associated with Arrhythmogenic Right Ventricular Cardiomyopathy in the Genome Aggregation Database. *European Journal of Human Genetics* **2018**, *26*, 1312–1318, doi:10.1038/s41431-018-0169-4.

20. Marcus, F.I.; Edson, S.; Towbin, J.A. Genetics of Arrhythmogenic Right Ventricular Cardiomyopathy: A Practical Guide for Physicians. *Journal of the American College of Cardiology* **2013**, *61*, 1945–1948, doi:10.1016/j.jacc.2013.01.073.

21. Kant, S.; Holthöfer, B.; Magin, T.M.; Krusche, C.A.; Leube, R.E. Desmoglein 2-Dependent Arrhythmogenic Cardiomyopathy Is Caused by a Loss of Adhesive Function. *Circulation: Cardiovascular Genetics* **2015**, *8*, 553–563, doi:10.1161/CIRCGENETICS.114.000974.

22. Hariharan, V.; Asimaki, A.; Michaelson, J.E.; Plovie, E.; MacRae, C.A.; Saffitz, J.E.; Huang, H. Arrhythmogenic Right Ventricular Cardiomyopathy Mutations Alter Shear Response without Changes in Cell-Cell Adhesion. *Cardiovascular Research* **2014**, *104*, 280–289, doi:10.1093/cvr/cvu212.

23. Ermakov, S.; Ursell, P.C.; Johnson, C.J.; Meadows, A.; Zhao, S.; Marcus, G.M.; Scheinman, M. Plakoglobin Immunolocalization as a Diagnostic Test for Arrhythmogenic Right Ventricular Cardiomyopathy. *PACE - Pacing and Clinical Electrophysiology* **2014**, *37*, 1708–1716, doi:10.1111/pace.12492.

24. Munkholm, J.; Christensen, A.H.; Svendsen, J.H.; Andersen, C.B. Usefulness of Immunostaining for Plakoglobin as a Diagnostic Marker of Arrhythmogenic Right Ventricular Cardiomyopathy. *American Journal of Cardiology* **2012**, *109*, 272–275, doi:10.1016/j.amjcard.2011.08.044.

25. Asimaki, A.; Tandri, H.; Duffy, E.R.; Winterfield, J.R.; MacKey-Bojack, S.; Picken, M.M.; Cooper, L.T.; Wilber, D.J.; Marcus, F.I.; Basso, C.; et al. Altered Desmosomal Proteins in Granulomatous Myocarditis and Potential Pathogenic Links to Arrhythmogenic Right Ventricular Cardiomyopathy. *Circulation: Arrhythmia and Electrophysiology* **2011**, *4*, 743–752, doi:10.1161/CIRCEP.111.964890.

26. Rizzo, S.; Lodder, E.M.; Verkerk, A.O.; Wolswinkel, R.; Beekman, L.; Pilichou, K.; Basso, C.; Remme, C.A.; Thiene, G.; Bezzina, C.R. Intercalated Disc Abnormalities, Reduced Na+ Current Density, and Conduction Slowing in Desmoglein-2 Mutant Mice Prior to Cardiomyopathic Changes. *Cardiovascular Research* **2012**, *95*, 409–418, doi:10.1093/cvr/cvs219.

27. Gomes, J.; Finlay, M.; Ahmed, A.K.; Ciaccio, E.J.; Asimaki, A.; Saffitz, J.E.; Quarta, G.; Nobles, M.; Syrris, P.; Chaubey, S.; et al. Electrophysiological Abnormalities Precede Overt Structural Changes in Arrhythmogenic Right Ventricular Cardiomyopathy Due to Mutations in Desmoplakin-A Combined Murine and Human Study. *European Heart Journal* **2012**, *33*, 1942–1953, doi:10.1093/eurheartj/ehr472.

28. Kaplan, S.R.; Gard, J.J.; Protonotarios, N.; Tsatsopoulou, A.; Spiliopoulou, C.; Anastasakis, A.; Squarcioni, C.P.; McKenna, W.J.; Thiene, G.; Basso, C.; et al. Remodeling of Myocyte Gap Junctions in Arrhythmogenic Right Ventricular Cardiomyopathy Due to a Deletion in Plakoglobin (Naxos Disease). *Heart Rhythm* **2004**, *1*, 3–11, doi:10.1016/j.hrthm.2004.01.001.

29. Schlipp, A.; Schinner, C.; Spindler, V.; Vielmuth, F.; Gehmlich, K.; Syrris, P.; McKenna, W.J.; Dendorfer, A.; Hartlieb, E.; Waschke, J. Desmoglein-2 Interaction Is Crucial for Cardiomyocyte Cohesion and Function. *Cardiovascular Research* **2014**, *104*, 245–257, doi:10.1093/cvr/cvu206.

30. Schinner, C.; Erber, B.M.; Yeruva, S.; Waschke, J. Regulation of Cardiac Myocyte Cohesion and Gap Junctions via Desmosomal Adhesion. *Acta Physiologica* **2019**, *226*, 1–13, doi:10.1111/apha.13242.

31. El-Battrawy, I.; Zhao, Z.; Lan, H.; Cyganek, L.; Tombers, C.; Li, X.; Buljubasic, F.; Lang, S.; Tiburcy, M.; Zimmermann, W.H.; et al. Electrical Dysfunctions in Human-Induced Pluripotent Stem Cell-Derived Cardiomyocytes from a Patient with an Arrhythmogenic Right Ventricular Cardiomyopathy. *Europace* **2018**, *20*, f46–f56, doi:10.1093/europace/euy042.

32. Marcus, F.I.; Fontaine, G.H.; Guiraudon, G.; Frank, R.; Laurenceau, J.L.; Malergue, C.; Grosgogeat, Y. Right Ventricular Dysplasia: A Report of 24 Adult Cases. *Circulation* **1982**, *65*, doi:10.1161/01.CIR.65.2.384.

33. Corrado, D.; Basso, C.; Thiene, G.; McKenna, W.J.; Davies, M.J.; Fontaliran, F.; Nava, A.; Silvestri, F.; Blomstrom-Lundqvist, C.; Wlodarska, E.K.; et al. Spectrum of Clinicopathologic Manifestations of Arrhythmogenic Right Ventricular Cardiomyopathy/Dysplasia: A Multicenter Study. *Journal of the American College of Cardiology* **1997**, *30*, doi:10.1016/S0735-1097(97)00332-X.

34. Fontaine, G.; Fontaliran, F.; Rosas Andrade, F.; Velasquez, E.; Tonet, J.; Jouven, X.; Fujioka, Y.; Frank, R. The Arrhythmogenic Right Ventricle. Dysplasia versus Cardiomyopathy. *Heart and Vessels* **1995**, *10*, doi:10.1007/BF01744901.

35. Scheel, P.J.; Murray, B.; Tichnell, C.; James, C.A.; Tandri, H.; Calkins, H.; Chelko, S.P.; Gilotra, N.A. Arrhythmogenic Right Ventricular Cardiomyopathy Presenting as Clinical Myocarditis in Women. *American Journal of Cardiology* **2021**, *145*, 128–134, doi:10.1016/j.amjcard.2020.12.090.

36. Murray, B. Arrhythmogenic Right Ventricular Dysplasia/Cardiomyopathy (ARVD/C): A Review of Molecular and Clinical Literature. *Journal of Genetic Counseling* **2012**, *21*, doi:10.1007/s10897-012-9497-7.

37. Pilichou, K.; Remme, C.A.; Basso, C.; Campian, M.E.; Rizzo, S.; Barnett, P.; Scicluna, B.P.; Bauce, B.; Van Den Hoff, M.J.B.; De Bakker, J.M.T.; et al. Myocyte Necrosis Underlies Progressive Myocardial Dystrophy in Mouse Dsg2-Related Arrhythmogenic Right Ventricular Cardiomyopathy. *Journal of Experimental Medicine* **2009**, *206*, 1787–1802, doi:10.1084/jem.20090641.

38. Chelko, S.P.; Keceli, G.; Carpi, A.; Doti, N.; Agrimi, J.; Asimaki, A.; Bueno Beti, C.; Miyamoto, M.; Amat-Codina, N.; Bedja, D.; et al. Exercise Triggers CAPN1-Mediated AIF Truncation, Inducing Myocyte Cell Death in Arrhythmogenic Cardiomyopathy. *Sci. Transl. Med* **2021**, *13*, 891, doi:10.1126/scitranslmed.abf0891.

39. Chelko, S.P.; Asimaki, A.; Lowenthal, J.; Bueno-Beti, C.; Bedja, D.; Scalco, A.; Amat-Alarcon, N.; Andersen, P.; Judge, D.P.; Tung, L.; et al. Therapeutic Modulation of the Immune Response in Arrhythmogenic Cardiomyopathy. *Circulation* **2019**, *140*, 1491–1505, doi:10.1161/CIRCULATIONAHA.119.040676.

40. Chelko, S.P.; Asimaki, A.; Andersen, P.; Bedja, D.; Amat-Alarcon, N.; DeMazumder, D.; Jasti, R.; MacRae, C.A.; Leber, R.; Kleber, A.G.; et al. Central Role for GSK3β in the Pathogenesis of Arrhythmogenic Cardiomyopathy. *JCI Insight* **2016**, *1*, doi:10.1172/jci.insight.85923.

41. Wang, W.; Orgeron, G.; Tichnell, C.; Murray, B.; Crosson, J.; Monfredi, O.; Cadrin-Tourigny, J.; Tandri, H.; Calkins, H.; James, C.A. Impact of Exercise Restriction on Arrhythmic Risk among Patients with Arrhythmogenic Right Ventricular Cardiomyopathy. *Journal of the American Heart Association* **2018**, *7*, doi:10.1161/JAHA.118.008843.

42. Denis, A.; Sacher, F.; Derval, N.; Lim, H.S.; Cochet, H.; Shah, A.J.; Daly, M.; Pillois, X.; Ramoul, K.; Komatsu, Y.; et al. Diagnostic Value of Isoproterenol Testing in Arrhythmogenic Right Ventricular Cardiomyopathy. *Circulation: Arrhythmia and Electrophysiology* **2014**, *7*, 590–597, doi:10.1161/CIRCEP.113.001224.

43. Denis, A.; Sacher, F.; Derval, N.; Martin, R.; Lim, H.S.; Pambrun, T.; Massoullie, G.; Duchateau, J.; Cochet, H.; Pillois, X.; et al. Arrhythmogenic Response to Isoproterenol Testing vs. Exercise Testing in Arrhythmogenic Right Ventricular Cardiomyopathy Patients. *Europace* **2018**, *20*, f30–f36, doi:10.1093/europace/euy007.

44. Schinner, C.; Vielmuth, F.; Rötzer, V.; Hiermaier, M.; Radeva, M.Y.; Co, T.K.; Hartlieb, E.; Schmidt, A.; Imhof, A.; Messoudi, A.; et al. Adrenergic Signaling Strengthens Cardiac Myocyte Cohesion. *Circulation Research* **2017**, *120*, 1305–1317, doi:10.1161/CIRCRESAHA.116.309631.

45. Cerrone, M.; Montnach, J.; Lin, X.; Zhao, Y.T.; Zhang, M.; Agullo-Pascual, E.; Leo-Macias, A.; Alvarado, F.J.; Dolgalev, I.; Karathanos, T. v.; et al. Plakophilin-2 Is Required for Transcription of Genes That Control Calcium Cycling and Cardiac Rhythm. *Nature Communications* **2017**, *8*, doi:10.1038/s41467-017-00127-0.

46. Kim, J.-C.; Pérez-Hernández, M.; Alvarado, F.J.; Maurya, S.R.; Montnach, J.; Yin, Y.; Zhang, M.; Lin, X.; Vasquez, C.; Heguy, A.; et al. Disruption of Ca 2+ i Homeostasis and Connexin 43 Hemichannel Function in the Right Ventricle Precedes Overt Arrhythmogenic Cardiomyopathy in Plakophilin-2–Deficient Mice. *Circulation* **2019**, *140*, 1015–1030, doi:10.1161/circulationaha.119.039710.

47. Vischer, A.S.; Connolly, D.J.; Coats, C.J.; Fuentes, V.L.; Mckenna, W.J.; Castelletti, S.; Pantazis, A.A. *Arrhythmogenic Right Ventricular Cardiomyopathy in Boxer Dogs: The Diagnosis as a Link to the Human Disease*; 2017; Vol. XXXVI;

48. Eason, B.D.; Leach, S.B.; Kuroki, K. *Case Report Rapport de Cas Arrhythmogenic Right Ventricular Cardiomyopathy in a Weimaraner*;

49. Boukens, B.J.; Rivaud, M.R.; Rentschler, S.; Coronel, R. Misinterpretation of the Mouse ECG: “Musing the Waves of Mus Musculus.” *Journal of Physiology* 2014, *592*, 4613–4626.

50. van Mil, A.; Balk, G.M.; Neef, K.; Buikema, J.W.; Asselbergs, F.W.; Wu, S.M.; Doevendans, P.A.; Sluijter, J.P.G. Modelling Inherited Cardiac Disease Using Human Induced Pluripotent Stem Cell-Derived Cardiomyocytes: Progress, Pitfalls, and Potential. *Cardiovascular Research* **2018**, *114*, doi:10.1093/cvr/cvy208.

51. Pan, Z.; Ebert, A.; Liang, P. Human-Induced Pluripotent Stem Cells as Models for Rare Cardiovascular Diseases: From Evidence-Based Medicine to Precision Medicine. *Pflügers Archiv - European Journal of Physiology* **2021**, *473*, doi:10.1007/s00424-020-02486-y.

52. Blazeski, A.; Lowenthal, J.; Wang, Y.; Teuben, R.; Zhu, R.; Gerecht, S.; Tomaselli, G.; Tung, L. Engineered Heart Slice Model of Arrhythmogenic Cardiomyopathy Using Plakophilin-2 Mutant Myocytes. *Tissue Engineering - Part A* **2019**, *25*, 725–735, doi:10.1089/ten.tea.2018.0272.

53. Kim, C.; Wong, J.; Wen, J.; Wang, S.; Wang, C.; Spiering, S.; Kan, N.G.; Forcales, S.; Puri, P.L.; Leone, T.C.; et al. Studying Arrhythmogenic Right Ventricular Dysplasia with Patient-Specific IPSCs. *Nature* **2013**, *494*, 105–110, doi:10.1038/nature11799.

54. Khudiakov, A.; Zaytseva, A.; Perepelina, K.; Smolina, N.; Pervunina, T.; Vasichkina, E.; Karpushev, A.; Tomilin, A.; Malashicheva, A.; Kostareva, A. Sodium Current Abnormalities and Deregulation of Wnt/β-Catenin Signaling in IPSC-Derived Cardiomyocytes Generated from Patient with Arrhythmogenic Cardiomyopathy Harboring Compound Genetic Variants in Plakophilin 2 Gene. *Biochimica et Biophysica Acta - Molecular Basis of Disease* **2020**, *1866*, doi:10.1016/j.bbadis.2020.165915.

55. Uosaki, H.; Cahan, P.; Lee, D.I.; Fernandez, L.; Kass, D.A.; Kwon, C.; Uosaki, H.; Cahan, P.; Lee, D.I.; Wang, S.; et al. Transcriptional Landscape of Cardiomyocyte Resource Transcriptional Landscape of Cardiomyocyte Maturation. *CellReports* **2015**, *13*, 1705–1716, doi:10.1016/j.celrep.2015.10.032.

56. Karbassi, E.; Fenix, A.; Marchiano, S.; Muraoka, N.; Nakamura, K.; Yang, X.; Murry, C.E. Cardiomyocyte Maturation: Advances in Knowledge and Implications for Regenerative Medicine. *Nature Reviews Cardiology* **2020**, *17*, 341–359, doi:10.1038/s41569-019-0331-x.

57. Hawthorne, R.N.; Blazeski, A.; Lowenthal, J.; Kannan, S.; Teuben, R.; DiSilvestre, D.; Morrissette-McAlmon, J.; Saffitz, J.E.; Boheler, K.R.; James, C.A.; et al. Altered Electrical, Biomolecular, and Immunologic Phenotypes in a Novel Patient-Derived Stem Cell Model of Desmoglein-2 Mutant ARVC. *Journal of Clinical Medicine* **2021**, *10*, 3061, doi:10.3390/jcm10143061.

58. Richards, S.; Aziz, N.; Bale, S.; Bick, D.; Das, S.; Gastier-Foster, J.; Grody, W.W.; Hegde, M.; Lyon, E.; Spector, E.; et al. Standards and Guidelines for the Interpretation of Sequence Variants: A Joint Consensus Recommendation of the American College of Medical Genetics and Genomics and the Association for Molecular Pathology. *Genetics in Medicine* **2015**, *17*, 405–424, doi:10.1038/gim.2015.30.

59. Kelly, M.A.; Caleshu, C.; Morales, A.; Buchan, J.; Wolf, Z.; Harrison, S.M.; Cook, S.; Dillon, M.W.; Garcia, J.; Haverfield, E.; et al. Adaptation and Validation of the ACMG/AMP Variant Classification Framework for MYH7-Associated Inherited Cardiomyopathies: Recommendations by ClinGen's

Inherited Cardiomyopathy Expert Panel. *Genetics in Medicine* **2018**, *20*, 351–359, doi:10.1038/gim.2017.218.

60. Dobin, A.; Davis, C.A.; Schlesinger, F.; Drenkow, J.; Zaleski, C.; Jha, S.; Batut, P.; Chaisson, M.; Gingeras, T.R. STAR: Ultrafast Universal RNA-Seq Aligner. *Bioinformatics* **2013**, *29*, doi:10.1093/bioinformatics/bts635.

61. Liao, Y.; Smyth, G.K.; Shi, W. FeatureCounts: An Efficient General Purpose Program for Assigning Sequence Reads to Genomic Features. *Bioinformatics* **2014**, *30*, doi:10.1093/bioinformatics/btt656.

62. Liao, Y.; Smyth, G.K.; Shi, W. The Subread Aligner: Fast, Accurate and Scalable Read Mapping by Seed-and-Vote. *Nucleic Acids Research* **2013**, *41*, doi:10.1093/nar/gkt214.

63. Love, M.I.; Huber, W.; Anders, S. Moderated Estimation of Fold Change and Dispersion for RNA-Seq Data with DESeq2. *Genome Biology* **2014**, *15*, doi:10.1186/s13059-014-0550-8.

64. Luo, W.; Brouwer, C. Pathview: An R/Bioconductor Package for Pathway-Based Data Integration and Visualization. *Bioinformatics* **2013**, *29*, doi:10.1093/bioinformatics/btt285.

65. Sylvain Le Pepe EasyqpcR : EasyqpcR for Easy Analysis of Real-Time PCR Data Available online: http://irtomit.labo.univ-poitiers.fr/.

66. Burridge, P.W.; Matsa, E.; Shukla, P.; Lin, Z.C.; Churko, J.M.; Ebert, A.D.; Lan, F.; Diecke, S.; Huber, B.; Mordwinkin, N.M.; et al. Chemically Defined and Small Molecule-Based Generation of Human Cardiomyocytes. *Nature Methods* **2014**, *11*, 855–860, doi:10.1007/s10549-015-3663-1.Progestin.

67. Toffolo, R.L.; David Ianuzzo, C. *Myofibrillar Adaptations during Cardiac Hypertrophy*; Kluwer Academic Publishers, 1994; Vol. 131;.

68. James, C.A.; Jongbloed, J.D.H.; Hershberger, R.E.; Morales, A.; Judge, D.P.; Syrris, P.; Pilichou, K.; Medeiros Domingo, A.; Murray, B.; Cadrin-Tourigny, J.; et al. An International Evidence Based Reappraisal of Genes Associated with Arrhythmogenic Right Ventricular Cardiomyopathy (ARVC) Using the ClinGen Framework. *Circulation: Genomic and Precision Medicine* **2021**, doi:10.1161/circgen.120.003273.

69. Chen, J.; Nekrasova, O.E.; Patel, D.M.; Klessner, J.L.; Godsel, L.M.; Koetsier, J.L.; Amargo, E. v.; Desai, B. v.; Green, K.J. The C-Terminal

Unique Region of Desmoglein 2 Inhibits Its Internalization via Tail-Tail Interactions. *Journal of Cell Biology* **2012**, *199*, 699–711, doi:10.1083/jcb.201202105.

70. Gehmlich, K.; Asimaki, A.; Cahill, T.J.; Ehler, E.; Syrris, P.; Zachara, E.; Re, F.; Avella, A.; Monserrat, L.; Saffitz, J.E.; et al. Novel Missense Mutations in Exon 15 of Desmoglein-2: Role of the Intracellular Cadherin Segment in Arrhythmogenic Right Ventricular Cardiomyopathy? *Heart Rhythm* **2010**, *7*, 1446–1453, doi:10.1016/j.hrthm.2010.08.007.

71. Asimaki, A.; Tandri, H.; Huang, H.; Halushka, M.K.; Gautam, S.; Basso, C.; Thiene, G.; Tsatsopoulou, A.; Protonotarios, N.; McKenna, W.J.; et al. A New Diagnostic Test for Arrhythmogenic Right Ventricular Cardiomyopathy From the Departments of Pathology. *The New England Journal of Medicine* **2009**, *360*, 1075–1084.

72. D'Amati, G.; Leone, O.; Tiziana di Gioia, C.R.; Magelli, C.; Arpesella, G.; Grillo, P.; Marino, B.; Fiore, F.; Gallo, P. Arrhythmogenic Right Ventricular Cardiomyopathy: Clinicopathologic Correlation Based on a Revised Definition of Pathologic Patterns. *Human Pathology* **2001**, *32*, doi:10.1053/hupa.2001.28232.

73. Hedberg, C.; Melberg, A.; Kuhl, A.; Jenne, D.; Oldfors, A. Autosomal Dominant Myofibrillar Myopathy with Arrhythmogenic Right Ventricular Cardiomyopathy 7 Is Caused by a DES Mutation. *European Journal of Human Genetics* **2012**, *20*, doi:10.1038/ejhg.2012.39.

74. Basso, C.; Czarnowska, E.; della Barbera, M.; Bauce, N.; Beffagna, G.; Wlodarska, E.K.; Pilichou, K.; Ramondo, A.; Lorenzon, A.; Wozniek, O.; et al. Ultrastructural Evidence of Intercalated Disc Remodelling in Arrhythmogenic Right Ventricular Cardiomyopathy: An Electron Microscopy Investigation on Endomyocardial Biopsies. *European Heart Journal* **2006**, *27*, doi:10.1093/eurheartj/ehl095.

75. Chen, P.; Xiao, Y.; Wang, Y.; Zheng, Z.; Chen, L.; Yang, X.; Li, J.; Wu, W.; Zhang, S. Intracellular Calcium Current Disorder and Disease Phenotype in *OBSCN* Mutant IPSC-Based Cardiomyocytes in Arrhythmogenic Right Ventricular Cardiomyopathy. *Theranostics* **2020**, *10*, doi:10.7150/thno.45172.

76. Ma, D.; Wei, H.; Lu, J.; Ho, S.; Zhang, G.; Sun, X.; Oh, Y.; Tan, S.H.; Ng, M.L.; Shim, W.; et al. Generation of Patient-Specific Induced Pluripotent Stem Cell-Derived Cardiomyocytes as a Cellular Model of Arrhythmogenic Right Ventricular Cardiomyopathy. *European Heart Journal* **2013**, *34*, doi:10.1093/eurheartj/ehs226.

77. Shiba, M.; Higo, S.; Kondo, T.; Li, J.; Liu, L.; Ikeda, Y.; Kohama, Y.; Kameda, S.; Tabata, T.; Inoue, H.; et al. Phenotypic Recapitulation and Correction of Desmoglein-2-Deficient Cardiomyopathy Using Human Induced Pluripotent Stem Cell-Derived Cardiomyocytes. *Human Molecular Genetics* **2021**, doi:10.1093/hmg/ddab127/6265028.

78. Willis, B.C.; Ponce-Balbuena, D.; Jalife, J. Protein Assemblies of Sodium and Inward Rectifier Potassium Channels Control Cardiac Excitability and Arrhythmogenesis. *American Journal of Physiology-Heart and Circulatory Physiology* **2015**, *308*, doi:10.1152/ajpheart.00176.2015.

79. Klabunde, R.E. Cardiac Electrophysiology: Normal and Ischemic Ionic Currents and the ECG. *Adv Physiol Educ* **2017**, *41*, 29–37, doi:10.1152/advan.00105.2016.-Basic.

80. Sutanto, H.; Lyon, A.; Lumens, J.; Schotten, U.; Dobrev, D.; Heijman, J. Cardiomyocyte Calcium Handling in Health and Disease: Insights from in Vitro and in Silico Studies. *Progress in Biophysics and Molecular Biology* **2020**, *157*, doi:10.1016/j.pbiomolbio.2020.02.008.

81. van Opbergen, C.J.M.; Delmar, M.; van Veen, T.A.B. Potential New Mechanisms of Pro-Arrhythmia in Arrhythmogenic Cardiomyopathy: Focus on Calcium Sensitive Pathways. *Netherlands Heart Journal* **2017**, *25*, 157–169, doi:10.1007/s12471-017-0946-7.

82. Bhupathy, P.; Babu, G.J.; Periasamy, M. Sarcolipin and Phospholamban as Regulators of Cardiac Sarcoplasmic Reticulum Ca2+ ATPase. *Journal of Molecular and Cellular Cardiology* 2007, *42*, 903–911.

83. Asahi, M.; Otsu, K.; Nakayama, H.; Hikoso, S.; Takeda, T.; Gramolini, A.O.; Trivieri, M.G.; Oudit, G.Y.; Morita, T.; Kusakari, Y.; et al. *Cardiac-Specific Overexpression of Sarcolipin Inhibits Sarco(Endo)Plasmic Reticulum Ca 2 ATPase (SERCA2a) Activity and Impairs Cardiac Function in Mice*; 2004;

84. Zhang, Y.; Matthews, G.D.K.; Lei, M.; Huang, C.L.H. Abnormal Ca2+ Homeostasis, Atrial Arrhythmogenesis, and Sinus Node Dysfunction in

Murine Hearts Modeling RyR2 Modification. *Frontiers in Physiology* 2013, *4 JUN*.

85. Bartos, D.C.; Morotti, S.; Ginsburg, K.S.; Grandi, E.; Bers, D.M. Quantitative Analysis of the Ca2+ -Dependent Regulation of Delayed Rectifier K + Current IKs in Rabbit Ventricular Myocytes. *The Journal of Physiology* **2017**, *595*, doi:10.1113/JP273676.

86. Morgan, J.M.; Cunningham, A.D.; Rowland, E. Relationship of the Effective Refractory Period and Monophasic Action Potential Duration after a Step Increase in Pacing Frequency. *Pacing and Clinical Electrophysiology* **1990**, *13*, doi:10.1111/j.1540-8159.1990.tb02147.x.

87. Priest, B.T.; McDermott, J.S. Cardiac Ion Channels. *Circulation: Arrhythmia and Electrophysiology* **2015**, *2*, 185–194, doi:10.1161/CIRCEP.108.789081.

88. Delmar, M.; Anumonwo, J.; Berenfeld, O. *Basic Mechanisms of Cardiac Arrhythmias*; 2009; ISBN 9781405183338.

89. Kléber, A.G.; Rudy, Y. Basic Mechanisms of Cardiac Impulse Propagation and Associated Arrhythmias. *Physiological Reviews* **2004**, *84*, 431–488, doi:10.1152/physrev.00025.2003.

90. Weiss, J.N.; Garfinkel, A.; Karagueuzian, H.S.; Chen, P.S.; Qu, Z. Early Afterdepolarizations and Cardiac Arrhythmias. *Heart Rhythm* **2010**, *7*, 1891–1899, doi:10.1016/j.hrthm.2010.09.017.

91. Weiss, J.N.; Qu, Z.; Chen, P.; Lin, S.; Karagueuzian, H.S.; Hayashi, H.; Garfinkel, A.; Karma, A. Basic Science for Clinicians The Dynamics of Cardiac Fibrillation. **2005**, 1232–1241, doi:10.1161/CIRCULATIONAHA.104.529545.

92. Akdis, D.; Saguner, A.M.; Shah, K.; Wei, C.; Medeiros-Domingo, A.; von Eckardstein, A.; Lüscher, T.F.; Brunckhorst, C.; Chen, H.S.V.; Duru, F. Sex Hormones Affect Outcome in Arrhythmogenic Right Ventricular Cardiomyopathy/Dysplasia: From a Stem Cell Derived Cardiomyocyte-Based Model to Clinical Biomarkers of Disease Outcome. *European Heart Journal* **2017**, *38*, doi:10.1093/eurheartj/ehx011.

93. Rouhani, F.; Kumasaka, N.; de Brito, M.C.; Bradley, A.; Vallier, L.; Gaffney, D. Genetic Background Drives Transcriptional Variation in Human Induced

Pluripotent Stem Cells. *PLoS Genetics* **2014**, *10*, doi:10.1371/journal.pgen.1004432.

94. Volpato, V.; Webber, C. Addressing Variability in IPSC-Derived Models of Human Disease: Guidelines to Promote Reproducibility. *Disease Models & Mechanisms* **2020**, *13*, doi:10.1242/dmm.042317.

95. Ng, R.; Manring, H.; Papoutsidakis, N.; Albertelli, T.; Tsai, N.; See, C.J.; Li, X.; Park, J.; Stevens, T.L.; Bobbili, P.J.; et al. Patient Mutations Linked to Arrhythmogenic Cardiomyopathy Enhance Calpain-Mediated Desmoplakin Degradation. *JCI Insight* **2019**, *4*, doi:10.1172/jci.insight.128643.

96. Janz, A.; Zink, M.; Cirnu, A.; Hartleb, A.; Albrecht, C.; Rost, S.; Klopocki, E.; Günther, K.; Edenhofer, F.; Ergün, S.; et al. CRISPR/Cas9-Edited PKP2 Knock-out (JMUi001-A-2) and DSG2 Knock-out (JMUi001-A-3) IPSC Lines as an Isogenic Human Model System for Arrhythmogenic Cardiomyopathy (ACM). *Stem Cell Research* **2021**, *53*, doi:10.1016/j.scr.2021.102256.

97. Meraviglia, V.; Arendzen, C.H.; Tok, M.; Freund, C.; Maione, A.S.; Sommariva, E.; Bellin, M. Generation of Human Induced Pluripotent Stem Cell Line LUMCi027-A and Its Isogenic Gene-Corrected Line from a Patient Affected by Arrhythmogenic Cardiomyopathy and Carrying the c.2013delC PKP2 Mutation. *Stem Cell Research* **2020**, *46*, doi:10.1016/j.scr.2020.101835.

98. Ran, F.A.; Hsu, P.D.; Wright, J.; Agarwala, V.; Scott, D.A.; Zhang, F. Genome Engineering Using the CRISPR-Cas9 System. *Nature Protocols* **2013**, *8*, 2281–2308, doi:10.1038/nprot.2013.143.

99. Lu, Y.-Y.; Chen, Y.-C.; Kao, Y.-H.; Wu, T.-J.; Chen, S.-A.; Chen, Y.-J. Extracellular Matrix of Collagen Modulates Intracellular Calcium Handling and Electrophysiological Characteristics of HL-1 Cardiomyocytes With Activation of Angiotensin II Type 1 Receptor. *Journal of Cardiac Failure* **2011**, *17*, doi:10.1016/j.cardfail.2010.10.002.

100. Malan, D.; Reppel, M.; Dobrowolski, R.; Roell, W.; Smyth, N.; Hescheler, J.; Paulsson, M.; Bloch, W.; Fleischmann, B.K. Lack of Laminin Γ1 in Embryonic Stem Cell-Derived Cardiomyocytes Causes Inhomogeneous Electrical Spreading Despite Intact Differentiation and Function. *Stem Cells* **2009**, *27*, doi:10.1634/stemcells.2008-0335.

101. Nakajima, K.; Kazuno, A.A.; Kelsoe, J.; Nakanishi, M.; Takumi, T.; Kato, T. Exome Sequencing in the Knockin Mice Generated Using the CRISPR/Cas System. *Scientific Reports* **2016**, *6*, 1–6, doi:10.1038/srep34703.

102. Veres, A.; Gosis, B.S.; Ding, Q.; Collins, R.; Ragavendran, A.; Brand, H.; Erdin, S.; Talkowski, M.E.; Musunuru, K. Low Incidence of Off-Target Mutations in Individual CRISPR-Cas9 and TALEN Targeted Human Stem Cell Clones Detected by Whole-Genome Sequencing. *Cell Stem Cell* **2014**, *15*, 27–30, doi:10.1016/j.stem.2014.04.020.

103. Li, I.-C.; Fu, J.; Hung, Y.-T.; Chu, E.H.Y. Estimation of Mutation Rates in Cultured Mammalian Cells. *Mutation Research* **1983**, *111*, 253–262.

104. Martincorena, I.; Campbell, P.J. Somatic Mutation in Cancer and Normal Cells. *Science* **2015**, *349*, doi:10.1126/science.aab4082.

105. Kuijk, E.; Jager, M.; van der Roest, B.; Locati, M.D.; van Hoeck, A.; Korzelius, J.; Janssen, R.; Besselink, N.; Boymans, S.; van Boxtel, R.; et al. The Mutational Impact of Culturing Human Pluripotent and Adult Stem Cells. *Nature Communications* **2020**, *11*, doi:10.1038/s41467-020-16323-4.

106. Mianné, J.; Bourguignon, C.; Nguyen Van, C.; Fieldès, M.; Nasri, A.; Assou, S.; de Vos, J. Pipeline for the Generation and Characterization of Transgenic Human Pluripotent Stem Cells Using the CRISPR/Cas9 Technology. *Cells* 2020, *9*.

107. Hanss, Z.; Boussaad, I.; Jarazo, J.; Schwamborn, J.C.; Krüger, R. Quality Control Strategy for CRISPR-Cas9-Based Gene Editing Complicated by a Pseudogene. *Frontiers in Genetics* **2020**, *10*, doi:10.3389/fgene.2019.01297.

108. Merkert, S.; Bednarski, C.; Göhring, G.; Cathomen, T.; Martin, U. Generation of a Gene-Corrected Isogenic Control IPSC Line from Cystic Fibrosis Patient-Specific IPSCs Homozygous for p.Phe508del Mutation Mediated by TALENs and SsODN. *Stem Cell Research* **2017**, *23*, doi:10.1016/j.scr.2017.07.010.

109. Kawatani, K.; Nambara, T.; Nawa, N.; Yoshimatsu, H.; Kusakabe, H.; Hirata, K.; Tanave, A.; Sumiyama, K.; Banno, K.; Taniguchi, H.; et al. A Human Isogenic IPSC-Derived Cell Line Panel Identifies Major Regulators

of Aberrant Astrocyte Proliferation in Down Syndrome. *Communications Biology* **2021**, *4*, doi:10.1038/s42003-021-02242-7.

110. Fontaine, V.; Duboscq-Bidot, L.; Jouve, C.; Hamlin, M.; Curjol, A.; Briand, V.; Janiak, P.; Hulot, J.-S.; Pruniaux-Harnist, M.-P.; Charron, P.; et al. Generation of IPSC Line from MYH7 R403L Mutation Carrier with Severe Hypertrophic Cardiomyopathy and Isogenic CRISPR/Cas9 Corrected Control. *Stem Cell Research* **2021**, *52*, doi:10.1016/j.scr.2021.102245.

111. Sleiman, Y.; Souidi, M.; Kumar, R.; Yang, E.; Jaffré, F.; Zhou, T.; Bernardin, A.; Reiken, S.; Cazorla, O.; Kajava, A. v.; et al. Modeling Polymorphic Ventricular Tachycardia at Rest Using Patient-Specific Induced Pluripotent Stem Cell-Derived Cardiomyocytes. *EBioMedicine* **2020**, *60*, doi:10.1016/j.ebiom.2020.103024.

112. Wang, W.; Tichnell, C.; Murray, B.A.; Agafonova, J.; Cadrin-Tourigny, J.; Chelko, S.; Tandri, H.; Calkins, H.; James, C.A. Exercise Restriction Is Protective for Genotype-Positive Family Members of Arrhythmogenic Right Ventricular Cardiomyopathy Patients. *EP Europace* **2020**, *22*, doi:10.1093/europace/euaa105.

113. Wichter, T.; Schäfers, M.; Rhodes, C.G.; Borggrefe, M.; Lerch, H.; Lammertsma, A.A.; Hermansen, F.; Schober, O.; Breithardt, G.; Camici, P.G. Abnormalities of Cardiac Sympathetic Innervation in Arrhythmogenic Right Ventricular Cardiomyopathy. *Circulation* **2000**, *101*, doi:10.1161/01.CIR.101.13.1552.

114. Lefkowitz, R.J.; Pitcher, J.; Krueger, K.; Daaka, Y. Mechanisms of β-Adrenergic Receptor Desensitization and Resensitization. In; 1997.

115. Choi, D.-J.; Koch, W.J.; Hunter, J.J.; Rockman, H.A. Mechanism of β-Adrenergic Receptor Desensitization in Cardiac Hypertrophy Is Increased β-Adrenergic Receptor Kinase. *Journal of Biological Chemistry* **1997**, *272*, doi:10.1074/jbc.272.27.17223.

116. George, C.F. Intravenously Administered Isoproterenol Sulfate Dose-Response Curves in Man. *Archives of Internal Medicine* **1972**, *130*, doi:10.1001/archinte.1972.03650030041010.

117. Kassebaum, D.G.; van Dyke, A.R. Electrophysiological Effects of Isoproterenol on Purkinje Fibers of the Heart. *Circulation Research* **1966**, *19*, doi:10.1161/01.RES.19.5.940.

118. Zeng, H.; Wang, J.; Clouse, H.; Lagrutta, A. Unveiling the Lack of Inotropic Response of Human Induced Pluripotent Stem Cell-Derived Cardiomyocytes to Isoproterenol by Chronic External Stimulation. *Applied In Vitro Toxicology* **2020**, *6*, doi:10.1089/aivt.2020.0002.

119. Zeng, H.; Balasubramanian, B.; Lagrutta, A.; Sannajust, F. Response of Human Induced Pluripotent Stem Cell-Derived Cardiomyocytes to Several Pharmacological Agents When Intrinsic Syncytial Pacing Is Overcome by Acute External Stimulation. *Journal of Pharmacological and Toxicological Methods* **2018**, *91*, doi:10.1016/j.vascn.2017.12.004.

120. Patel, D.; Stohlman, J.; Dang, Q.; Strauss, D.G.; Blinova, K. Assessment of Proarrhythmic Potential of Drugs in Optogenetically Paced Induced Pluripotent Stem Cell-Derived Cardiomyocytes. *Toxicological Sciences* **2019**, *170*, doi:10.1093/toxsci/kfz076.

121. Sun, N.; Yazawa, M.; Liu, J.; Han, L.; Sanchez-Freire, V.; Abilez, O.J.; Navarrete, E.G.; Hu, S.; Wang, L.; Lee, A.; et al. Patient-Specific Induced Pluripotent Stem Cells as a Model for Familial Dilated Cardiomyopathy. *Science Translational Medicine* **2012**, *4*, doi:10.1126/scitranslmed.3003552.

122. Zhang, G.Q.; Wei, H.; Lu, J.; Wong, P.; Shim, W. Identification and Characterization of Calcium Sparks in Cardiomyocytes Derived from Human Induced Pluripotent Stem Cells. *PLoS ONE* **2013**, *8*, doi:10.1371/journal.pone.0055266.

123. Liu, J.; Fu, J.D.; Siu, C.W.; Li, R.A. Functional Sarcoplasmic Reticulum for Calcium Handling of Human Embryonic Stem Cell-Derived Cardiomyocytes: Insights for Driven Maturation. *Stem Cells* **2007**, *25*, doi:10.1634/stemcells.2007-0549.

124. Dolnikov, K.; Shilkrut, M.; Zeevi-Levin, N.; Gerecht-Nir, S.; Amit, M.; Danon, A.; Itskovitz-Eldor, J.; Binah, O. Functional Properties of Human Embryonic Stem Cell-Derived Cardiomyocytes: Intracellular Ca $^{2+}$ Handling and the Role of Sarcoplasmic Reticulum in the Contraction. *Stem Cells* **2006**, *24*, doi:10.1634/stemcells.2005-0036.

125. Fontaine, G.; Fontaliran, F.; Andrade, F.; Velasquez, E.; Tonet, J.; Jouven, X.; Fujioka, Y.; Frank, R. The Arrhythmogenic Right Ventricle. Dysplasia versus Cardiomyopathy. *Heart Vessels* **1995**, *10*, 227–235.

126. Bangert, A.; Andrassy, M.; Müller, A.M.; Bockstahler, M.; Fischer, A.; Volz, C.H.; Leib, C.; Göser, S.; Korkmaz-Icöz, S.; Zittrich, S.; et al. Critical Role of RAGE and HMGB1 in Inflammatory Heart Disease. *Proceedings of the National Academy of Sciences of the United States of America* **2016**, *113*, E155–E164, doi:10.1073/pnas.1522288113.

127. Zhong, Q.; Zhou, K.; Liang, Q.L.; Lin, S.; Wang, Y.C.; Xiong, X.Y.; Meng, Z.Y.; Zhao, T.; Zhu, W.Y.; Yang, Y.R.; et al. Interleukin-23 Secreted by Activated Macrophages Drives ΓδT Cell Production of Interleukin-17 to Aggravate Secondary Injury after Intracerebral Hemorrhage. *Journal of the American Heart Association* **2016**, *5*, doi:10.1161/JAHA.116.004340.

128. Ha, H.; Han, D.; Choi, Y. TRAF-Mediated TNFR-Family Signaling. *Current Protocols in Immunology* 2009.

129. Xie, P. TRAF Molecules in Cell Signaling and in Human Diseases. *Journal of Molecular Signaling* 2013, *8*.

130. Shi, J.H.; Sun, S.C. Tumor Necrosis Factor Receptor-Associated Factor Regulation of Nuclear Factor KB and Mitogen-Activated Protein Kinase Pathways. *Frontiers in Immunology* 2018, *9*.

131. Gandjbakhch, E.; Redheuil, A.; Pousset, F.; Charron, P.; Frank, R. Clinical Diagnosis, Imaging, and Genetics of Arrhythmogenic Right Ventricular Cardiomyopathy/Dysplasia: JACC State-of-the-Art Review. *Journal of the American College of Cardiology* 2018, *72*, 784–804.

132. Takemoto, Y.; Yoshiyama, M.; Takeuchi, K.; Omura, T.; Komatsu, R.; Izumi, Y.; Kim, S.; Yoshikawa, J. Increased JNK, AP-1 and NF-KB DNA Binding Activities in Isoproterenol-Induced Cardiac Remodeling. *Journal of Molecular and Cellular Cardiology* **1999**, *31*, 2017–2030, doi:10.1006/jmcc.1999.1033.

133. Lau, D.; Mollnau, H.; Eiserich, J.P.; Freeman, B.A.; Daiber, A.; Gehling, U.M.; Brummer, J.; Rudolph, V.; Munzel, T.; Heitzer, T.; et al. Myeloperoxidase Mediates Neutrophil Activation by Association with CD11b/CD18 Integrins. *Proceedings of the National Academy of Sciences* **2005**, *102*, doi:10.1073/pnas.0405193102.

134. Friedrichs, K.; Baldus, S.; Klinke, A. Fibrosis in Atrial Fibrillation – Role of Reactive Species and MPO. *Frontiers in Physiology* **2012**, *3*, doi:10.3389/fphys.2012.00214.

135. Sawant, K. v.; Sepuru, K.M.; Lowry, E.; Penaranda, B.; Frevert, C.W.; Garofalo, R.P.; Rajarathnam, K. Neutrophil Recruitment by Chemokines Cxcl1/KC and Cxcl2/MIP2: Role of Cxcr2 Activation and Glycosaminoglycan Interactions. *Journal of Leukocyte Biology* **2021**, *109*, doi:10.1002/JLB.3A0820-207R.

136. Wang, L.; Zhang, Y.-L.; Lin, Q.-Y.; Liu, Y.; Guan, X.-M.; Ma, X.-L.; Cao, H.-J.; Liu, Y.; Bai, J.; Xia, Y.-L.; et al. CXCL1–CXCR2 Axis Mediates Angiotensin II-Induced Cardiac Hypertrophy and Remodelling through Regulation of Monocyte Infiltration. *European Heart Journal* **2018**, *39*, doi:10.1093/eurheartj/ehy085.

137. Venteclef, N.; Guglielmi, V.; Balse, E.; Gaborit, B.; Cotillard, A.; Atassi, F.; Amour, J.; Leprince, P.; Dutour, A.; Clément, K.; et al. Human Epicardial Adipose Tissue Induces Fibrosis of the Atrial Myocardium through the Secretion of Adipo-Fibrokines. *European Heart Journal* **2015**, *36*, doi:10.1093/eurheartj/eht099.

138. Abe, I.; Teshima, Y.; Kondo, H.; Kaku, H.; Kira, S.; Ikebe, Y.; Saito, S.; Fukui, A.; Shinohara, T.; Yufu, K.; et al. Association of Fibrotic Remodeling and Cytokines/Chemokines Content in Epicardial Adipose Tissue with Atrial Myocardial Fibrosis in Patients with Atrial Fibrillation. *Heart Rhythm* **2018**, *15*, doi:10.1016/j.hrthm.2018.06.025.

139. van de Sande, D. v.; Kopljar, I.; Maaike, A.; Teisman, A.; Gallacher, D.J.; Bart, L.; Snyders, D.J.; Leybaert, L.; Lu, H.R.; Labro, A.J. The Resting Membrane Potential of HSC-CM in a Syncytium Is More Hyperpolarised than That of Isolated Cells. *Channels* **2021**, *15*, 239–252, doi:10.1080/19336950.2021.1871815.

140. Li, W.; Han, J.L.; Entcheva, E. Syncytium Cell Growth Increases Kir2.1 Contribution in Human IPSC-Cardiomyocytes. *Am J Physiol Heart Circ Physiol* **2020**, *319*, 1112–1122, doi:10.1152/ajpheart.00148.2020.

141. Morrissette-McAlmon, J.; Hawthorne, R.N.; Snyder, S.; Grayson, W.L. Strategies for Tissue Engineering Vascularized Cardiac Patches to Treat Myocardial Infarctions. In *Biophysical Regulation of Vascular Differentiation and Assembly*; Gerecht, S., Ed.; Springer, 2018; pp. 141–175 ISBN 9783319993195.

142. Blazeski, A.; Kostecki, G.M.; Tung, L. Engineered Heart Slices for Electrophysiological and Contractile Studies. *Biomaterials* **2015**, *55*, 119–128, doi:10.1016/j.biomaterials.2015.03.026.

143. Stoppel, W.L.; Kaplan, D.L.; Black, L.D. Electrical and Mechanical Stimulation of Cardiac Cells and Tissue Constructs. *Advanced Drug Delivery Reviews* **2016**, *96*, 135–155, doi:10.1016/j.addr.2015.07.009.

144. Sharma, A.; Zhang, Y.; Buikema, J.W.; Serpooshan, V.; Chirikian, O.; Kosar, N.; Churko, J.M.; Dzilic, E.; Shieh, A.; Burridge, P.W.; et al. Stage-Specific Effects of Bioactive Lipids on Human IPSC Cardiac Differentiation and Cardiomyocyte Proliferation. **2018**, 1–10, doi:10.1038/s41598-018-24954-3.

Vita

Robert Nathaniel Hawthorne was born in Indianapolis, Indiana on November 17th, 1993. He received his Bachelor of Science degree in Engineering Sciences – Chemical and Material Bioengineering from Harvard University in Cambridge, Massachusetts in 2015. Before and during his undergraduate education he had the opportunity to conduct thymic carcinoma research at the Indiana University Simon Cancer Center under Angelo Cardoso, M.D., Ph.D., microfluidic chip design work at the University of Michigan at Ann Arbor under Sunitha Nagrath, Ph.D., and three-dimensional bioprinting materials research at The Wyss Institute for Biologically Inspired Engineering at Harvard University under Jennifer Lewis, Sc.D. In 2015, he enrolled in the Medical Scientist Training Program at Johns Hopkins University School of Medicine and began his medical education before joining the Biomedical Engineering Ph.D. program in 2017. Robert's doctoral research contributed to three conference presentations, a textbook chapter, and a first-author peer-reviewed publication [57,141].